Theses and Dissertations

May 2013

Towards the Use of Time-Resolved X-ray Crystallography in Mechanistic Studies of Cytochrome c Nitrite Reductase from Shewanella Oneidensis

Matthew David Youngblut
University of Wisconsin-Milwaukee

TOWARDS THE USE OF

TIME-RESOLVED X-RAY CRYSTALLOGRAPHY

IN MECHANISTIC STUDIES OF

CYTOCHROME *C* NITRITE REDUCTASE

FROM *SHEWANELLA ONEIDENSIS*

by

Matthew D. Youngblut

A Dissertation Submitted in

Partial Fulfillment of the

Requirements for the Degree of

Doctor of Philosophy

in Chemistry

at

The University of Wisconsin-Milwaukee

May 2013

ABSTRACT

TOWARDS THE USE OF TIME-RESOLVED X-RAY CRYSTALLOGRAPHY IN MECHANISTIC STUDIES OF CYTOCHROME *C* NITRITE REDUCTASE FROM *SHEWANELLA ONEIDENSIS*

by

Matthew D. Youngblut

The University of Wisconsin-Milwaukee

Under the Supervision of Professor A. Andrew Pacheco

A high-yield expression and purification of *Shewanella oneidensis* cytochrome *c* nitrite reductase (ccNiR), and its characterization by a variety of methods, notably Laue crystallography, is reported. A key component of the expression system is an artificial ccNiR gene in which the N-terminal signal peptide from the highly expressed *S. oneidensis* protein "Small Tetra-heme *c*" replaces the wild-type signal peptide. This gene, inserted into the plasmid pHSG298 and expressed in *S. oneidensis* TSP-1 strain, generated approximately 20 mg crude ccNiR/L culture, compared with 0.5-1 mg/L for untransformed cells. Purified ccNiR exhibited nitrite and hydroxylamine reductase activities comparable to those of *E. coli* ccNiR. UV/Vis spectropotentiometric titrations identified five independent one-electron reduction processes. Global analysis of the spectropotentiometric data also allowed determination of the extinction coefficient

spectra for the five reduced ccNiR species. Purified ccNiR yielded good quality crystals, with which the 2.59Å resolution structure was solved at room temperature using the Laue diffraction method. The structure is similar to that of *E. coli* ccNiR, except in the region where each enzyme interacts with distinct physiological partners. Using the above-mentioned expression system, a mutant ccNiR bearing a surface cysteine was prepared and labeled with the photo-active $[Ru(bpy)_2(5\text{-iodoacetamido-}1,10\text{-phenanthroline})]^{2+}$. In the presence of ferrocyanide the Ru-labeled ccNiR could be photo-reduced in less than 1μs using a 5ns laser pulse. *S. oneidensis* ccNiR also oxidizes hydroxylamine, yielding nitrite as the sole nitrogenous product. UV/visible stopped-flow and rapid freeze-quench EPR data, along with product analysis, showed that the equilibrium between hydroxylamine and nitrite is fairly rapidly established in the presence of large initial concentrations of hydroxylamine, despite said equilibrium lying far to the left. By contrast reduction of hydroxylamine to ammonia did not occur, even though disproportionation of hydroxylamine to yield both nitrite and ammonia is strongly favored thermodynamically. This suggests a kinetic barrier to the ccNiR-catalyzed reduction of hydroxylamine to ammonia, which has important mechanistic implications. The availability of a large quantity of ccNiR, that yields crystals suitable for diffractometry using the Laue method, and that can be tagged with a photo-reductant, opens the door to future time-resolved X-ray crystallographic studies with this enzyme.

To Elizabeth,

my one true partner in life

Table of Contents

List of Figures

List of Tables

List of Schemes

Acknowledgments

I would first and foremost like to thank my thesis advisor, Dr. Andy Pacheco, for his tireless efforts to help me become a better scientist, and also a better person. Dr. Pacheco is truly gifted as a mentor, and sets a great example as to how to approach science, and how to get others interested in science as well. It was Dr. Pacheco that inspired me to extend my education into graduate school, and now I hope to make him proud of me with my future endeavors.

I would further like to thank each of my thesis committee members, Dr. Graham Moran, Dr. Dennis Bennett, Dr. Nick Silvaggi, and Dr. Marius Schmidt. Every member of my committee has helped me, either by working directly with me in the lab, or via helpful discussions. Their efforts greatly advanced my graduate career.

Science is a team effort, and without strong collaborations with other scientists in my research group and outside it, I could never have made the progress I did. This dissertation is a testament to our combined efforts. In this regard I first want to thank all past and present graduate students in my research group: Dr. Joshua Kostera, Jennifer McGarry, Natalia Stein, Patrick Cobb, Karl Koebke, and Dan Pauly. Natalia in particular contributed directly to the preparation of a ccNiR mutant with a surface cysteine. Undergraduate researchers are a constant and welcome presence in our laboratory, and many contributed to this project over the years. Major contributions were made by Bilal Sayyed and Tyler Groelzer, who helped develop the purification protocol for ccNiR, by Angel Corona and Daniel Walters who worked out an important ammonia assay, and by Victor Trussell who carried out essential stability experiments on the enzyme. Notably,

Chapter 1

Introduction

1.1. Overview of the nitrogen cycle

Bacterial respiratory processes play a major role in the interconversion of many inorganic compounds, such as those involved in the nitrogen cycle (*1-3*). In the nitrogen cycle, atmospheric nitrogen is first fixed to form ammonia by nitrogen fixing bacteria such as *Azotobacter sp.*   A variety of other organisms then metabolize the ammonia into multiple nitrogenous compounds, which together with ammonia are collectively referred to as "reactive nitrogen species", in order to extract energy for ATP formation. The metabolic processes by which reactive nitrogen species are intercoverted can be divided into aerobic oxidative and anaerobic reductive pathways (Figure 1.1).

The primary aerobic oxidative bacterial respiratory pathway in the nitrogen cycle is the nitrification pathway. Nitrification is the process whereby ammonia is oxidized first to hydroxylamine, subsequently to nitrite, and finally to nitrate. Certain aerophillic bacteria, such as *Nitrosomonas europaea*, couple the oxidation of ammonia to nitrite with the reduction of oxygen during respiration. A different class of bacteria then oxidizes nitrite to nitrate, again using oxygen as the electron acceptor.
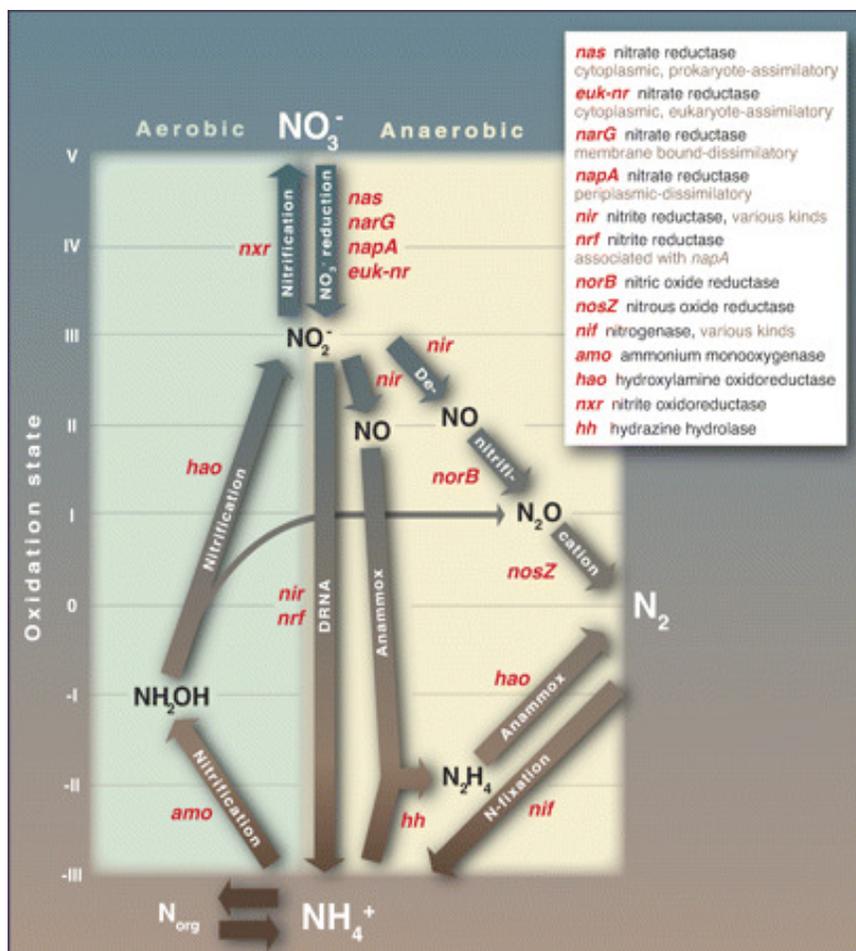
Figure 1.1. Depiction of the nitrogen cycle divided into oxidative aerobic reactions and reductive anaerobic reactions (*4*).

In anaerobic respiration of reactive nitrogen species, microorganisms use these compounds as the terminal electron acceptors of respiration in place of oxygen. The anaerobic processes show considerably more variety than the aerobic ones. Many organisms use a variety of nitrate reductases to reduce nitrate to nitrite, but at this point the possible respiratory pathways diverge. Figure 1.1 shows that nitrite is the center of a branch point of three major reductive pathways. The denitrification pathway is a

multistep process where nitrite is first reduced to nitric oxide, then nitrous oxide, and finally to molecular nitrogen. This pathway exists largely in heterotrophic bacteria, and usually involves a series of species (*3, 5, 6*). Another anaerobic reductive pathway in the reduction of nitrite is the ANaerobic AMMonia OXidation (ANAMMOX) pathway, which has gained notoriety in recent times (*7-9*). The ANAMMOX pathway is a combination of oxidative and reductive reactions where ammonia comproportionates with nitrite to form hydrazine, a major component of rocket fuel, which is then oxidized to molecular nitrogen (*10*). To date, all bacteria known to use the ANAMMOX pathway belong to the phylum Plantomycetes, and these bacteria have been utilized in some countries to purify wastewater (*11*). The remaining major biological pathway for the reduction of nitrite is the Dissimilatory Reduction of Nitrate to Ammonia (DRNA) pathway. Several species of bacteria, such as *Shewanella oneidensis*, *Escherichia coli*, and *Wollinella succinogenes*, use this pathway to directly reduce nitrite to ammonia using a single enzyme, cytochrome *c* nitrite reductase (ccNiR). This process is used exclusively for energy transduction; the ammonia generated is not incorporated into organic molecules, as it would be in assimilatory nitrite reduction, which is catalyzed by distinct nitrite reductases.

This dissertation focuses on a mechanistic investigation of ccNiR from *S. oneidensis*. To place this kinetic analysis in context, we first explore the thermodynamic conditions that allow bacteria to extract energy from the reduction of nitrite to ammonia. Figure 1.2 shows a pH 7 Frost diagram for the different nitrogenous species involved in the nitrogen cycle, relative to the standard hydrogen-proton couple. Since NE° is directly proportional to the standard free energy of each species in the diagram, one can see that

an organism could extract energy from the surroundings by coupling the reduction of

nitrate or nitrite to ammonia, with oxidation of a metabolite with a midpoint potential

comparable to the hydrogen-proton couple.
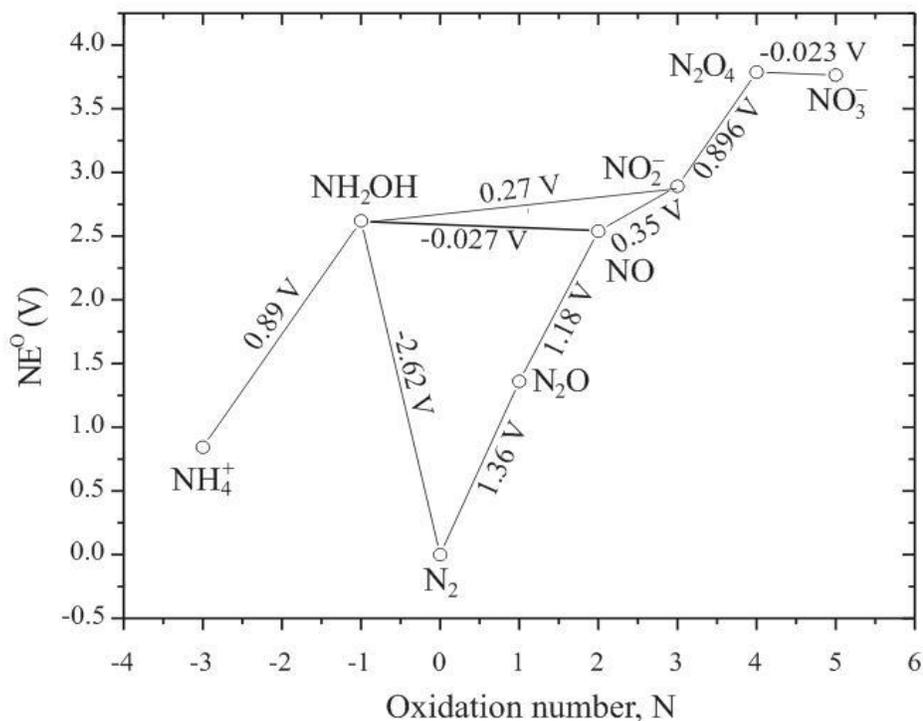
Figure 1.2. Frost diagram for the nitrogenous species involved in the nitrogen cycle.

Values given are relative to the standard hydrogen electrode.

1.2. Introduction to *S. oneidensis* ccNiR

Shewanella oneidensis is a Gram-negative γ-proteobacterium originally isolated

from Lake Oneida, NY in 1988 (*12*). This organism is unique in that it can respire using

over two dozen different terminal electron acceptors (*13*), which include inorganic

compounds, such as nitrate and nitrite, organic molecules, such as formate and dimethyl

sulfoxide, and even metals, such as manganese(V) and uranium(VI). The genome sequence for *S. oneidensis*, released in 2002, identified at least 42 genes bearing the CXXCH motif characteristic of *c*-type cytochromes (*14, 15*). *C*-heme proteins are often highly efficient in electron transfer functions, and it has been hypothesized that *S. oneidensis* has a large number of respiratory options due to the presence of the large number of these proteins. Among the *c*-heme proteins encoded by *S. oneidensis* is ccNiR, which catalyzes the reduction of nitrite to ammonia.

CcNiR is a soluble protein located in the periplasm of several bacterial species, including *S. oneidensis*. This enzyme is a homodimer, with protomeric molecular weights ranging from 52-65 kDa (depending on the organism from which it is expressed), in which each protomer contains five *c*-type hemes (*16-21*). Four of these hemes are six-coordinate, *bis*-histidine ligated and low-spin (Shown in yellow and green in Figure 1.3). This motif is fairly ubiquitous in *c*-hemes involved exclusively in electron transport. The hemes shown in green in Figure 1.3 are solvent exposed, and are believed to accept electrons directly from ccNiR's physiological electron donors (*17, 22, 23*). The electron donor for different ccNiRs is dependent on the organism from which it is derived. For *S. oneidensis*, the physiological electron donor has been shown to be cymA, a cytoplasmic membrane electron transport protein (*23*). In *E. coli*, another γ-proteobacterium, the physiological donor has been identified as the soluble, periplasmic tetraheme protein nrfB, whereas other organisms, such as the δ-proteobacterium *D. desulfuricans* and the ε-proteobacterium *W. succinogenes*, use a periplasmic integral membrane protein known as nrfH as the electron donor to ccNiR (*17, 22*). The fifth *c*-type heme in ccNiR (shown in orange in Figure 1.3) acts as the active site in each protomer. It is five-coordinate,

allowing the substrate nitrite to bind to the open distal position, and is unique among *c*-hemes in that the axial ligand is a lysine residue. The chaperone proteins nrfEFG have been shown to be critical for incorporating this novel active-site arrangement (*24*). In addition to the five iron atoms from the hemes, each ccNiR protomer contains one buried six-coordinate Ca^{2+} ion per monomer in all ccNiRs characterized to date. In the case of *D. desulfuricans* ccNiR, the crystal structure shows a second six-coordinate Ca^{2+} ion in each monomer (*20*).
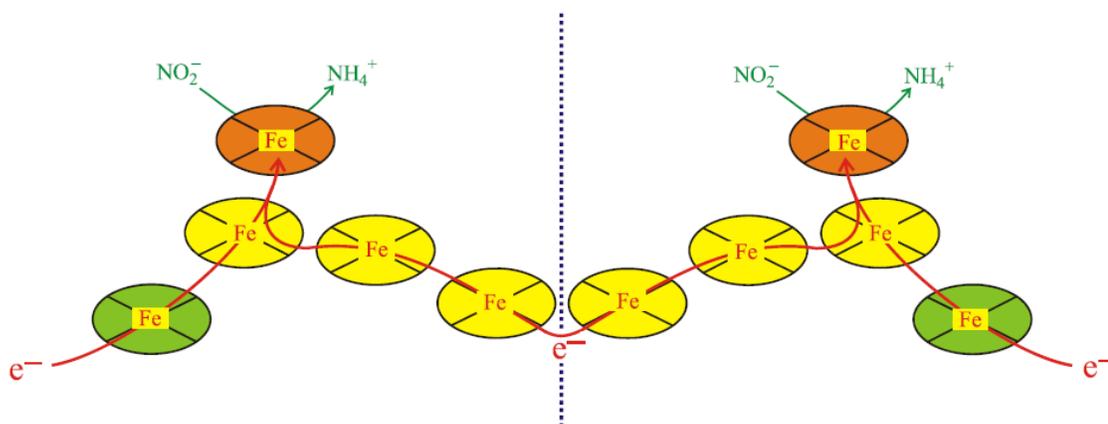
Figure 1.3. Schematic depiction of the heme arrangement within the ccNiR dimer. The hemes shown in orange are the active sites of each monomer. The hemes shown in yellow and green are used solely in electron transport, with the difference being that the hemes shown in green are solvent exposed. CcNiR presumably interacts with its physiological electron donor at these green hemes.

The arrangement of the hemes in ccNiR is such that they are closely packed, with iron-iron distances of <13 Å, which facilitates rapid inter-heme electron transfer (*25*). Physiologically, ccNiR performs the direct six-electron reduction of nitrite to ammonia (Scheme 1.1) with no unbound intermediates produced during catalysis. Scheme 1.1 also shows that ccNiR can catalyze the five-electron reduction of nitric oxide, and the two-electron reduction of hydroxylamine; in both cases ammonia is the product. Additionally, ccNiR has been shown to reductively turn over sulfite to hydrogen sulfide (Scheme 1.1), albeit at a much slower rate than its turnover of reactive nitrogen species.

$$NO_2^- + 8H^+ + 6e^- \longrightarrow NH_4^+ + 2H_2O$$
$$NO^\bullet + 6H^+ + 5e^- \longrightarrow NH_4^+ + H_2O$$
$$NH_2OH + 3H^+ + 2e^- \longrightarrow NH_4^+ + H_2O$$
$$SO_3^{2-} + 7H^+ + 6e^- \longrightarrow HS^- + 3H_2O$$
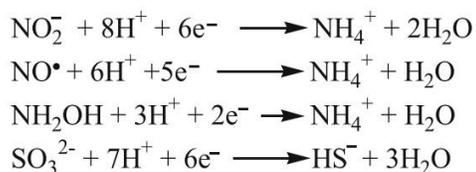
Scheme 1.1. Reactions catalyzed by ccNiR.

Einsle et al. proposed the first reaction mechanism for the reduction of nitrite by ccNiR (red arrows, Figure 1.4) based on crystallographic data and density functional theory (DFT) calculations (*26*). The mechanism is also consistent with ccNiR's known catalytic capabilities (Scheme 1.1); though free NO and NH$_2$OH are not released during nitrite reduction, Figure 1.4 shows Fe-bound intermediates of these species. At the start of the project described in this dissertation, the mechanism in Figure 1.4 was our working hypothesis. More recently the ccNiR reaction mechanism has been investigated further by Bykov and Neese using more advanced DFT calculations (*27, 28*), which allows some

details to be added to Figure 1.4. Initially, for the reduction of nitrite by ccNiR, nitrite displaces a water molecule normally found in the active site of the resting enzyme. When the active-site heme has a weak-field ligand bound, such as water, the heme is high-spin. The active-site heme then undergoes a high-spin to low-spin transition when a relatively strong-field ligand, such as nitrite, binds.

Figure 1.4. Proposed minimal reaction mechanism for nitrite-ammonia and/or nitrite-hydroxylamine interconversion catalyzed by ccNiR and HAO. Red arrows show the reductive reactions, blue ones the oxidative reactions.

At this point, a one-electron/two-proton reductive event occurs. During this event, one N-O bond is heterolytically cleaved (*27*), resulting in the formation of a species referred to as $\{Fe(NO)\}^6$ in the Enemark and Feltham notation (*29*). In this notation the iron and iron-bound species are contained in braces, and the superscript outside the braces indicates the number of *d*-electrons from the heme iron atom, combined with the number of π^* electrons from the iron-bound species. The $\{Fe(NO)\}^6$ can also be represented by two resonance structures (Figure 1.4): NO^+ bound to Fe(II), and $NO^{\cdot}$ bound to Fe(III). Bykov and Neese predict that the $\{Fe(NO)\}^6$ moiety is formed from the nitrite-bound species via two sequential protonation steps. Initially, one oxygen atom of the bound nitrite becomes protonated, which results in a HONO adduct (*27*). This adduct is polarized such that the two N-O bonds are inequivalent, causing the N-OH bond to be weakened due to the presence of the active-site iron (*27*). The –OH group can now be further protonated and leave as water, leading to the formation of the $\{Fe(NO)\}^6$ species. The next step in the cycle is a one-electron reduction that leads to the formation of an $\{Fe(NO)\}^7$ species (Figure 1.4), which has been previously characterized in model compounds (*30-32*). This species can also be represented by two resonance forms, this time $NO^{\cdot}$ bound to Fe(II), and NO^- bound to Fe(III). $\{Fe(NO)\}^7$ species tend to adopt more bent configurations than $\{Fe(NO)\}^6$ species, which in extreme cases where the Fe(III)NO^+ form predominates may actually have linear Fe-N-O geometry. A further protonation step would retain the same number of electrons, but would lead to the formation of an $\{Fe(HNO)\}^7$ species (Figure 1.4). From here, a two-electron/two-proton reductive event occurs to produce hydroxylamine bound to ferrous active-site (Figure 1.4). Recently, proton-coupled electron transfer (PCET) has been proposed as a means

for this process to occur without the need to form high-energy intermediates (*28*). A final two-electron/two-proton reductive event would give ammonia bound to the ferrous active-site, which would then be readily displaced by water and protonated to give free ammonium (Figure 1.4).

An important question that remains to be answered experimentally is the identity of the proton donors that facilitate the reduction of nitrite to ammonia by ccNiR. Three particular amino acid residues that are highly conserved in all ccNiRs, and are located in the active-site binding pocket, have been implicated for nitrite reduction (*17, 33*). For the *S. oneidensis* ccNiR, these amino acid residues are His257, Arg103, and Tyr206, which correlate to the *E. coli* amino acid residues of His277, Arg114, and Tyr218, respectively (Figure 1.5). His257 is the likely proton donor in the active-site under normal physiological conditions, since its pK_a is near physiological pH, and it can be easily tuned by the local protein environment (*34*). Also, histidine residues have been characterized as proton donors both in heme-containing enzymes, such as the cd_1 nitrite reductase (*35*), and in non-heme enzymes, such as serine proteases (*36*). Since ccNiR has been shown to be catalytic from pH 6-10, histidine is probably not the proton donor above pH ~ 8. At higher pH, Arg103 would most likely assume the role of the proton donor. The role of Tyr206 (or Tyr218 in *E. coli*) has been examined by Bykov and Neese (*27*), and their computational studies have indicated that this amino acid residue does not have a direct role in protonation; however, this tyrosine residue could be involved in facilitating the shuttling of protons from the region near the Ca^{2+} ion located in each ccNiR protomer to the active site. This would give the Ca^{2+} ion a catalytic role in ccNiR, in addition to its structural importance. The Ca^{2+} ion is in direct contact with the protein backbone at

Tyr206 in the *S. oneidensis* ccNiR, and is located only ~10 Å from the active-site iron center. Furthermore, studies with *E. coli* ccNiR mutants have shown that the Ca^{2+} coordination environment significantly affects the activity of the active site (*33*), which supports the hypothesis that Ca^{2+} plays a catalytic role. A Ca^{2+} ion has been previously characterized operating in a similar manner in carbonic anhydrase (*37*). While Tyr206 might not be involved in the direct protonation of bound substrate species, it could be involved in the mechanism for recharging His257/Arg103 during these multiple protonation events (*27, 28*).
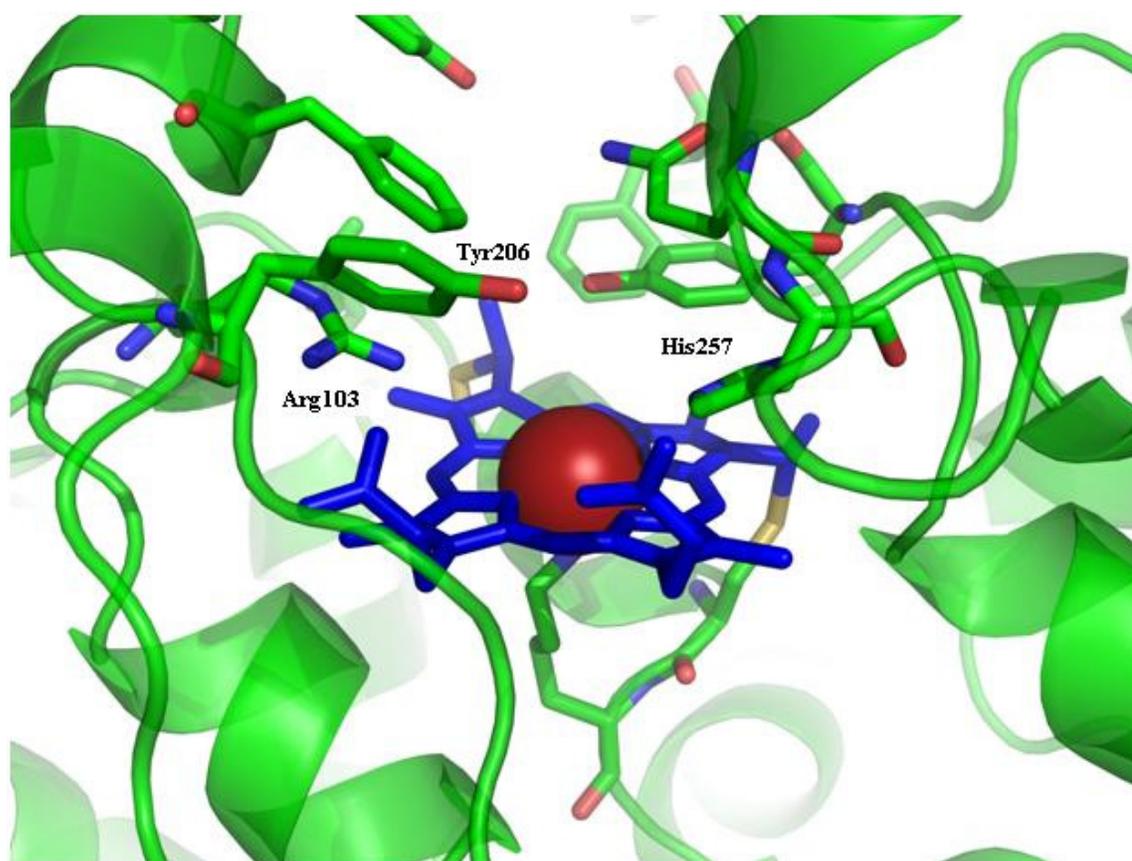
Figure 1.5. View of the active-site of *S. oneidensis* ccNiR. Three highly conserved amino acid residues (His257, Arg103, Tyr206) in the active-site binding pocket have been implicated in proton-transfer steps during the reduction of nitrite to ammonia.

1.3. Nitrite reduction vs. hydroxylamine oxidation

The arrangement of the hemes in ccNiR is quite similar to that seen in another

multi- *c*-heme protein, hydroxylamine oxidoreductase (HAO), which is expressed by the

bacterium *Nitrosomonas europaea* (*38*). HAO catalyzes the four-electron oxidation of

hydroxylamine to nitrite in the nitrification pathway (Figure 1.1). When this process is

coupled to oxygen reduction, *N. europaea* can use the energy released to fuel its

metabolic needs. Intriguingly, while ccNiR and HAO share similar heme arrangements,

the enzymes operate in opposite directions: whereas ccNiR is funneling electrons toward

the active site to reduce nitrite, HAO is funneling electrons away from the active site to

oxidize hydroxylamine. Furthermore, it is possible to posit a formal mechanism for

hydroxylamine oxidation by HAO which includes all the same intermediates as those

proposed for nitrite reduction by ccNiR; this is shown by the blue arrows in Figure 1.4.

These observations raise the interesting question of whether and/or how ccNiR and HAO

are optimized to operate preferentially in one direction or the other, particularly given the

superficial similarities between the heme arrangements in the two proteins. A major

long-term research goal within the Pacheco group is to answer this question via

mechanistic studies of the two enzymes. This dissertation focuses on the reactivity of

ccNiR, while HAO is being studied in a separate project.

1.4. Introduction to time resolved X-ray crystallography

The major strategy being employed in the study of both ccNiR and HAO is to

characterize as fully as possible the individual steps by which the enzymes carry out their

respective processes. These steps are expected to be very fast (with lifetimes in the microsecond to millisecond timescales), so they must be studied using specialized time-resolved techniques. A technique that shows great promise in this regard, but which has never been used on systems as complex as the ccNiR-catalyzed reduction of nitrite, is time-resolved X-ray crystallography using the Laue method.

Laue crystallography is described in more detail in Chapter 3, but briefly, it allows one to collect diffraction patterns very quickly using 1-10 100 ps bursts of polychromatic X-rays. This confers the Laue method with two important advantages over conventional crystallography. First, exposing proteins to X-rays over a period of time eventually changes the protein structure. In conventional crystallography, which requires relatively long exposure times, these changes often happen on the timescale of data collection, and so one obtains a "blurred" structure, which is the time-average of all the species (*39*). By contrast, using the Laue method to collect X-ray diffraction data quickly is akin to taking a photograph with a fast shutter speed: data collection is fast compared to the timescale in which the X-rays induce structural changes to occur, and so one sees the structure as it was before the X-ray exposure (*40, 41*). The second important advantage of the Laue method is that it opens the door to making "movies" of a reaction in progress. In this application a reaction is rapidly initiated within a crystal, usually by laser activation of a suitable chromophore within the crystal, and then after a time delay, Δt, the structure is obtained using the Laue method. This provides information about the structural changes that have occurred within the protein from the time the reaction was initiated until the moment the diffraction patterns were obtained. The movie is then built up frame-by-frame by repeating the process with different Δt delays.

While the application of time-resolved crystallography to a complex protein such as ccNiR is a long-term goal of the Pacheco group, the work described here lays the groundwork for such an investigation.

1.5. Summary of the dissertation objectives

Our desire to eventually study ccNiR using time-resolved crystallography immediately imposed a series of practical objectives onto the dissertation project. First, an overexpression system for the enzyme needed to be developed since crystallography experiments require large quantities of protein. Even though several ccNiR structures had been reported by the time the project began, we chose to concentrate on developing an expression system in *S. oneidensis*, since this bacterium produces *c*-heme proteins very readily, even under aerobic conditions. Other bacteria, such as *E. coli*, do not do this without a relatively extensive amount of genetic manipulation (*42*). The development of the *S. oneidensis* overexpression system is described in Chapter 2. A second benchmark that needed to be reached in order to show that time-resolved crystallography with ccNiR was feasible, was to identify crystallization conditions that yielded ccNiR crystals of sufficient quality for use in the Laue method. In general, the requirements of the Laue method are substantially more stringent than those for conventional crystallography using monochromatic X-rays. The solution of the *S. oneidensis* ccNiR structure using the Laue method is described in Chapter 3. A final practical requirement for using time-resolved crystallography on ccNiR was to develop a

suitable method for photo-initiating substrate reduction within the protein crystal. Progress achieved in this goal is described in Chapter 4.

In addition to laying the groundwork for applying time-resolved crystallography to the study of ccNiR, investigations of the enzyme using more traditional biochemical techniques were also performed. Chapter 5 describes a spectropotentiometric study of ccNiR, which yielded the midpoint potentials for reduction of the five *c*-hemes, as well as the associated spectral components. Chapter 6 describes an investigation of the reaction between fully oxidized ccNiR and hydroxylamine, using stopped-flow UV/Vis and freeze-quenched EPR experiments. These experiments demonstrate that ccNiR can be made to operate in 'reverse'; that is, as a hydroxylamine oxidase that oxidizes hydroxylamine to nitrite. The results are compared to those reported recently by our group, in which HAO was forced to operate as a nitrite reductase in the presence of strong reducing agents (*43, 44*).

1.6. References

1.   Haddock, B. A., and Jones, C. W. (1977) Bacterial Respiration, *Bacteriological Reviews 41*, 47-99.

2.   Richardson, D. J. (2000) Bacterial respiration: a flexible process for a changing environment, *Microbiology 146*, 551-571.

3.   Cole, J. A., and Brown, C. M. (1980) Nitrite Reduction to Ammonia by Fermentative Bacteria: A Short Circuit in the Biological Nitrogen Cycle, *FEMS Microbiology Letters 7*, 65-72.

4.   Canfield, D. E., Glazer, A. N., and Falkowski, P. G. (2010) The Evolution and
        Future of Earth's Nitrogen Cycle, *Science 330*, 192-196.

5.   Knowles, R. (1982) Denitrification, *Microbiological Reviews 46*, 43-70.

6.   Zumft, W. G. (1997) Cell biology and molecular basis of denitrification,
        Microbiology and Molecular Biology Reviews 61, 533-616.

7.   Strous, M., Gerven, E. V., Kuenen, J. G., and Jetten, M. S. M. (1997) Effects of
        aerobic and microaerobic conditions on anaerobic ammonium-oxidizing
        (anammox) sludge, *Applied and Environmental Microbiology 63*, 2446-2448.

8.   Kuypers, M. M. M., Sliekers, A. O., Lavik, G., Schmid, M., Jorgensen, B. B.,
        Kuenen, J. G., Sinninghe Damste, J. S., Strous, M., and Jetten, M. S. M. (2003)
        Anaerobic ammonium oxidation by anammox bacteria in the Black Sea, *Letters to
        Nature 422*, 608-611.

9.   Op den Camp, H. J., Kartal, J., Guven, D., van Niftrik, L. A., Haaijer, S. C., W.R.,
        v. d. S., van de Pas-Schoonen, K. T., Cabezas, A., Ying, Z., Schmid, M., Kuypers,
        M. M. M., van de Vossenberg, J., Harhangi, H. R., Picioreanu, C., van Loosdrect,
        M. C., Kuenen, J. G., Strous, M., and Jetten, M. S. M. (2006) Global impact and
        application of the anaerobic ammonium-oxidizing (anammox) bacteria,
        Biochemical Society Transactions 34, 174-178.

10.   Schalk, J., Oustad, H., Kuenen, J. G., and Jetten, M. S. M. (1998) The anaerobic
        oxidation of hydrazine: a novel reaction in microbial nitrogen metabolism, *FEMS
        Microbiology Letters 158*, 61-67.

11. van Dongen, U., Jetten, M. S. M., and van Loosdrect, M. C. (2001) The SHARON-Anammox process for treatment of ammonium rich wastewater, *Water Science and Technology 44*, 153-160.

12. Venkateswaran, K., Moser, D. P., Dollhopf, M. E., Lies, D. P., Saffarini, D. A., MacGregor, B. J., Ringelberg, D. B., White, D. C., Miyuki, N., Sano, H., Burghardt, J., Stackebrandt, E., and Nealson, K. H. (1999) Polyphasic taxonomy of the genus Shewanella and description of Shewanella oneidensis sp. now, *International Journal of Systematic Bacteriology 49*, 705-724.

13. Beliaev, A. S., Klingeman, D. M., Klappenbach, J. A., Wu, L., Romine, M. F., Tiedje, J. M., Nealson, K. H., Fredrickson, J. K., and Zhou, J. (2005) Global Transcriptome Analysis of Shewanella oneidensis MR-1 Exposed to Different Terminal Electron Acceptors, *Journal of Bacteriology 187*, 7138-7145.

14. Heidelberg, J. F., Paulsen, I. T., Nelson, K. E., Gaidos, E. J., Nelson, W. C., Read, T. D., Eisen, J. A., Seshadri, R., Ward, N., Methe, B., Clayton, R. A., Meyer, T., Tsapin, A., Scott, J., Beanan, M., Brinkac, L., Daugherty, S., DeBoy, R. T., Dodson, R. J., Durkin, A. S., Haft, D. H., Kolonay, J. F., Madupu, R., Peterson, J. D., Umayam, L. A., White, O., Wolf, A. M., Vamathevan, J., Weidman, J., Impraim, M., Lee, K., Berry, K., Lee, C., Mueller, J., Khouri, H., Gill, J., Utterback, T. R., McDonald, L. A., Feldblyum, T. V., Smith, H. O., Venter, J. C., Nealson, K. H., and Fraser, C. M. (2002) Genome sequence of the dissimilatory metal ion-reducing bacterium Shewanella oneidensis, *Nature Biotechnology 20*, 1118-1123.

15. Meyer, T. E., Tsapin, A. I., Vandenberghe, I., de Smet, L., Frishman, D., Nealson, K. H., Cusanovich, M. A., and J.J., v. B. (2004) Identification of 42 possible cytochrome c genes in the Shewanella oneidensis genome and characterization of six soluble cytochromes, *OMICS: A Journal of Integrative Biology 8*, 57-77.

16. Einsle, O., Messerschmidt, A., Stach, P., Bourenkov, G. P., Bartunik, H. D., Huber, R., and Kroneck, P. M. H. (1999) Structure of cytochrome c nitrite reductase, *Nature 400*, 476-480.

17. Einsle, O., Stach, P., Messerschmidt, A., Simon, J., Kroger, A., Huber, R., and Kroneck, P. M. H. (2000) Cytochrome c nitrite reductase from Wolinella succinogenes - Structure at 1.6 angstrom resolution, inhibitor binding, and heme-packing motifs, *J. Biol. Chem. 275*, 39608-39616.

18. Pereira, I., LeGall, J., Xavier, A., and Teixeira, M. (2000) Characterization of a heme *c* nitrite reductase from a non-ammonifying microorganism, *Desulfovibrio vulgaris* Hildenborough, *Biochim. Biophys. Acta 1481*, 119-130.

19. Bamford, V. A., Angove, H. C., Seward, H. E., Thomson, A. J., Cole, J. A., Butt, J. N., Hemmings, A. M., and Richardson, D. J. (2002) Structure and spectroscopy of the periplasmic cytochrome c nitrite reductase from Escherichia coli, *Biochemistry 41*, 2921-2931.

20. Cunha, C. A., Macieira, S., Dias, J. M., Almeida, G., Goncalves, L. L., Costa, C., Lampreia, J., Huber, R., Moura, J. J. G., Moura, I., and Romao, M. J. (2003) Cytochrome c nitrite reductase from Desulfovibrio desulfuricans ATCC 27774 - The relevance of the two calcium sites in the structure of the catalytic subunit (NrfA), *J. Biol.Chem. 278*, 17455-17465.

21. Rodrigues, M. L., Oliveira, T., Matias, P. M., Martins, C., Valente, F. M., Pereira, I. A., and Archer, M. (2006) Crystallization and preliminary structure determination of the membrane-bound complex cytochrome c nitrite reductase from Desulfovibrio vulgaris Hildenborough, *Acta Cryst. F 62*, 565-568.

22. Rodrigues, M., Oliveira, T., Pereira, I., and Archer, M. (2006) X-ray structure of the membrane-bound cytochrome *c* quinol dehydrogenase NrfH reveals novel haem coordination, *EMBO Journal 25*, 5951-5960.

23. Gao, H., Yang, Z. K., Barua, S., Reed, S. B., Romine, M. F., Nealson, K. H., Fredrickson, J. K., Tiedje, J. M., and Zhou, J. (2009) Reduction of nitrate in *Shewanella oneidensis* depends on atypical NAP and NRF systems with NapB as a preferred electron transport protein from CymA to NapA, *ISME Journal 3*, 966-976.

24. Eaves, D. J., Grove, J., Staudenmann, W., James, P., Poole, R. K., White, S. A., Griffiths, L., and Cole, J. A. (1998) Involvement of products of the *nrfEFG* genes in the covalent attachment of haem *c* to a novel cysteine-lysine motif in the cytochrome c_{552} nitrite reductase from *Escherichia coli*, *Mol. Microbiol. 28*, 205-216.

25. Burlat, B., Gwyer, J. D., Poock, S., Clarke, T., Cole, J. A., Hemmings, A. M., Cheesman, M. R., Butt, J. N., and Richardson, D. J. (2005) Cytochrome c nitrite reductase: from structural to physicochemical analysis, *Biochemical Society Transactions 33*, 137-140.

26. Einsle, O., Messerschmidt, A., Huber, R., Kroneck, P. M. H., and Neese, F. (2002) Mechanism of the six-electron reduction of nitrite to ammonia by cytochrome c nitrite reductase, *J. Am. Chem. Soc. 124*, 11737-11745.

27. Bykov, D., and Neese, F. (2011) Substrate binding and activation in the active site of cytochrome *c* nitrite reductase: a density functional study, *J. Biol. Inorg. Chem 16*, 417-430.

28. Bykov, D., and Neese, F. (2012) Reductive activation of the heme iron-nitrosyl intermediate in the reaction mechanism of cytochrome c nitrite reductase: a theoretical study, *Journal of Biological Inorganic Chemistry 17*, 741-760.

29. Enemark, J. H., and Feltham, R. D. (1974) Principles of Structure, Bonding and Reactivity for Metal Nitrosyl Complexes, *Coord. Chem. Rev. 13*, 339-406.

30. Roncaroli, F., Videla, M., and Olabe, J. A. (2007) New features in the redox coordination chemistry of metal nitrosyls {M–NO+; M–NO; M–NO−(HNO)}, *Coordination Chemistry Reviews 251*, 1903-1930.

31. Wasser, I. M., de Vries, S., Moenne-Loccoz, P., Schroder, I., and Karlin, K. D. (2002) Nitric Oxide in Biological Denitrification: Fe/Cu Metalloenzyme and Metal Complex NOx Redox Chemistry, *Chemical Reviews 102*, 1201-1234.

32. Averill, B. A. (1996) Dissimilatory Nitrite and Nitric Oxide Reductases, *Chemical Reviews 96*, 2951-2964.

33. Clarke, T. A., Kemp, G. L., Van Wonderen, J. H., Doyle, R. A. S., Cole, J. A., Tovell, N., Cheesman, M. R., Butt, J. N., Richardson, D. J., and Hemmings, A. M. (2008) Role of a conserved glutamine residue in tuning the catalytic activity of *Escherichia coli* Cytochrome *c* nitrite reductase, *Biochemistry 47*, 3789-3799.

34. Markley, J. L. (1975) Correlation proton magnetic resonance studies at 250 MHz of bovine pancreatic ribonuclease. I. Reinvestigation of the histidine peak assignments, *Biochemistry 14*, 3546-3554.

35. Marti, M. A., Crespo, A., Bari, S. E., Doctorovich, F. A., and Estrin, D. A. (2004) QM−MM Study of Nitrite Reduction by Nitrite Reductase of Pseudomonas aeruginosa, *Journal of Physical Chemistry B 108*, 18073-18080.

36. Hudaky, P., and Perczel, A. (2007) pKa optimized catalysis in serine proteinases, an ab initio study on the catalaytic His, *International Journal of Quantum Chemistry 107*, 2178-2183.

37. Shinobu, A., and Agmon, N. (2009) Mapping Proton Wires in Proteins: Carbonic Anhydrase and GFP Chromophore Biosynthesis, *Journal of Physical Chemistry A 113*, 7253-7266.

38. Hooper, A. B., and Nason, A. J. (1965) Characterization of Hydroxylamine-cytochrome *c* reductase from the chemoautotrohs *Nitrosomonas europaea* and *Nitrosocystis oceanus*, *J. Biol. Chem.*, 4044-4057.

39. Ravelli, R. B. G., and McSweeney, S. M. (2000) The "fingerprint" that X-rays can leave on structures, *Structure 8*, 315-328.

40. Schmidt, M., Šrajer, V., Purwar, N., and Tripathi, S. (2012) The Kinetic Dose Limit in Room Temperature Time-resolved Macromolecular Crystallography, *J. Synchrotron Rad. 19*, Available online, Jan 2012.

41. Youngblut, M., Judd, E. T., Srajer, V., Sayyed, B., Goelzer, T., Elliott, S. J., Schmidt, M., and Pacheco, A. A. (2012) Laue crystal structure of *Shewanella*

oneidensis cytochrome *c* nitrite reductase from a high-yield expression system, *J. Biol. Inorg. Chem. 17*, 647-662.

42.   Londer, Y. Y., Pokkuluri, P. R., Tiede, D. M., and Schiffer, M. (2002) Production and preliminary characterization of a recombinant triheme cytochrome c_7 from *Geobacter reducens* in *E. coli*, *Biochim. Biophys. acta 1554*, 202-211.

43.   Kostera, J., Youngblut, M. D., Slosarczyk, J. M., and Pacheco, A. A. (2008) Kinetic and product distribution analysis of NO reductase activity in *Nitrosomonas europaea* hydroxylamine oxidoreductase, *J. Biol. Inorg. Chem. 13*, 1073-1083.

44.   Kostera, J., McGarry, J. M., and Pacheco, A. A. (2010) Enzymatic Interconversion of Ammonia and Nitrite: the Right Tool for the Job, *Biochemistry 49*, 8546-8553.

Chapter 2

Overexpression and Purification of ccNiR

2.1. Introduction

In order to obtain enough pure ccNiR to perform protein-intensive experiments, such as time resolved crystallography and EPR, an overexpression system was needed. However, ccNiR is a periplasmic multi- *c*-heme protein, and such proteins are notoriously difficult to overexpress using typical expression vectors in organisms such as *E. coli*. The difficulty arises because proper folding of these proteins requires significant post-translational manipulation by three specialized metabolic systems, each consisting of several channel and/or chaperone proteins. The complete *c*-heme protein assembling apparatus is illustrated in Figure 2.1 (*1*).
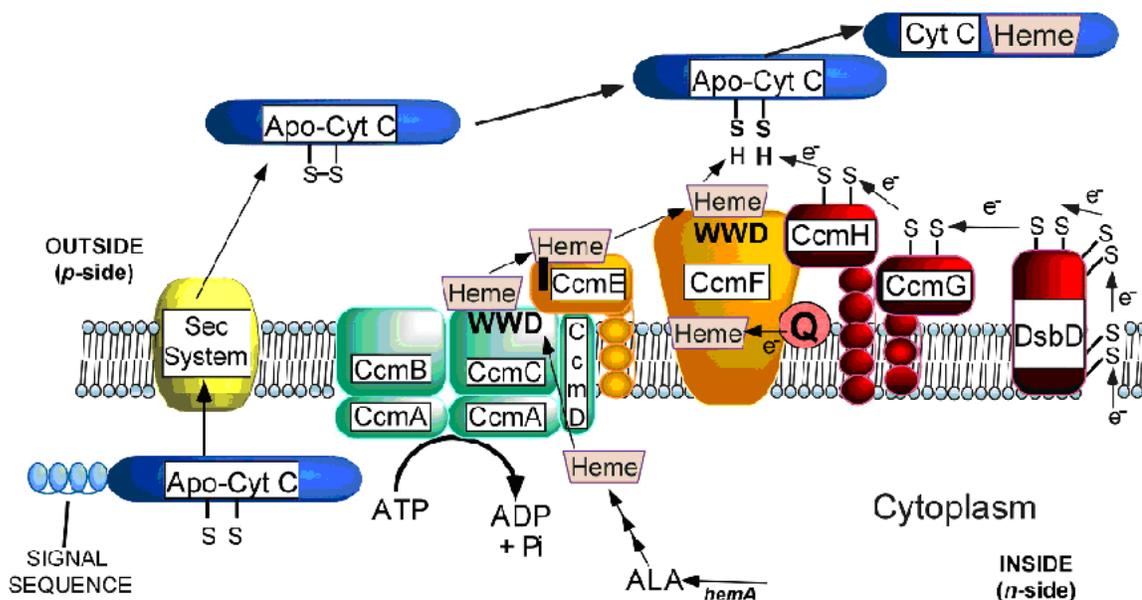
Figure 2.1. Depiction of the Cytochrome *c* Maturation (CCM) system (*1*).

Initially, soluble periplasmic proteins, such as ccNiR, must be transported from the cytoplasm, where translation takes place, to the periplasm. A protein channel system known as the Protein Secretion System (SEC) is believed to mediate the exportation process. Initially, transcribed periplasmic proteins contain an N-terminal periplasmic locating signal sequence that targets them to the SEC. The SEC system is comprised of two chaperone proteins, secAB, that recognize the N-terminal signal sequence, prevent the newly transcribed apoprotein from folding in the cytoplasm, and subsequently both initiate, and provide energy derived from ATP hydrolysis for, the secretion of this apoprotein through the inner membrane protein channel, secYEG (*2, 3*). Once the protein is secreted into the periplasm, the enzyme signal peptidase cleaves the N-terminal periplasmic locating sequence (*4*).

Once in the periplasm apoproteins can fold; however, proteins that need specialized cofactors for proper structure/function, such as *c*-heme proteins, require that these cofactors be loaded into them. Since *c*-heme proteins have the hemes covalently attached via thioether bonds between the vinyl sidechains of the hemes and cysteine residues in the protein, the cysteine residues must be in a reduced state for this to occur. In order for this to happen in the periplasm, the disulfide bond formation and isomerization (DSB) pathway is utilized (*5*). The DSB pathway consists of several soluble and membrane proteins located both in the cytoplasm and periplasm. The first step in the pathway is reduction of the disulfide bonds of thioredoxin by NADPH, a process that takes place in the cytoplasm and is mediated by thioredoxin reductase. The reducing equivalents are then transferred to the transmembrane protein dsbD (*6*), and subsequently to the Cytochrome *c* Maturation (CCM) system, which ultimately uses them

to reduce the cysteine residues in the apo- *c*-heme protein prior to incorporation of the heme.

The CCM system in Gram-negative bacteria consists of eight different types of membrane proteins that are directly involved in the covalent attachment of hemes to *c*-heme proteins (*7*). Once the heme has been synthesized in the cytoplasm from its main precursor, Δ-aminolevulinic acid, it is translocated into the periplasm using the ABC-type transporter ccmABC (Figure 2.1) (*1, 7*). At this point, the heme transport protein ccmE is recruited to the ccmABC complex via ccmD, and the heme is relayed to the shuttle protein (*1, 7*). Finally, all of the components required for heme incorporation into an apoprotein are then shuttled to the transmembrane protein ccmF, where the appropriate cysteine residues are reduced in the apoprotein, and the heme is covalently attached to the apoprotein by ccmF, resulting in the fully matured *c*-heme protein (Figure 2.1) (*1, 7*).

When trying to overexpress ccNiR, the novel fold of the lysine residue in the axial position of the active-site heme requires three additional chaperone proteins. These have been identified by Eaves et al. as nrfEFG (*8*), which in complex act as a heme lyase. These three proteins bring the total number of chaperones required specifically to overexpress ccNiR to eleven. Typical *E. coli* strains are capable of producing these chaperones, but do so only when the bacteria are growing anaerobically; under these conditions growth is slow, and final cell density is low, so efficient overexpression is not possible (*9*). Special *E. coli* strains have been devised that contain a CCM operon that is always turned on, but in order to express ccNiR the NRF operon would also have to be added to these bacteria. This chapter describes an alternative approach, in which *Shewanella oneidensis* was used as the expression host. Like *E. coli*, *S. oneidensis* is

easy to culture, and grows rapidly to high density; however, unlike *E. coli*, *S. oneidensis* naturally expresses all manner of *c*-hemes, including ccNiR, under aerobic conditions (*10*).

2.2. Materials and Methods

2.2.1. Overexpression of S. oneidensis ccNiR. A DNA sequence encoding for ccNiR was synthesized (Genscript) using codon optimization parameters derived from *E.coli*. The wild-type N-terminal signal peptide was replaced with the signal peptide from the *S. oneidensis* protein ''small tetraheme *c*'' (STC), which is constitutively expressed at high levels (*11, 12*). PCR was performed using Phusion® hot-start high-fidelity DNA polymerase (Finnzymes) and the primers ccNiRopt-F (5-GACTGAATTCGGAGGATACAATTA-3) and ccNiRopt-R (5-GATCTCTAGATCACTTGTAGGTCG-3). The resulting DNA fragment and the plasmid pHSG298 (TakaraBio) were digested with EcoRI and XbaI (New England Biolabs) and ligated using T4 DNA ligase (New England Biolabs). The plasmid construct was used to transform chemically competent NEB5-α cells (New England Biolabs). Positive transformants were selected for by plating onto LB agar plates containing 50 µg/mL kanamycin and screened using colony PCR. Plasmid DNA was isolated from the *E. coli* cells and used to transform electrocompetent *S. oneidensis* TSP-C cells (rifampicin-resistant) (*13*) via electroporation with a Gene Pulser MXcell™ electroporation system (Bio-Rad). Positive transformants were screened for by plating them onto LB agar plates containing 50 µg/mL kanamycin, 30 µg/mL rifampicin, and 20

mM MgSO$_4$. A single colony was used to inoculate a 5-mL overnight culture, which was then used to inoculate multiple 1-L cultures that were harvested after approximately 20 h of growth. Cell pellets were re-suspended in 50 mM N-(2-hydroxyethyl)piperazine-N-ethanesulfonic acid (HEPES) buffer, pH 7.0, containing 1 mM EDTA, 10 μM leupeptin, and 500 μM 4-(2-aminoethyl)benzenesulfonyl fluoride hydrochloride, and were then frozen at -80°C until needed.

2.2.2. Purification of S. oneidensis ccNiR from S. oneidensis TSP-C cells.

CcNiR-containing cells were lysed via sonication using a sonic dismembrator (model 500, Fisher Scientific), and centrifuged at 48,000 g for 15 min. Ammonium sulfate was added to the supernatant to obtain 50% saturation at 0°C (*14*), and the sample was centrifuged again as done before. The supernatant was applied to a 2.5 cm × 10 cm octyl-Sepharose column equilibrated with 20 mM HEPES, 1 mM EDTA, 3 M ammonium sulfate, pH 7.0 (buffer A). The column was first washed with buffer A, and then with 40% buffer B (20 mM HEPES, 1 mM EDTA, pH 7.0). In each case the wash continued until the absorbance at 280 nm (A$_{280}$) returned to the baseline. Finally, ccNiR was eluted with 80% buffer B. The ccNiR eluent was exchanged into buffer B using Ultracell® 10K molecular weight cutoff centrifugal filters (Millipore) via repeated concentration of the sample and dilution into buffer B. The sample was then applied to a 1.3 cm ×10 cm Q-Sepharose column and the flow-through was collected and exchanged into buffer C (20 mM HEPES, 1 mM EDTA, 2 M ammonium sulfate, pH 7.0) using centrifugal filters as previously described. The sample, concentrated to a volume of approximately 5 mL, was applied to a 1 mL RESOURCE isopropyl column (GE Healthcare), and eluted with a gradient from 0–40% buffer B. CcNiR typically eluted at 20–30% buffer B, exhibited an

A_{410}/A_{280} ratio of more than 3.8, and ran as a single band when analyzed by sodium

dodecyl sulfate polyacrylamide gel electrophoresis (Figure 2.2).
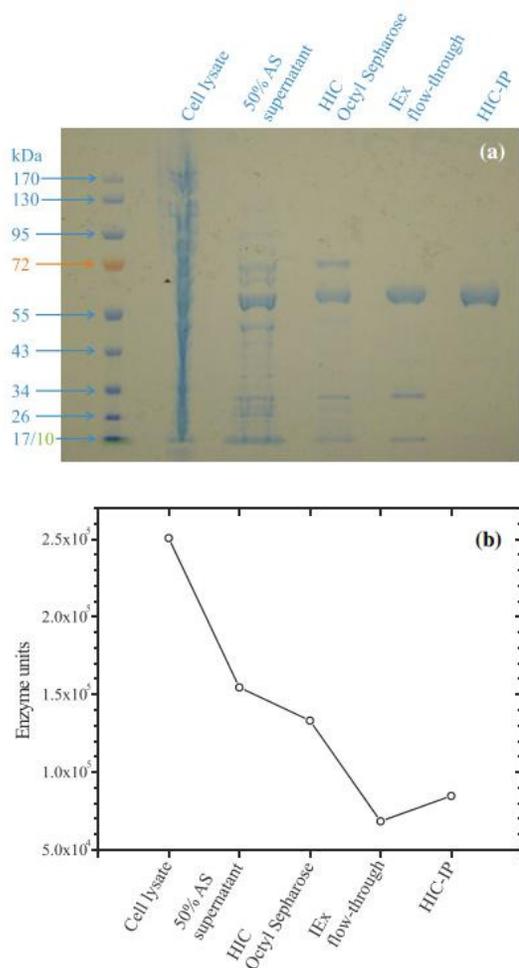
Figure 2.2. A: Sodium dodecyl sulfate polyacrylamide gel electrophoresis gel

documenting the ccNiR purification procedure. **B:** CcNiR activity recovered after each

purification step. One enzyme unit is the amount required to reduce 1 μmol nitrite per

minute under the assay conditions. AS - ammonium sulfate, HIC - hydrophobic

interaction chromatography, IEx - ion exchange chromatography, IP–isopropyl.

2.2.3. Steady-state kinetic analysis. Steady-state kinetic parameters for the

ccNiR-catalyzed reduction of nitrite or hydroxylamine by methyl viologen monocation

radical (MV_{red}) were obtained in a manner similar to that reported previously by Atkinson

et al (*15*). Briefly, MV_{red} was generated via bulk electrolysis of methyl viologen (MV) at

a potential of -550 mV versus the standard hydrogen electrode (SHE). An assay solution

buffered at pH 7.0 with 50 mM HEPES, and containing a known concentration of ccNiR

(typically 100 pM), approximately 75 µM MV_{red}, 1 mM MV, and varying substrate

concentration (2–500 µM for nitrite,0.5–250 mM for hydroxylamine), was then prepared

in a cuvette thermostated at 25°C. The final reagent added was MV_{red}, and its addition

initiated the reaction. The reoxidation of MV_{red} was monitored by tracking the

absorbance decrease at 600 nm in the visible spectrum. Reactions were completed

anaerobically in a nitrogen-filled glove box (O_2 below 2 ppm).

2.3. Results and Discussion.

2.3.1. Overexpression of ccNiR. Several approaches to overexpressing *S.*

oneidensis ccNiR were explored in this project. In the ultimately successful approach an

optimized ccNiR gene was incorporated into a pHSG298 vector for expression in *S.*

oneidensis (strain TSP-C). PHSG298 is very similar to pUC plasmids, except that the

latter use the ampicillin resistance gene as the selective agent for isolating transformed

cells, whereas pHSG298 uses the kanamycin resistance gene. Attempts to obtain

ampicillin-resistant colonies of *S. oneidensis* (containing ccNiR in a pUC18 plasmid)

were unsuccessful. The *S. oneidensis* TSP-C strain was used, as it has natural rifampicin

resistance and allows double antibiotic selection of transformed cells.

A comparison between the wild-type and optimized ccNiR genes is provided in

Appendix 1. The most notable difference between the two is that in the optimized gene

the ccNiR N-terminal signal sequence for periplasmic translocation has been replaced by

the signal sequence for another *S. oneidensis* protein, STC, which is typically expressed

in larger amounts than ccNiR (*12*). *S. oneidensis* cells transformed with the pHSG298

expression vector containing the optimized gene produced 20- to 30-fold more ccNiR

than untransformed cells. Typical yields were approximately 20 mg crude ccNiR per liter

of culture for the transformed cells, compared with 0.5–1 mg/L for the untransformed

cells. Significantly, *S. oneidensis* TSP-C cells transformed with pHSG298 plasmids

containing the wild-type ccNiR gene, complete with wild-type signal peptide, did not

produce ccNiR in concentrations above the background seen from chromosomal

expression.

Numerous strategies for the overexpression of multiheme *c*-type cytochromes

have been proposed (*12, 13, 16, 17*). Initially, *E. coli* would appear to be a good

organism to use for overexpressing *c*-heme proteins such as ccNiR, and indeed it has

been used with some success (*9, 17-19*). A major disadvantage of *E. coli* though is that it

expresses the eight cytochrome *c* maturation chaperones (ccmA-H) needed to incorporate

c-type hemes post-translationally into apoproteins only under anaerobic conditions.

Londer et al. overcame this problem by using an *E. coli* strain that contains the requisite

chaperones within the pEC86 vector; however, ccNiR requires an additional three

chaperones (nrfEFG) in order to correctly ligate lysine to the active-site heme, and *E. coli* only expresses these anaerobically (*8*).

S. oneidensis has also been used to overexpress *c*-hemes (*12, 13, 20-22*), and is in many ways a better host for this purpose. Crucially, unlike *E. coli*, this organism expresses both the ccmA-H and nrfEFG operons even under aerobic conditions. In a suitably overexpressing system, this makes *S. oneidensis* a potential source of large quantities of *c*-hemes, since bacteria typically grow much more rapidly and to higher density under aerobic conditions.

Takayama and Akutsu (*12*) recently used *S. oneidensis* to overexpress human cytochrome *c* by first substituting the human N-terminal signal peptide with that of the *S. oneidensis* protein STC. They proposed this strategy as a general one for the heterologous expression of c hemes within *S. oneidensis*. Our results suggest that in some cases it may be beneficial to change the N-terminal signal peptide prior to expression, even when the desired protein is from *S. oneidensis* and already has a signal peptide recognized by the bacterial cytochrome *c* maturation system. When we initially expressed the wild-type ccNiR gene, with its corresponding wild-type signal peptide, in *S. oneidensis*, the expression was no higher than the background seen from chromosomal expression. When the optimized gene bearing the STC signal peptide was used, expression was 20- to 30-fold above the background level. It is possible that the overexpression is due to better codon usage in the optimized gene, but for ccNiR the wild-type gene does not really show any obvious poor usage sections (see Appendix 1). Instead, we suspect that the STC signal peptide leads to more efficient post-translational modification of the associated protein than the ccNiR signal peptide. For example, the

protein responsible for translocating apoproteins across the periplasmic membrane might have more affinity for the STC signal peptide than for the ccNiR signal peptide. One can even see how such affinity variations might evolve: for proteins that are not needed by the bacteria in large quantities, such as the highly efficient ccNiR enzyme, there may be no evolutionary pressure to develop a signal peptide with high affinity for the translocation machinery.

The hypothesis that the rate of *c*-heme protein maturation can be increased by judicious choice of the signal peptide is worthy of more systematic investigation. Indeed it is possible that another signal peptide, such as that for the highly expressed *S. oneidensis* protein periplasmic fumarate reductase (SO2727), could in general lead to even higher overexpression than the STC peptide.

2.3.2. Purification of overexpressed ccNiR. CcNiR was obtained in high yield and purity using a five-step purification procedure. Most impurities were removed after the third step (hydrophobic interaction chromatography using octyl-Sepharose), as shown in Figure 2.2. One of the remaining impurities (approximately 70 kDa) was removed by passing the protein mixture through a Q-Sepharose anion exchange column, which does not bind ccNiR; this step also removed other minor impurities. A final hydrophobic interaction chromatography step using a high-resolution column brought all remaining impurities down to acceptable background concentrations (Figure 2.2). The overall yield for the purification was typically between 30 and 40% (Figure 2.2) of the initial activity. This translates to 7–10 mg pure ccNiR obtained per liter of cell culture, which is ample for protein-intensive experiments such as crystallography, EPR, or spectropotentiometry. The stability of the pure ccNiR was assessed using the steady-state assay described in the

following section. Micromolar solutions of the protein are stable for over 2 weeks at pH

7 and 4°C. Very dilute (nanomolar) solutions kept in microcentrifuge tubes appeared to

lose activity with half-lives of about 1.5 h. This apparent loss may be due to slight

adsorption of the protein into the matrix of the microcentrifuge tube. Alternatively ccNiR

in dilute solutions may slowly dissociate from an active dimeric to an inactive

monomeric form. The stability of pure ccNiR did not depend on the presence of added

Ca^{2+}.

2.3.3. Steady-state kinetic analysis of ccNiR. Steady-state kinetics for ccNiR-

catalyzed nitrite and hydroxylamine reduction by MV_{red} were obtained for the purified

protein. As expected, initial rates showed a first-order dependence on ccNiR

concentration, zero-order dependence on MV_{red} concentration, and hyperbolic

dependence on NO_2^- and NH_2OH concentrations. The K_m and k_{cat} values obtained from

Michaelis–Menten plots of V_o versus NO_2^- concentration were 23±4 μM and 824±33 s^{-1},

respectively, where the k_{cat} value reflects the number of micromoles of NO_2^- consumed

per second. For the V_o versus NH_2OH concentration plots, the corresponding K_m and k_{cat}

values were 8.3±2.4 mM and 2,380±160 s^{-1}, respectively, where the k_{cat} value now

reflects the number of micromoles of NH_2OH consumed per second. All of these values

are similar to the Michaelis–Menten parameters obtained for ccNiR from *E. coli* (K_m=28

μM and k_{cat}=770 s^{-1} for NO_2^- and K_m=30 mM and k_{cat}=2,380 s^{-1}for NH_2OH (*23*)).

It is conventional to express the various k_{cat} values for ccNiR in terms of the

nitrogenous species being reduced, as was done above. However, it is arguably more

meaningful to express k_{cat} for all nitrogenous species in terms of moles of electrons

transferred (or of MV_{red} oxidized, which is equivalent), allowing for the kinetic behavior

of these species to be compared using a single metric. Doing this for NO_2^- and NH_2OH reveals that the k_{cat} calculated in terms number of electrons transferred is essentially identical for the two reactions: 4620 s^{-1} for NO_2^- vs. 4760 s^{-1} for NH_2OH. This is an important observation because it shows that the rate limiting step in the six-electron reduction of NO_2^- is the final reduction of NH_2OH to NH_4^+; no step before that one is slower.

Initially, MV for use in the steady-state experiments was reduced using dithionite. However, sulfite, a product of dithionite oxidation, was recently shown to be a substrate for the *E. coli* ccNiR, being reduced to sulfide albeit at a very slow rate (*24*). To date we have not conclusively shown that the *S. oneidensis* ccNiR can catalyze the reduction of sulfite by MV_{red}; however, what is evident is that sulfite is a competitive inhibitor of the nitrite reduction by MV_{red}. Thus, in experiments where MV_{red} was generated by reduction with dithionite, the K_m values obtained were consistently higher than those obtained when MV_{red} was generated by bulk electrolysis. By contrast, the k_{cat} values were unaffected by the choice of protocol. The K_I value for sulfite inhibition of nitrite reductase activity was subsequently determined to be approximately 600 μM, by monitoring the dependence of the observed K_m on sulfite concentration in independent experiments (data not shown).

2.4. Summary

In the overall goal of performing time-resolved crystallography and other protein-intensive experiments, such as EPR and spectropotentiometry, on ccNiR, it was crucial to

establish a means to obtain a large amount of pure active enzyme. For this, an overexpression system in *S. oneidensis* was developed, which yielded ~20 mg of crude ccNiR per liter of culture, representing a 20- to 30-fold increase in ccNiR production compared to the wild-type organism. Additionally, an optimized purification scheme was established that gave an approximate 30-40% yield of pure protein relative to the crude lysate. Steady-state experiments were performed that showed that ccNiR from *S. oneidensis* behaves similarly to that of the previously characterized *E. coli* ccNiR. Interestingly, the results of these experiments also suggest that the final step in the six-electron reduction of nitrite to ammonia, which involves the two-electron reduction of hydroxylamine to ammonia, is probably the rate limiting step in catalysis.

2.5. References

1.   Richard-Fogal, C., and Kranz, R. G. (2010) The CcmC:Heme:CcmE Complex in Heme Trafficking and Cytochrome c Biosynthesis, *Journal of Molecular Biology 401*, 350-362.

2.   Douville, K., Price, A., Eichler, J., Economou, A., and Wickner, W. (1995) SecYEG and SecA Are the Stoichiometric Components of Preprotein Translocase, *Journal of Biological Chemistry 270*, 20106-20111.

3.   Hartl, F., Lecker, S., Schiebel, E., Hendrick, J. P., and Wickner, W. (1990) The binding cascade of SecB to SecA to SecY/E mediates preprotein targeting to the E. coli plasma membrane, *Cell 63*, 269-279.

4.   Zwizinski, C., and Wickner, W. (1980) Purification and characterization of leader (signal) peptidase from Escherichia coli, *Journal of Biological Chemistry 255*, 7973-7977.

5.   Kadokura, H., Katzen, F., and Beckwith, J. (2003) Protein Disulfide Bond Formation in Prokaryotes, *Annual Review of Biochemistry 72*, 111-135.

6.   Ito, K., and Inaba, K. (2008) The disulfide bond formation (Dsb) system, *Current Opinion in Structural Biology 18*, 450-458.

7.   Cianciotto, N. P., Cornelis, P., and Baysse, C. (2005) Impact of the bacterial type I cytochrome c maturation system on different biological processes, *Molecular Microbiology 56*, 1408-1415.

8.   Eaves, D. J., Grove, J., Staudenmann, W., James, P., Poole, R. K., White, S. A., Griffiths, L., and Cole, J. A. (1998) Involvement of products of the *nrfEFG* genes in the covalent attachment of haem *c* to a novel cysteine-lysine motif in the cytochrome c_{552} nitrite reductase from *Escherichia coli*, *Mol. Microbiol. 28*, 205-216.

9.   Londer, Y. Y., Pokkuluri, P. R., Tiede, D. M., and Schiffer, M. (2002) Production and preliminary characterization of a recombinant triheme cytochrome c_7 from *Geobacter reducens* in *E. coli*, *Biochim. Biophys. acta 1554*, 202-211.

10.   Beliaev, A. S., Thompson, D. K., Khare, T., Lim, H., Brandt, C. C., Li, G., Murray, A. E., Heidelberg, J. F., Giometti, C. S., Yates III, J., Nealson, K. H., Tiedje, J. M., and Zhou, J. (2002) Gene and Protein Expression Profiles of Shewanella oneidensis during Anaerobic Growth with Different Electron Acceptors, *OMICS: A Journal of Integrative Biology 6*, 39-60.

11. Tsapin, A. I., Nealson, K. H., Meyers, T., Cusanovich, M. A., van Beuumen, J., Crosby, L. D., Feinberg, B. A., and Zhang, C. (1996) Purification and properties of a low-redox-potential tetraheme cytochrome c_3 from *Shewanella putrefaciens*, *J. Bacteriol. 178*, 6386-6388.

12. Takayama, Y., and Akutsu, H. (2007) Expression in periplasmic space of *Shewanella oneidensis*, *Protein Expr. Purif. 56*, 80-84.

13. Ozawa, K., Yasukawa, F., Fujiwara, Y., and Akutsu, H. (2001) A Simple, Rapid, and Highly Efficient Gene Expression System for Multiheme Cytochromes *c*, *Biosci. Biotechnol. Biochem. 65*, 185-189.

14. Dawson, R. M. C., Elliot, D. C., and Jones, K. M. (1969) Data for Biochemical Research, Oxford University Press, London.

15. Atkinson, S. J., Mowat, C. G., Reid, G. A., and Chapman, S. K. (2007) An octaheme c-type cytochrome from Shewanella oneidensis can reduce nitrite and hydroxylamine, *FEBS Lett. 581*, 3805-3808.

16. Thony-Meyer, L., Fischer, F., Kunzler, P., Ritz, D., and Hennecke, H. (1995) *Escherichia coli* Genes Required for Cytochrome *c* Maturation, *J. Bacteriol. 177*, 4321-4326.

17. Londer , Y., Giuliani, S. E., Peppler, T., and Collart, F. R. (2008) Addressing *Shewanlella oneidensis* "cytochrome": the first step towards high-throughput expression of cytochromes *c*., *Prot. Expr. Purif. 62*, 128-137.

18. Londer, Y. Y., Pokkuluri, P. R., Erickson, J., Orshonsky, V., and Schiffer, M. (2005) Heterologous expression of hexaheme fragments of a multidomain

cytochrome from *Geobacter sulfurreducens* representing a novel class of cytochromes *c*, *Protein Expr. Purif. 39*, 254-260.

19. Londer, Y. Y., Pokkuluri, P. R., Orshonsky, V., Orshonsky, L., and Schiffer, M. (2006) Heterologous expression of dodecaheme "nanowire" cytochromes *c* from *Geobacter sulfurreducens*, *Protein Expr. Purif. 47*, 241-248.

20. Ozawa, K., Tsapin, A. I., Nealson, K. H., Cusanovich, M. A., and Akutsu, H. (2000) Expression of a tetraheme protein, *Desulfovibrio vulgaris* Miyazaki F Cytochrome c_3 in *Shewanella oneidensis* MR-1, *Appl. Environ. Microbiol. 66*, 4168-4171.

21. Shi, L., Lin, J. T., Markillie, L. M., Squier, T. C., and Hooker, B. S. (2005) Overexpression of multi-heme *c*-type cytochromes, *BioTechniques 38*, 297-299.

22. Shi, L., Chen, B., Wang, Z., Elias, D. A., Mayer, M. U., Gorby, Y. A., Ni, S., Lower, B. H., Kennedy, D. W., Wunschel, D. S., Mottaz, H. M., Marshall, M. J., Hill, E. A., Beliaev, A. S., Zachara, J. M., Fredrickson, J. K., and Squier, T. C. (2006) Isolation of a high-affinity functional protein complex between OmcA and MtrC: two outer membrane decaheme c-type cytochromes of Shewanella oneidensis MR-1., *J. Bacteriol. 188*, 4705–4714.

23. Bamford, V. A., Angove, H. C., Seward, H. E., Thomson, A. J., Cole, J. A., Butt, J. N., Hemmings, A. M., and Richardson, D. J. (2002) Structure and spectroscopy of the periplasmic cytochrome c nitrite reductase from Escherichia coli, *Biochemistry 41*, 2921-2931.

24.   Lukat, P., Rudolf, M., Stach, P., Messerschmidt, A., Kroneck, P., Simon, J., and Einsle, O. (2008) Binding and Reduction of Sulfite by Cytochrome *c* Nitrite Reductase, *Biochemistry 47*, 2080-2086.

Chapter 3

X-ray Crystallography of ccNiR

3.1. Introduction

In order to directly study the mechanistic differences between ccNiR and HAO, specialized techniques must be used since many of the catalytic processes of these enzymes occur on very fast (microsecond and millisecond) timescales. One such technique that has been developed in recent years is time-resolved X-ray crystallography using the Laue method (*1, 2*). A long-term goal in the ccNiR project is to study the nitrite reduction mechanism using this time-resolved method. In addition, as described below, the Laue method itself has some distinct advantages over more conventional crystallographic methods that the Pacheco and Schmidt groups hope to exploit in the coming years. This chapter describes the initial success in applying the Laue method to solve the structure of *S. oneidensis* ccNiR.

The Laue method differs fundamentally from current standard crystallography techniques in that it uses polychromatic rather than monochromatic X-rays (*1*). In addition, there are several important differences in the way that the Laue and monochromatic methods are currently applied in practice. In a standard crystallography experiment up to the entire crystal is illuminated by the X-ray beam, and data are collected over relatively long time-periods of up to several hours while systematically rotating the crystal, in order to sample a sufficient fraction of reciprocal space. By

contrast, in the modern incarnation of the Laue method, a diffraction pattern is obtained by irradiating the protein crystal with a succession of 1-10 intense polychromatic X-ray pulses, each lasting only ~100 ps (*2*). Furthermore, only a small portion of the protein crystal is illuminated by any given pulse. The number of pulses actually needed to collect a diffraction pattern is dependent on the quality of the protein crystal being imaged. As with all crystallography experiments, the number of diffraction patterns necessary to solve the crystal structure is dependent on the symmetry of the space group of that crystal. With polychromatic X-rays one can sample a large fraction of reciprocal space at once with a single pulse, while simultaneously collecting the entire integrated intensity of all the reflections in that volume, without the need to rotate the crystal. In practice one actually collects 1-10 successive 100 ps pulses during an exposure time of up to 800 ns at one orientation, and then rotates the crystal to sample a new part of reciprocal space. The data at each crystal orientation can be obtained using fresh crystal, not previously exposed to the X-ray beam, which is important for the reason discussed next.

When water-containing crystals are exposed to X-rays, electrons are photo-ejected from the solvent (*3-6*). These electrons are fairly mobile even at cryogenic temperatures and can reduce components of the protein, particularly metal centers such as hemes. Since heme proteins such as ccNiR and HAO tend to be redox active, using the standard monochromatic X-ray based technique could actually yield a distorted or blurred view of the protein, since at the beginning of data collection the protein would be fully oxidized, and then would become at least partially reduced as data collection progresses. At cryogenic temperatures this problem is partially mitigated because atoms tend to be

frozen in place even when oxidation states change. However, even at such temperatures it can be difficult to give credence to subtle structural features in the vicinity of redox-active centers, since such features could still be influenced by the oxidation state. Furthermore, over longer periods of time even the protein backbone will be reduced, at which point the diffraction pattern starts to fade. At temperatures of 0ºC and higher this problem is exacerbated because hydroxyl radicals and hydrogen generated by electron photo-ejection are then mobile and available to react with the proteins in the crystals.

The Laue method has a distinct advantage with regard to X-ray induced damage because the protein crystal is illuminated by the X-ray beam for only a short period of ~100 ps, during which a significant amount of structural information is acquired. During this short time period very little molecular movement or reduction can occur, and so one sees the protein essentially as it was prior to the X-ray pulse, even if reduction and structural damage occurs subsequently (*6*). Furthermore, because only a small fraction of the crystal volume is irradiated to obtain a given data point, one can move the crystal after each X-ray pulse in order to expose a fresh volume for the each acquisition. In this way, the 1-10 data points needed to obtain a diffraction pattern can often be collected using one crystal, while at the same time ensuring that each point is collected from pristine protein.

Time-resolved crystallography also takes advantage of the Laue method's unique features (*2, 6*). In this method a crystal is first mounted on the goniometer, and then a reaction is photo-initiated within the crystal by illuminating a small region of that crystal with an intense laser pulse. After a defined time, Δt, the same region of the crystal that was illuminated by the laser pulse is probed with a polychromatic X-ray beam. This will

provide information about the structural changes that have occurred in the protein from the moment that the reaction was photo-initiated until it was probed with the X-ray beam. By moving the crystal and repeating this process 1-10 times, all of the data needed to obtain a diffraction pattern at this Δt can be collected. The experiment is then repeated until all diffraction patterns are obtained that are necessary to solve the crystal structure at this time point. Then, by repeating this experiment several times and changing the Δt, a series of crystal structures can be obtained along the reaction coordinate. When this series of crystal structures is compiled, an atomic-resolution movie of the catalytic process can be obtained. This allows direct study of the mechanisms of enzymes, such as ccNiR and HAO, which operate on very fast time-scales.

3.2. Materials and Methods

3.2.1. Crystallization of S. oneidensis MR-1 ccNiR. Initial crystallization screens were performed on ccNiR in the laboratory of Dr. J. Fu (Medical College of Wisconsin) using a robotic high-throughput screening system, and the custom in-house screen MCW192. Crystals were obtained from solutions containing 50 mM triethanolamine at pH 8.25 with 19% PEG 4,000. Further optimization of the crystallization conditions was then performed using the hanging drop method, where 2-µL drops were prepared by mixing 1 µL ccNiR stock with 1 µL precipitant solution, and suspended over a reservoir containing 500 µL precipitant. Optimal crystals were obtained when the ccNiR stock had a concentration of 10 mg/mL, whereas the precipitant consisted of a solution containing 50 mM triethanolamine and 14% PEG 4,000, pH 8.25. Trays of hanging drop samples

were incubated at 23°C. Crystals typically appeared overnight. The onset of crystal

formation appears to be critically dependent on the temperature; no change in drop

appearance was observed at temperatures above 23°C, whereas below this temperature

liquid–liquid phase separation invariably occurred. Some batches of purified protein

resisted crystallization even at 23°C. In such cases micro-seeding as follows proved

useful. Previously grown crystals were pulverized in mother liquor using a 3-mL tissue

grinder (Wheaton), and were then mixed 1:1 with the ccNiR crystallization solution

described above. This solution was incubated at 25°C for 6–18 h, and then slowly cooled

by transferring the sample to a 20°C room. Crystals grown in this manner typically

appeared in 2–3 days.

3.2.2. Crystallographic data collection. Crystals with dimensions of 200 μm x 60

μm x 60 μm were grown as described in the previous section. For conventional

crystallographic analysis, crystals were cryoprotected by transferring them to a solution

of mother liquor supplemented with 10% (w/v) PEG 20,000, and then flash-frozen.

Monochromatic crystallographic data to a resolution of 3.2 Å were collected at BioCARS

14BM-C beamline at cryogenic temperatures (100 K) using an ADSC Q315 detector.

Data were collected in 0.5° steps for a total of 180°. Data were analyzed by Mosflm (*7*)

and scaled and merged by the Collaborative Computational Project Number 4 (CCP4)

program scala (*8*). Crystals appeared to be monoclinic, space group $P2_1$, with cell

parameters a = 47.1 Å, b = 92.7 Å, c = 216.5 Å, a = 90°, b = 91.04°, and c = 90°. Data

statistics are given in Table 3.1.

Laue crystallographic data were collected at the Bio-CARS 14ID-B Laue

beamline using X-ray radiation from a double undulator (U23 and U27 (*9*)). Crystals

were mounted in glass capillaries, and data were collected at 0°C. The synchrotron

operated in hybrid mode, and radiation from a single electron bunch was selected. Each

X-ray pulse contained about 3×10^{10} photons, and seven pulses were used per Laue

diffraction pattern. After each Laue pattern had been obtained, the crystal was translated

along its long axis to expose a fresh volume of crystal to the X-ray beam. The X-ray

beam size was 90 μm × 60 μm. Laue data extended to a resolution of 2.59 Å with

sufficient completeness to 2.72 Å. The complete data set consisted of 90 Laue patterns

covering 180°. Data were indexed, integrated, and scaled by Precognition/Epinorm

(Renz Research). The space group was deter-mined to be $P2_12_12_1$, orthorhombic, with

cell parameters a = 51.5 Å, b = 95.5 Å, c = 223.0 Å, a = 90°, b = 90°, and c = 90°. Data

statistics of the Laue data are also given in Table 3.1.

	Monochromatic	Laue
Temperature (K)	100	273
Crystal size	60 μm × 60 μm × 200 μm	60 μm × 60 μm × 200 μm
Mosaicity (°)	0.9[a]	<0.1[a]
Resolution (Å)	3.20	2.72
Cell parameters	a = 47.1 Å, b = 92.7 Å, c = 216.5 Å, α = 90°, β = 91.04°, γ = 90°	a = 51.5 Å, b = 95.5 Å, c = 223.0 Å, α = 90°, β = 90°, γ = 90°
V_{cell} (Å³)	945,120	1,096,769
Space group	$P2_1$ monoclinic	$P2_12_12_1$ orthorhombic
R_{sym} (%)	21.9	9.9
$I/\sigma(I)$	2.3	16.7
Redundancy	2.9	8.9
Completeness (last shell)	73.9% (63.8%, 3.37–3.20 Å)	75.2% (63.5%, 2.86–2.72 Å)
Models for molecular replacement	Escherichia coli ccNiR (PDB ID 2RDZ) subunits A and B	E. coli ccNiR oriented and refined against monochromatic data subunits A and B
Asymmetric unit	Tetramer	Dimer
R_{cryst}/R_{free} (%)		
Molecular replacement	47.7 (to 3.5 Å)	31.1 (to 2.59 Å)[b]
Rigid body	41.1 (to 3.2 Å)	25.6
Refinement (no water)	32.9/37.8	21.6/26.7
Protein plus water		19.7/25.7

ccNiR cytochrome c nitrite reductase, PDB Protein Data Bank

[a] As estimated by the data reduction program. The Laue value was estimated from shape of the reflection; monochromatic and Laue values also contain contributions from beam geometry (crossfire) that might be slightly different at beamlines 14-IDB and 14-BMC
[b] Refinement includes all data to 2.59 Å

Table 3.1. Crystallography data and refinement statistics.

3.3. Results and Discussion

3.3.1. Crystal structure model building and refinement. The data analysis

described in this section was performed by Dr. Vukica Srajer of the University of

Chicago and Prof. Marius Schmidt of the UWM Physics department. For an initial

molecular replacement the monoclinic ($P2_1$) monochromatic data obtained at 100 K were

used. The A and B subunits (one dimer) of the *E. coli* ccNiR without water or calcium

ions were used as a template (*E. coli* ccNiR Protein Data Bank ID 2RDZ). Molecular

replacement was attempted to 3.5 Å using the CCP4 program phaser (*10*). One solution

comprising two dimers was identified. The molecular replacement solution was quickly

refined using refmac5 (CCP4 program collection (*8*)) by rigid-body and by conventional

refinement including non-crystallographic symmetry restraints. R_{cryst} settled to 32.9%.

No further refinement was attempted owing to the poor data quality. However, one dimer

consisting of sub-units A and B of this initial model was then used for molecular

replacement against the Laue data collected at room temperature. A single, distinct

molecular replacement solution was found in the orthorhombic crystal form. After rigid-

body refinement of individual subunits A and B, the resulting model was inspected at

positions where differences in the sequence between *E. coli* and *S. oneidensis* ccNiR

occur. Differences were immediately visible in the electron density, and the atomic

model was modified according to the correct *S. oneidensis* ccNiR sequence. All model

manipulations were done using coot (*11*). The electron density map around residues 170

and 220 could be easily retraced. Both regions accommodate loops which are different in

E. coli and *S. oneidensis* ccNiR. Very large difference electron density within the protein

indicated the presence of a strong scatterer. The electron density was modeled by a

calcium ion in accordance with similar findings for the *E. coli* and other ccNiRs

previously characterized crystallographically. Finally, water molecules were inserted.

The final *R* factor dropped to 19.7% (see Table 3.1).

Attempts to solve the ccNiR structure using mono-chromatic crystallographic data

collected at cryogenic temperatures (100 K) were considerably less successful than those

using the Laue method on data collected at 0°C. A variety of cryo-protectants were

tested, including glycerol, 2-methyl-2,4-pentanediol, PEG 400, PEG 8,000, PEG 20,000,

mineral oil, and various mixtures of these. The best results were obtained using 10%

PEG 20,000 as the cryo-protectant; however, even with this cryo-protectant very weak

monochromatic data were collected—see $I/\sigma(I)$ and *R* merge in Table 3.1. Multiple

attempts to collect better monochromatic data failed. At room temperature the diffraction

patterns fade away after a few degrees. When comparing the room-temperature Laue

data with the cryogenic monochromatic data, one can observe differences in cell

parameters as large as 6.5 Å. In addition, freezing increases the mosaicity. It is difficult

to estimate the mosaicity from the size of the Laue reflections since factors such as

crystal size and crossfire also contribute. However, the software Precognition estimated

the mosaicity to be around 0.1°, which usually yields good Laue patterns. Freezing then

increases the mosaicity to around 1°.

The ccNiR crystallizes as dimers, which form the building blocks of both the

orthorhombic and the monoclinic crystals. Two dimers occupy similar places in both

space groups; however, numerous contacts are established between subunits of individual

dimers, whereas there are few contacts between two distinct dimers. In space group

$P2_12_12_1$, individual dimers are related by crystallographic symmetry, whereas in space

group $P2_1$, two dimers reside in the same asymmetric unit. The difference is that in space group $P2_1$ the second dimer is rotated slightly relative to the corresponding dimer position in the orthorhombic form (see Appendix 2). Hence, freezing generates strain in the crystals that breaks the symmetry and increases the mosaicity, although the molecular packing in both crystals remains almost the same. These factors contribute to disorder in the crystals at cryogenic temperatures, increase (decrease) the temperature factor (the Debye–Waller factor), and hence contribute to the limited resolution and poor monochromatic data quality.

3.3.2. Structure of S. oneidensis ccNiR. Structure determination of *S. oneidensis* ccNiR reveals what to our knowledge may be the first case in which polychromatic Laue X-ray data collected at 0°C proved to be superior to monochromatic data collected at cryogenic temperatures. Without Laue crystallography we would have been limited to relatively low quality data with a resolution limit lower than 3 Å. The biggest challenge in cryo-crystallography is to find a good cryo-protectant. If this is difficult, and the overall crystal quality is poor in the first place, most data sets are of low quality and must be discarded. In addition, crystals even from the same batch often do not scatter equally well. Room-temperature monochromatic data collection with crystals held in capillaries or freely mounted using a humidifier (*12*) offers one possible solution. Since the crystals are not frozen, there is little strain that might generate disorder and increased mosaicity, and consequently data quality can be extremely good. However, we were unable to collect complete monochromatic room-temperature data on this ccNiR because after a few exposures the diffraction patterns fade away. Laue crystallography offers an alternative when monochromatic data collection at ambient or cryogenic temperatures

obstinately fails. Laue crystallography tends to minimize damage to the crystal caused by

the ionizing X-rays. Several publications have reported the effect of X-ray dose and dose

rate on protein crystals (*6, 13, 14*). The dose tolerance depends on the rate at which the

X-ray dose is administered. The higher the rate, the higher the tolerance (*13*), up to a

certain limit where temperature increase and, presumably, hydrogen formation destroys

the crystal rapidly (*14*). Single-pulse Laue crystallography exhibits the highest peak dose

rates for synchrotrons (on the order of 10^{13} Gy/s, (*6*)), but there is enough waiting time

between the X-ray pulses to allow the temperature to equilibrate and potential hydrogen

to diffuse out of the crystal. The combination of ultrashort brilliant X-ray pulses and the

displacement of the crystal along its axis to expose a fresh crystal volume proved to be

very advantageous for successful collection of high-resolution data on this ccNiR.

Crystal structures of ccNiR were previously reported from three different

branches of the bacterial phylogenetic tree (*15-21*). *Sulfurospirillum deleyianum* and

Wollinella succinogenes are ε-proteobacteria, *Desulfovibrio desulfuricans* and *D.*

vulgaris are δ-proteobacteria, and *E. coli* and *S. oneidensis* are γ-proteobacteria (*16, 19*).

All structures reported so far, including the *S. oneidensis* form described herein, appear to

be functional dimers, and exhibit highly conserved heme arrangements. Figure 3.1 shows

an overlay of the *S. oneidensis* hemes within one monomer with the corresponding *E. coli*

hemes. The arrangements of the histidine imidazole planes are of note because they often

permit correlations to be made between a heme protein's structure and its EPR

spectroscopic features (*18, 22*). The imidazole planes of heme 2 are very nearly parallel

in all of the ccNiRs reported to date, whereas the imidazole planes of hemes 4 and 5 are

closer to perpendicular. Each of these arrangements gives rise to a distinct type of EPR

spectrum. The imidazole arrangement of heme 2 is more variable than that of the other hemes, being the most parallel in the *S. oneidensis* protein and less so in other ccNiRs. This heme is typically magnetically coupled to the high-spin active site, and thus exhibits an anomalous EPR signature (*18*).
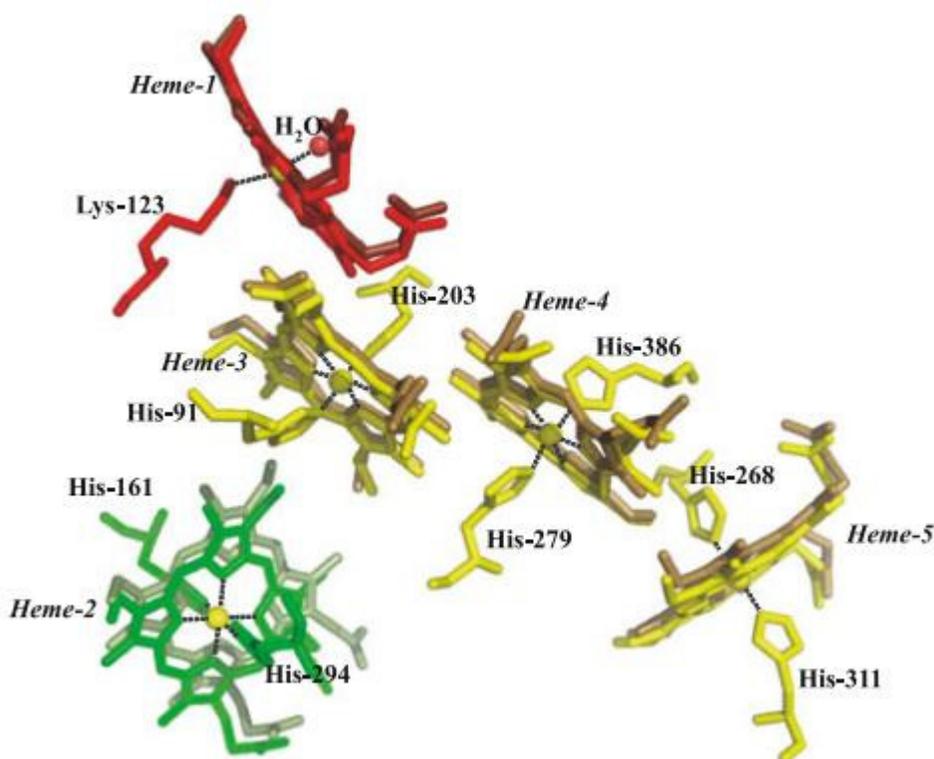
Figure 3.1. Comparison between the heme arrangement within a monomer of *S. oneidensis* ccNiR (lighter shade) and that within a monomer of *E. coli* (darker shade). Subunit A is shown. Iron atoms are shown in yellow. Red hemes are the active site, yellow hemes are *bis*-histidine ligated with perpendicular imidazoles, and green hemes are *bis*-histidine ligated with parallel imidazoles and are where ccNiR presumably interacts with its physiological electron donor.

In addition to sharing a common heme arrangement, all ccNiRs reported to date contain a Ca^{2+} ion that lies close to the active site in a highly conserved region of the protein (*16*). Figure 3.2 shows the environment of the Ca^{2+} ion in *S. oneidensis* ccNiR. The ion is coordinated in bidentate fashion by Glu-205, and in monodentate fashion by the Tyr-206 and Lys-254 backbone carbonyls, and the Gln-256 side-chain carbonyl. In other ccNiRs, two remaining (cis-oriented) coordination sites are occupied by water molecules; however, in the *S. oneidensis* structure we only assigned one water molecule to the Ca^{2+} ion in subunit B. In subunit A the difference electron density that represents this water molecule is very close to the noise level, and it is difficult to identify even one water molecule there. The carbonyl side chain of Asp-242 and the hydroxyl of Tyr-235 are close to the open calcium coordination sites, but are not within bonding distance. Instead they interact with the water molecule that is weakly coordinated to the Ca^{2+} ion (see Figure 3.2). The ccNiR calcium ions appear to play a vital role in organizing the active site (*16*), and at least in the case of the *E. coli* protein, mutations to the Ca^{2+}-binding amino acids have been shown to affect the active-site heme midpoint potential (*23*). In the case of ccNiR from *S. deleyianum*, enzyme activity increased in the presence of added calcium, and decreased when chelators such as EDTA were added to the buffers (*24*). However, the *S. oneidensis* enzyme showed no activity dependence on added calcium, or on the presence of added EDTA. It is not clear from structural comparisons why the Ca^{2+} ion should be labile in one case and not the other, as the calcium environment is so similar in both cases. In addition to the binding site conserved within all ccNiRs, the ccNiRs from *D. desulfuricans* and *D. vulgaris* exhibit a second, well-defined Ca^{2+} binding site near hemes 3 and 4 (*19, 20*). The *E. coli* enzyme crystal

structure exhibits a second Ca^{2+} ion in the same relative position, but the binding site in this case is not as clearly defined, and it is unclear if the calcium is physiologically relevant (*18*). We did not detect a second Ca^{2+} ion in *S. oneidensis* ccNiR, perhaps simply because Ca^{2+} was not included in the crystallization buffer.
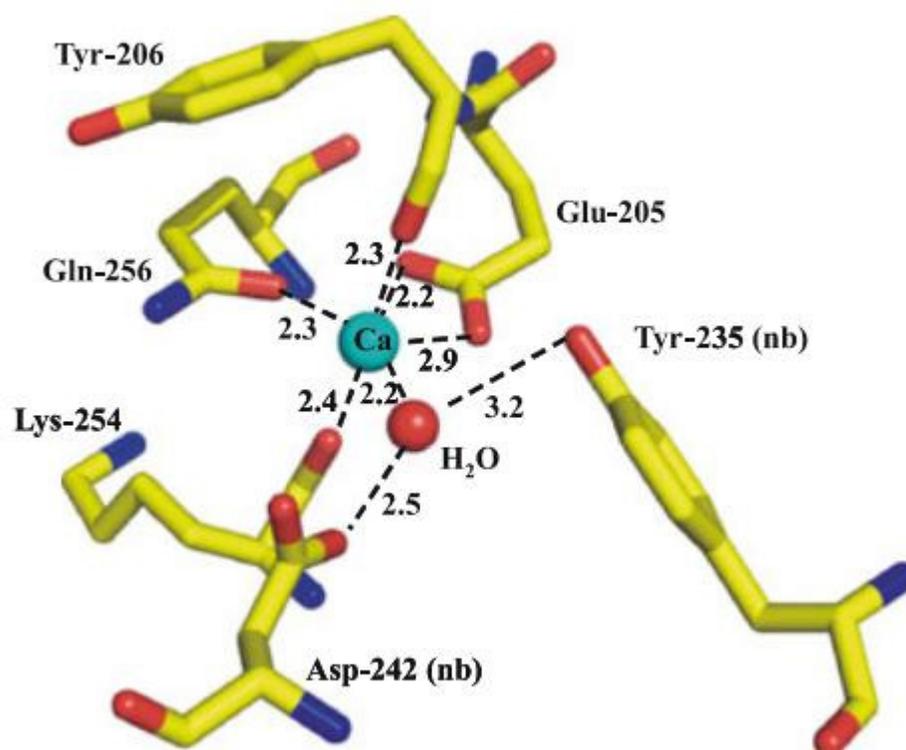
Figure 3.2. Coordination environment of the conserved Ca^{2+} site within the *S. oneidensis* ccNiR. Subunit B is shown here; in subunit A the difference electron density feature that corresponds to the Ca^{2+}-bound water is only 3.5σ. This is extremely close to the noise level, and consequently the water molecule was left out of the structure. The *E. coli* structure revealed two water molecules bound to the Ca^{2+} ion.

Overall, the *S. oneidensis* ccNiR structure is very similar to that of *E. coli* ccNiR; the structures are compared in Figure 3.3. When corresponding subunits of *E. coli* and *S. oneidensis* ccNiRs are compared, the root mean square deviation between the C_α atoms is 0.7 Å with 64% sequence identity (*25*). The small rectangle in Figure 3.3 highlights the region where the greatest sequence divergence is found. This region of the protein, which borders heme 2, was long suspected to be the entry point for electrons into ccNiR (*16*); more recently, a crystal structure of *D. vulgaris* ccNiR bound to its physiological partner has all but confirmed this hypothesis (*21*). The ccNiRs from the different phylogenetic branches use different physiological electron acceptors, which probably explains why the region around heme 2 generally shows significant interspecies sequence variability. CcNiRs from δ-proteobacteria and ε-proteobacteria use NrfH, a membrane-bound quinol dehydrogenase, as the electron donor, whereas γ-proteobacteria normally use a soluble electron transport protein known as NrfB to shuttle electrons from the membrane-bound quinol dehydrogenase to ccNiR (*16*). *S. oneidensis* and *E. coli* are both γ-proteobacteria; however, *S. oneidensis* ccNiR is unusual in that its electron donor is a membrane-bound tetraheme protein called CymA, rather than the more common NrfB (*26*). *Shewanella* species appear to have evolved to use a large number of physiological electron donors interchangeably. Accordingly, CymA appears to be a general-purpose protein that can donate electrons equally well to a variety of proteins, such as ccNiR, and nitrate, fumarate, and dimethyl sulfoxide reductases among others (*26*).
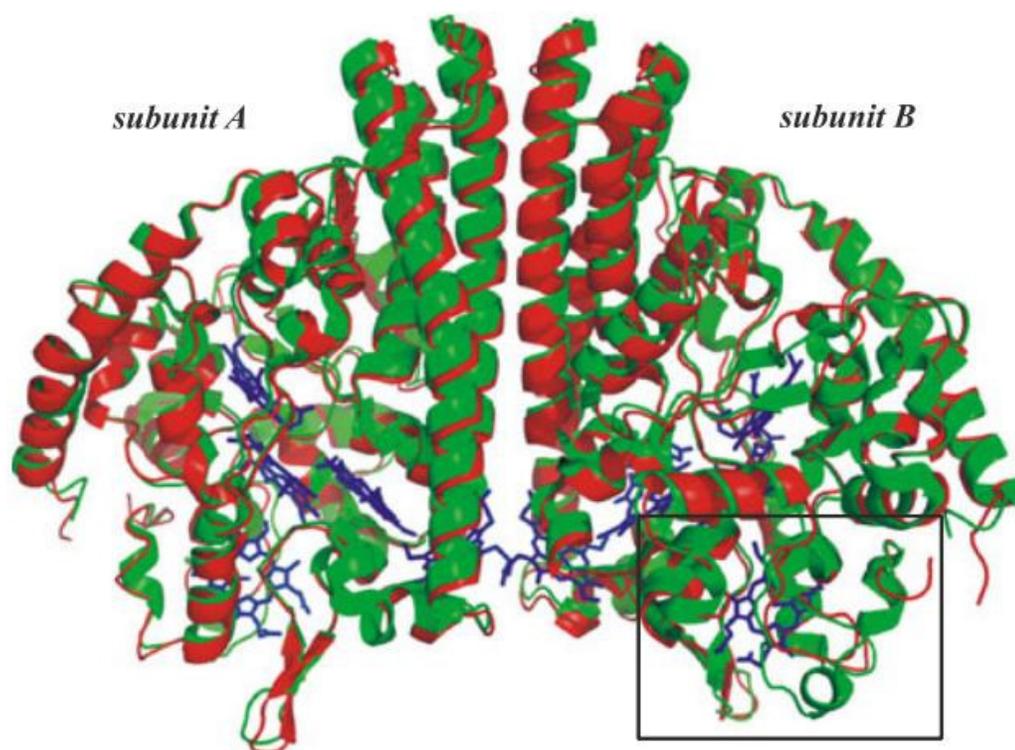
Figure 3.3. Overlay comparing the protein structures of *S. oneidensis* and *E. coli* ccNiRs. The rectangle highlights the region near heme 2 that shows the greatest sequence divergence.

3.4. Summary

The crystallography experiments described here represent a major step in the progress towards the goal of performing time-resolved crystallography on ccNiR. After several rounds of crystal screens and subsequent optimization, high quality crystals of ccNiR were obtained. However, these crystals proved to be inadequate for use with traditional cryo-crystallography methods, yielding data with a resolution limit of >3 Å. Fortunately, these ccNiR crystals proved to be compatible with the Laue crystallography

technique, allowing for the structure of the *S. oneidensis* ccNiR to be solved to the resolution limit of 2.59 Å. To date, we are aware of no other crystal structures of proteins that have been solved via Laue crystallography prior to being solved by traditional methods. Additionally, by comparing the structure of the ccNiR from *S. oneidensis* to the previously solved structure of the *E. coli* ccNiR, it was determined that while both structures are quite similar there is a region of divergence that is likely attributed to each of these ccNiRs having a different physiological electron donor in their respective host organisms.

2.5. References

1. Ren, Z., Bourgeois, D., Helliwell, J. R., Moffat, K., Srajer, V., and Stoddard, B. L. (1999) Laue crystallography: coming of age, *J. Synchrotron Rad. 6*, 891-917.

2. Schmidt, M. (2008) Structure Based Enzyme Kinetics by Time-Resolved X-ray crystallography, In *Ultrashort Laser Pulses in Medicine and Biology* (Zinth, W., Braun, M., and Gilch, P., Eds.), Springer Verlag.

3. Ravelli, R. B. G., and McSweeney, S. M. (2000) The "fingerprint" that X-rays can leave on structures, *Structure 8*, 315-328.

4. Pearson, A. R., Pahl, R., Kovaleva, E. G., Davidson, V. L., and Wilmot, C. M. (2007) Tracking X-ray derived redox changes in crystals of a methylamine dehydrogenase/amicyanin complex using single-crystal UV/Vis microspectrophotometry, *J. Synchrotron Rad. 14*, 92-98.

5. Beitlich, T., Kuhnel, K., Schulze-Briese, C., Shoeman, R. L., and Schlichting, I. (2007) Cryoradiolytic reduction of crystalline heme proteins: analysis by UV/Vis spectroscopy and X-ray crystallography, *J. Synchrotron Rad. 14*, 11-23.

6. Schmidt, M., Šrajer, V., Purwar, N., and Tripathi, S. (2012) The Kinetic Dose Limit in Room Temperature Time-resolved Macromolecular Crystallography, *J. Synchrotron Rad. 19*, Available online, Jan 2012.

7. Battye, T. G., Kontogiannis, L., Johnson, O., Powell, H. R., and Leslie, A. G. W. (2011) iMOSFLM: a new graphical interface for diffraction-image processing with MOSFLM, *Acta Cryst. D 67*, 271-281.

8. Collaborative Computational Project Number 4. (1994) The ccp4 suite: programs for protein crystallography, *Acta Cryst. D 50*, 760-763.

9. Graber, T., Anderson, S., Brewer, H., Chen, Y. S., Cho, H. S., Dashdorj, N., Henning, R. W., Kosheleva, I., Macha, G., Meron, M., Pahl, R., Ren, Z., Ruan, S., Schotte, F., Rajer, V. S., Viccaro, P. J., Westferro, F., Anfinrud, P., and Moffat, K. (2011) BioCARS: a synchrotron resource for time-resolved X-ray science., *J. Synchrotron Rad. 18*, 658-670.

10. McCoy, A. J., Grosse-Kunstleve, R. W., Adams, P. D., Winn, M. D., Storoni, L. C., and Read, R. J. (2002) Phaser crystallographic software, *J. Appl. Cryst. 40*, 658-674.

11. Emsley, P., Lohkamp, B., Scott, W. G., and Cowtan, K. (2010) Features and development of Coot, *Acta Cryst. D66*, 486-501.

12. Kiefersauer, R., Than, M. E., Dobbek, H., Gremer, L., Melero, M., Strobl, S., Dias, J. M., Soulimane, T., and Huber, R. (2000) A novel free-mounting system

for protein crystals: transformation and improvement of diffraction power by accurately controlled humidity changes, *J. Appl. Cryst. 33*, 1223-1230.

13. Southworth-Davies, R. J., Medina, M. A., Carmichael, I., and Garman, E. F. (2007) Observation of decreased radiation damage at higher dose rates in room temperature protein crystallography, *Structure 15*, 1531-1541.

14. Rajendran, C., Dworkowski, F. S., Wang, M., and Schulze-Briese, C. (2011) Radiation damage in room-temperature data acquisition with the PILATUS 6M pixel detector, *J. Synchrotron Rad. 18*, 318-328.

15. Einsle, O., Messerschmidt, A., Stach, P., Bourenkov, G. P., Bartunik, H. D., Huber, R., and Kroneck, P. M. H. (1999) Structure of cytochrome c nitrite reductase, *Nature 400*, 476-480.

16. Einsle, O., Stach, P., Messerschmidt, A., Simon, J., Kroger, A., Huber, R., and Kroneck, P. M. H. (2000) Cytochrome c nitrite reductase from Wolinella succinogenes - Structure at 1.6 angstrom resolution, inhibitor binding, and heme-packing motifs, *J. Biol. Chem. 275*, 39608-39616.

17. Pereira, I., LeGall, J., Xavier, A., and Teixeira, M. (2000) Characterization of a heme *c* nitrite reductase from a non-ammonifying microorganism, *Desulfovibrio vulgaris* Hildenborough, *Biochim. Biophys. Acta 1481*, 119-130.

18. Bamford, V. A., Angove, H. C., Seward, H. E., Thomson, A. J., Cole, J. A., Butt, J. N., Hemmings, A. M., and Richardson, D. J. (2002) Structure and spectroscopy of the periplasmic cytochrome c nitrite reductase from Escherichia coli, *Biochemistry 41*, 2921-2931.

19. Cunha, C. A., Macieira, S., Dias, J. M., Almeida, G., Goncalves, L. L., Costa, C., Lampreia, J., Huber, R., Moura, J. J. G., Moura, I., and Romao, M. J. (2003) Cytochrome c nitrite reductase from Desulfovibrio desulfuricans ATCC 27774 - The relevance of the two calcium sites in the structure of the catalytic subunit (NrfA), *J. Biol.Chem. 278*, 17455-17465.

20. Rodrigues, M. L., Oliveira, T., Matias, P. M., Martins, C., Valente, F. M., Pereira, I. A., and Archer, M. (2006) Crystallization and preliminary structure determination of the membrane-bound complex cytochrome c nitrite reductase from Desulfovibrio vulgaris Hildenborough, *Acta Cryst. F 62*, 565-568.

21. Rodrigues, M., Oliveira, T., Pereira, I., and Archer, M. (2006) X-ray structure of the membrane-bound cytochrome *c* quinol dehydrogenase NrfH reveals novel haem coordination, *EMBO Journal 25*, 5951-5960.

22. Walker, F. A. (1999) Magnetic spectroscopic (EPR, ESEEM, Mossbauer, MCD and NMR) studies of low-spin ferriheme centers nad their corresponding heme proteins, *Coord. Chem. Rev. 186*, 471-534.

23. Clarke, T. A., Kemp, G. L., Van Wonderen, J. H., Doyle, R. A. S., Cole, J. A., Tovell, N., Cheesman, M. R., Butt, J. N., Richardson, D. J., and Hemmings, A. M. (2008) Role of a conserved glutamine residue in tuning the catalytic activity of *Escherichia coli* Cytochrome *c* nitrite reductase, *Biochemistry 47*, 3789-3799.

24. Stach, P., Einsle, O., Schumacher, W., Kurun, E., and Kroneck, P. M. H. (2000) Bacterial cytochrome *c* nitrite reductase: new structural and functional aspects, *J. Inorg. Biochem. 79*, 381-385.

25. Holm, L., and Park, J. (2000) DaliLite workbench for protein structure comparison, *Bioinformatics 16*, 566-567.

26. Gao, H., Yang, Z. K., Barua, S., Reed, S. B., Romine, M. F., Nealson, K. H., Fredrickson, J. K., Tiedje, J. M., and Zhou, J. (2009) Reduction of nitrate in *Shewanella oneidensis* depends on atypical NAP and NRF systems with NapB as a preferred electron transport protein from CymA to NapA, *ISME Journal 3*, 966-976.

Chapter 4

Photo-reduction of wild-type and labeled ccNiR

4.1. Introduction

For time resolved crystallography, a means of photo-initiating a reaction in a protein crystal is needed. Several methods exist for photo-initiating a variety of reactions (*1-4*), though only a handful have ever been used to initiate a reaction within a crystal (*1, 5-7*). Currently, our research group is focused on the study of reductive reactions that ccNiR and HAO catalyze (Scheme 4.1). A well characterized system for the photo-initiation of reductive reactions uses the chromophore tris(bipyridine)ruthenium(II) ($Ru(bpy)_3^{2+}$) (Figure 4.1) (*8, 9*). In this system, $Ru(bpy)_3^{2+}$ is photo-excited in the presence of a sacrificial electron donor, such as EDTA, to generate two reducing equivalents for every one $Ru(bpy)_3^{2+}$ that is photo-excited (See Discussion Section). While this approach works well for studying reductive reactions in solution, it may not be optimal to reduce a protein crystal for several reasons. In order to use $Ru(bpy)_3^{2+}$ in a protein crystal, either the chromophore would have to be soaked into the crystal or co-crystallized with the protein. The difficulty in soaking $Ru(bpy)_3^{2+}$ into the crystal is its relatively large size (678 g/mol) and low solubility (<10 mM) in aqueous solutions at pH 7. As a rule of thumb, compounds with a molecular weight >500 g/mol do not readily soak into most crystals. Additionally, in a protein crystal, the protein concentration is on the order of ~20-100 mM, so at best there would be a 2-10× lower concentration of the chromophore relative to the protein, which would lead to a low number of reducing equivalents generated with respect to protein concentration. Alternatively, $Ru(bpy)_3^{2+}$

could be co-crystallized with the protein, but the probability of identifying the right crystallization conditionsis likely quite low, and could be further limited by the relatively low solubility of Ru(bpy)$_3^{2+}$.The most likely outcome in most cases would be the generation of protein crystals from which the Ru(bpy)$_3^{2+}$ would be excluded and remain in solution. While these difficulties do not prohibit using Ru(bpy)$_3^{2+}$ as the means by which to photo-reduce a protein in a crystal, they led us to consider using another strategy to accomplish the desired objective.

$$NO_2^- + 8H^+ + 6e^- \longrightarrow NH_4^+ + 2H_2O$$
$$NO^\bullet + 6H^+ + 5e^- \longrightarrow NH_4^+ + H_2O$$
$$NH_2OH + 3H^+ + 2e^- \longrightarrow NH_4^+ + H_2O$$
$$SO_3^{2-} + 7H^+ + 6e^- \longrightarrow HS^- + 3H_2O$$
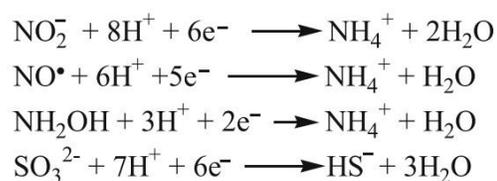
Scheme 4.1. Reactions catalyzed by ccNiR. It has also been shown that HAO can catalyze the reduction of nitrite and hydroxylamine (*10*)
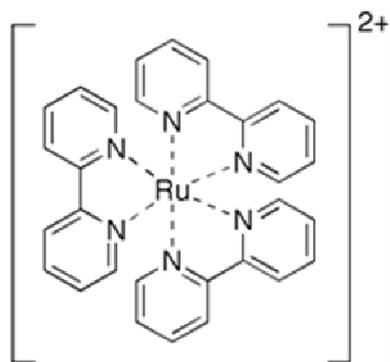
Figure 4.1. Structure of tris(bipyridine)ruthenium(II).

This led to us adapting a previously described system that provides for a highly efficient means by which to covalently attach a photo-active Ru(II) moiety to a protein crystal (*11*). Covalently attaching the chromophore to the protein prior to crystallizing the labeled construct has both advantages and disadvantages. With the chromophore directly attached to the protein, the challenge of having to soak the chromophore into the crystal, or co-crystallize chromophore and protein, is circumvented. Instead one needs only to find the right crystallization conditions for the chromophore-labeled protein. The major disadvantage to covalently attaching a chromophore to a protein and then crystallizing the labeled constructis that previously determined crystallization conditions will not be likely to translate to the new system. This is because the relatively large chromophore being attached to the surface of the protein will significantly change the protein's local charge and structure, and thus lead to significant changes in the preferred crystal packing arrangement. Therefore, one must assume that new crystallization conditions will have to be determined for Ru-labeled proteins. This, however, is well worth the effort, since a protein crystal with a protein:chromophore ratio of 1:1 would be obtained, which in turn would allow for highly controllable reduction of the labeled protein.

4.2. Materials and Methods

4.2.1. Generation of the ccNiR-T309C mutant. PCR was performed using

Phusion® hot-start high-fidelity DNA polymerase (Finnzymes) and the primers

ccNiRT309C-F (ATCAAATGGGTTACCAACCTTATGATCGGTAAACTTTTTGCC)

and ccNiRT309C-R (CGTTTTGAAGAGACCTGTGCTTGCTGCCATTCGCAAACC),

purchased with phosphorylated 5' ends from Integrated DNA Technologies.The template

DNA for this reaction was a minimal amount of the plasmid pHSG298 containing the

ccNiR optimized gene (See Chapter 2). The linear PCR product was treated with T4

DNA ligase (New England Biolabs) to create a new circular plasmid. This new plasmid

was then used to transform *S. oneidensis* TSP-C cells as described in Chapter 2. The

growth of the successfully transformed cells and purification of ccNiR-T309C were also

as described in Chapter 2, except that 1 mM of dithiothreitol (DTT) was added to the

buffers during purification. Additionally, at the end of the last step of purification,

ccNiR-T309C was exchanged into buffer containing 1 mM tris(2-carboxyethyl)phosphine

(TCEP) instead of DTT.

4.2.2. Attachment of the RBP Tag to ccNiR-T309C. Initially, ccNiR-T309C was

labeled with the commercially available fluorescent probe 1,5-IAEDANS (Invitrogen)

using the protocol provided by the manufacturer (Invitrogen MP 00003, revised in 2006).

A stock solution of 1,5-IAEDANS was prepared in DMSO and then was added to a

solution of ccNiR-T309C so that DMSO comprised 10% of the resulting solution, and

there was a 10-fold excess of 1,5-IAEDANS with respect to [ccNiR-T309C]. For

example, if [ccNiR-T309C] is 200 μM in a pH 7 buffer, then a 20 mM stock solution of

1,5-IAEDANS in DMSO should be prepared, and the two solutions should be mixed at a

ratio of 10:1.1, respectively. The reaction mixture was incubated at 4°C overnight.

Excess fluorescent probe was then removed by running the sample over a 25 cm × 1 cm

column containing G-25 gel filtration resin (Sigma) equilibrated with Buffer A (20 mM

HEPES, 1 mM EDTA, pH = 7.0) supplemented with 150 mM NaCl. The fractions

containing protein were pooled and checked for fluorescence in a Fluorolog-3

spectrofluorometer (Horiba) with an excitation wavelength of 336 nm and emission λ_{max}

of 490 nm. Excess probe could also be removed from the reaction mixture by repeatedly

concentrating and then diluting the sample in Buffer A using 10K MWCO centrifugal

concentrators (Millipore), until no unbound probe was detected in the flow-through.

[Ru(bpy)$_2$phen-IA](PF$_6$)$_2$ (RBP) was synthesized according to the procedure of

Castellano et al (*12*). A solution of RBP and ccNiR-T309C analogous to that described

above for 1,5-IAEDANS and ccNiR-T309C was incubated 4°C overnight as described

above. Unlabeled ccNiR-T309C was separated from labeled ccNiR-T309C (ccNiR-RBP)

by first loading the sample onto a HiTrap^{TM} SP HP cation-exchange column (GE

Healthcare) equilibrated with Buffer A, to which unlabeled protein will not bind. After

the column was thoroughly washed with Buffer A, ccNiR-RBP was eluted with Buffer B

(Buffer A + 500 mM NaCl), and subsequently desalted via repeated cycles of

concentration using 10K MWCO centrifugal filters (Millipore), and dilution with Buffer

A. The ccNiR-RBP solution was then divided into 50µL aliquots and frozen at -80°C for

future use. Attachment of RBP to ccNiR-T309C was verified using fluorescence with a

λ_{ex}= 460 nm and λ_{em} = 602 nm, as well as MALDI-TOF mass spectrometry.

4.2.3. Instrumentation. Photo-reduction of wild-type ccNiR and ccNiR-RBP was

initiated using 10 ns, 455 nm laser pulses from an OPO tunable laser (Opotek Rainbow

Vis). An OLIS RSM-1000 spectrophotometer was used to monitor the absorbance changes induced in the reaction mixture by the laser pulse. The configuration of the laser and spectrophotometric equipment was as described in general terms elsewhere (*13, 14*), except that the laser pulse was transmitted via an optical fiber instead of by using mirrors. Reactions were monitored with the OLIS RSM-1000 in fixed wavelength mode.

4.2.4. Photo-reduction of wild-type ccNiR and ccNiR-RBP. Photo-reduction of wild-type ccNiR was performed using a solution comprised of 2 μM ccNiR, 100 μM Ru(bpy)$_3^{2+}$ (Sigma), 10 mM EDTA, 1 mM methyl viologen (MV^{2+}, Acros), varying amounts of sodium nitrite, and a minimal amount of sodium dithionite, held in 3.0mm × 3.0mm microfluorometer square cuvettes (Starna). All solutions were made up in an anaerobic glovebox (Braun) with [O$_2$] < 2 ppm. Photo-reduction of ccNiR-RBP was conducted in a manner similar to that of the wild-type ccNiR, except the solution was comprised of 5 μM ccNiR-RBP, 200 mM potassium ferrocyanide (Acros), 10 nM catalase (Sigma), 1 mM glucose (Fisher), and 2 U/mL glucose oxidase (MP Biomedicals). For these experiments the solutions were held in 1.5mm × 1.5mm fluorometer sub-micro cuvettes (Starna), and the laser pulse was focused as a spot of ~5mm diameter, which irradiated the entire cuvette window.

4.3. Results and Discussion

4.3.1. Making ccNiR-T309C and Attachment of RBP Tag to ccNiR-T309C. In order to covalently attach RBP to ccNiR, a mutation had to be made on the surface of the protein to provide a binding site for the RBP tag. The mutagenesis process, as described

in the Materials and Methods section, was performed by Ms. Natalia Stein of the Pacheco group. The RBP tag has an iodoacetimide moiety which is very reactive towards thiols (*12*); therefore, a mutation causing a cysteine to be expressed on the surface of ccNiR would give the RBP tag a location to bind to the protein (Figure 4.2). The most conservative amino acid residue to mutate to a cysteine would be either a serine or a threonine(*15*). The amino acid T309, whose location is shown in Figure 4.3, was chosen as a promising candidate for RBP attachment because it is on the protein surface, and only one amino acid removed from H311, the axial ligand for ccNiR's heme 5 (Chapter 3, Figure 3.1). The latter is important because intramolecular electron transfer from the Ru center to the heme pool will only occur at a significant rate if there is a reasonably short path connecting the Ru to at least one of the hemes.
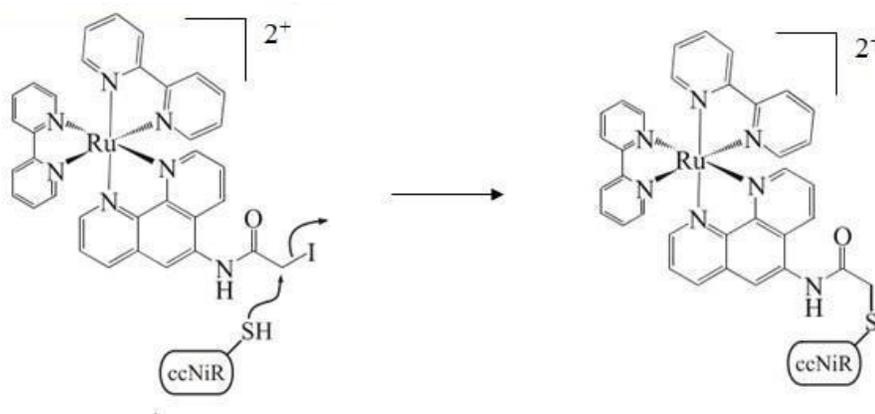
Figure 4.2. Schematic depiction of free RBP tag interacting with a cysteine that was mutated on the surface of ccNiR. The iodoacetimide reacts with the reduced thiol of the surface cysteine causing a covalent bond to form. Due to the fact that RBP is a di-cation, unlabeled ccNiR can subsequently be separated from ccNiR-RBP via cation-exchange chromatography.
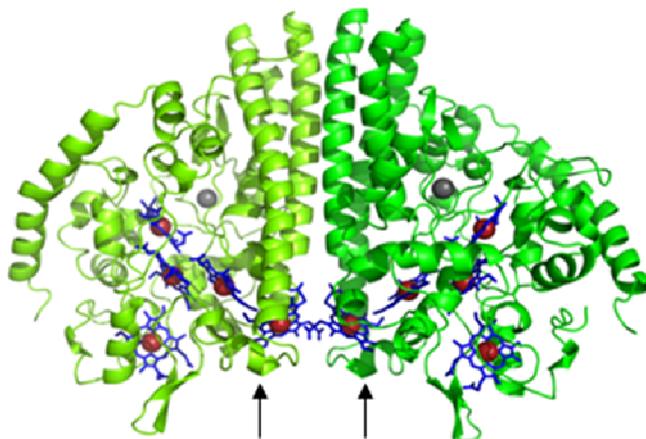
Figure 4.3. Location of T309 which was mutated to a cysteine for attachment of the RBP tag. T309 was chosen for as a target for RBP attachment due to its close proximity to an adjacent heme.

To ensure that a surface cysteine had been successfully inserted, the commercially-available fluorescent probe 1,5-IAEDANS was used. The attachment protocol provided by the manufacturerwarns that DTT is inhibitory to the attachment process, so at the last stage of the mutant's purification DTT was replaced with TCEP, which does not interfere with the attachment of the probe but will still keep the surface cysteine in a reduced state. After the recommended incubation time, and after excess probe was removed, fluorescence experiments showed that the probe had attached to the protein, indicating that a surface cysteine had been successfully introduced onto ccNiR.

For the attachment of RBP to ccNiR-T309C, the same procedure was used as with 1,5-IAEDANS.However, an additional purification step was necessary in order to separate ccNiR-T309C with no RBP attached from ccNiR-RBP. For this a cation-

exchange column was used, since RBP is a di-cation. The procedure is especially

efficientbecause unlabeled ccNiR does not bind to cation-exchange columns.

Fluorescence experiments verified that ccNiR-RBP had indeed been generated, yet the

MALDI-TOF data (Figure 4.4) suggest that only one RBP was attached per dimer. The

peak shift in Figure 4.4A indicates that one RBP tag has attached per dimer and the

broadening of the peak in Figure 4.4B indicates that there is a mixture of tagged and

untagged monomeric species. This is likely to be due to the close proximity of the C309

surface cysteines to the dimer interface; thus, when one RBP attaches it causes steric

hindrance, which prevents a second RBP from subsequently attaching.
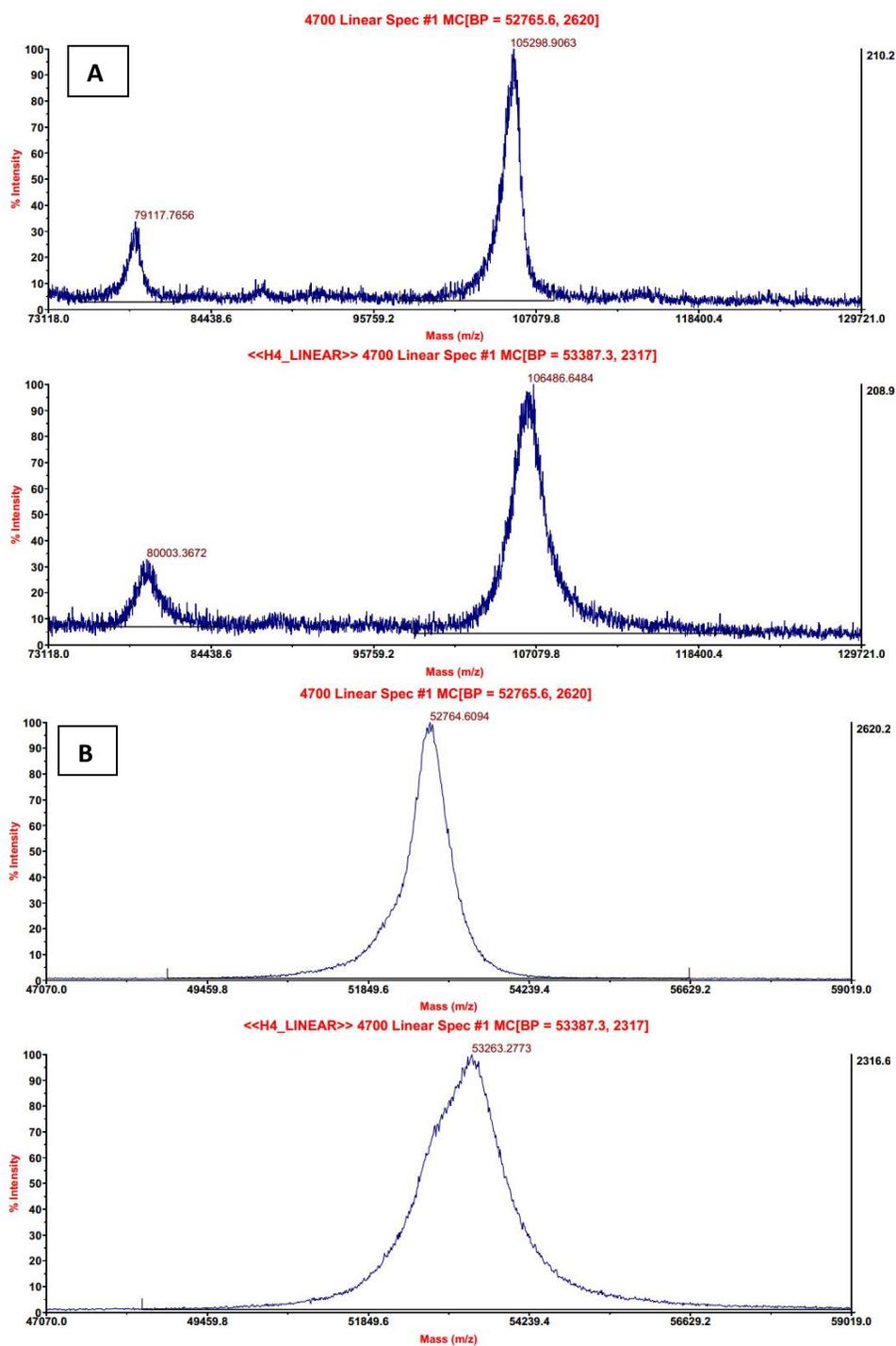
Figure 4.4. MALDI-TOF data showing wild-type ccNiR (top) versus ccNiR-RBP

(bottom) in each panel. **A**: MALDI-TOF data in the 100 kDa molecular weight range.

B: MALDI-TOF data in the 50 kDa molecular weight range.

4.3.2. Photo-reduction of wild-type ccNiR. Photo-reduction of wild-type ccNiR was performed using the well-studied system based on free $Ru(bpy)_3^{2+}$ that is depicted in Scheme 4.2 (*8*). Initially, a solution containing $Ru(bpy)_3^{2+}$ is illuminated with an intense laser pulse at a wavelength of 450 nm. This photo-excites $Ru(bpy)_3^{2+}$ to a state $^*Ru(bpy)_3^{2+}$ in which it is both a strong oxidant and a strong reductant. In the presence of a suitable electron acceptor, such as MV^{2+}, $^*Ru(bpy)_3^{2+}$ transfers an electron faster than it can relax to the ground state, generating MV^+ and the strong oxidant $Ru(bpy)_3^{3+}$. The latter species could oxidize MV^+ back to MV^{2+}, which would be non-productive quenching. Alternatively, if another species in solution is present that can react with $Ru(bpy)_3^{3+}$, such as EDTA, then $Ru(bpy)_3^{2+}$ can be regenerated. In the scenario where EDTA is used to accomplish this, EDTA is acting as a sacrificial electron donor since it fragments upon donating an electron to $Ru(bpy)_3^{3+}$, thus preventing the back reaction from occurring. Due to this fragmentation, a free-radical is generated which then reduces an additional equivalent of MV^{2+}. Therefore, the net reaction is such that for every one equivalent of $Ru(bpy)_3^{2+}$ that is photo-excited, two MV^+ reducing equivalents are generated(*8*). Note that the concentration of EDTA must be quite high (at least 1-10 mM) if it is to compete with MV^+ as the donor for $Ru(bpy)_3^{3+}$. Likewise, MV^{2+} must be in the mM range in order to capture a significant amount of $^*Ru(bpy)_3^{2+}$.

$$Ru(bipy)_3^{2+} \xrightleftharpoons{h\nu} {}^*Ru(bipy)_3^{2+}$$

$$^*Ru(bipy)_3^{2+} + MV_{ox} \longrightarrow Ru(bipy)_3^{3+} + MV_{red}$$

$$Ru(bipy)_3^{3+} + MV_{red} \longrightarrow Ru(bipy)_3^{2+} + MV_{ox} \quad \text{(non-productive quenching)}$$

$$Ru(bipy)_3^{3+} + edta \longrightarrow Ru(bipy)_3^{2+} + "R\bullet" + CO_2$$

$$"R\bullet" + MV_{ox} \longrightarrow "R^{+}" + MV_{red}$$

$$2MV_{ox} + edta \longrightarrow 2MV_{red} + "R^{+}" + CO_2 \quad \text{net reaction}$$
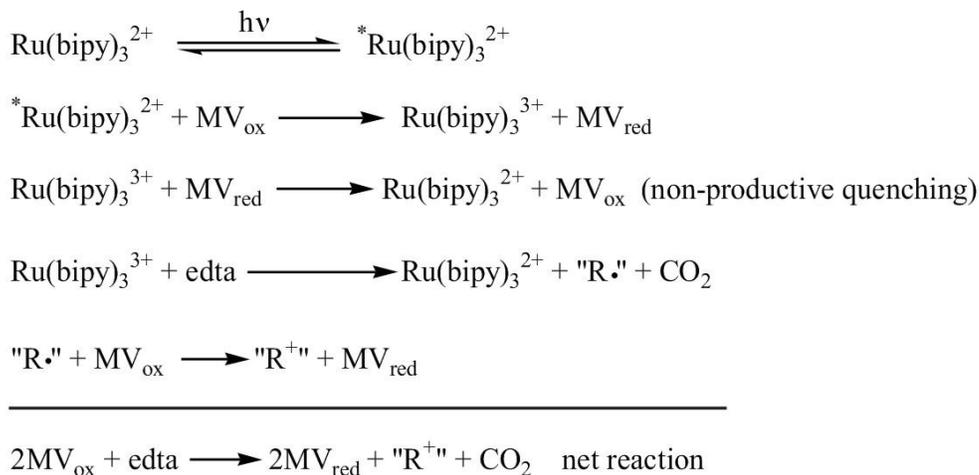
Scheme 4.2. Photo-reduction of methyl viologen (MV) in solution using $Ru(bpy)^{2+}$. Initially, $Ru(bpy)^{2+}$ is photo-excited using an intense laser pulse at 450 nm which generates an excited state. This excited species can then react with oxidized methyl viologen (MV_{ox}, equivalent to MV^{2+}) and reduced it to MV_{red} (equivalent to MV^+). At this point oxidized $Ru(bpy)^{3+}$ can react with MV_{red}, resulting in non-productive quenching since no net MV reduction has occurred. However, if an electron donor such as EDTA is present, then that donor can react with $Ru(bpy)^{3+}$, reducing it back to $Ru(bpy)^{2+}$. In this case, EDTA is a sacrificial electron donor, undergoing fragmentation which prevents the back reaction from occurring. Additionally, when EDTA fragments in this system, a free-radical is produced which can then also react with MV_{ox}. Therefore, in the net reaction, for every $Ru(bpy)^{2+}$ that is photo-excited, two reducing equivalents are produced.

The MV^+ generated in the reaction shown in Scheme 4.2 can subsequently reduce wild-type ccNiR in ~1 ms (Figure 4.5). The amount of MV^+ generated can be varied by varying the amount of $Ru(bpy)_3^{2+}$ initially present in solution, and this in turn changes the extent of eventual ccNiR reduction. The maximum $[MV^+]$ that was achieved using the procedure described in Section 4.2.3 was ~15 µM, which in the presence of mM concentrations of MV^{2+} allowed full reduction of the first three ccNiR heme centers, and partial reduction of the two lowest potential hemes (see Chapter 5). For the two traces shown in Figure 4.5, roughly two out of five hemes in each ccNiR monomer were reduced. The conditions for the two examples were essentially identical, except that the red trace in Figure 4.5 was collected in the presence of ~600 µM nitrite, while the blue trace was collected in the absence of nitrite. In each case the absorbance at 424nm initially rises rapidly as MV^+ reduces the hemes. In the presence of nitrite, this increase is followed by a fairly rapid decrease in absorbance, the rate of which depends on nitrite concentration. This phase is due to electron transfer from the reduced hemes to the coordinated nitrite, and is the one of interest to our research. Some re-oxidation is also seen in the blue trace obtained in the absence of nitrite, but this is substantially slower, varies from sample to sample, and is attributed to the reaction of the reduced hemes with residual oxygen.
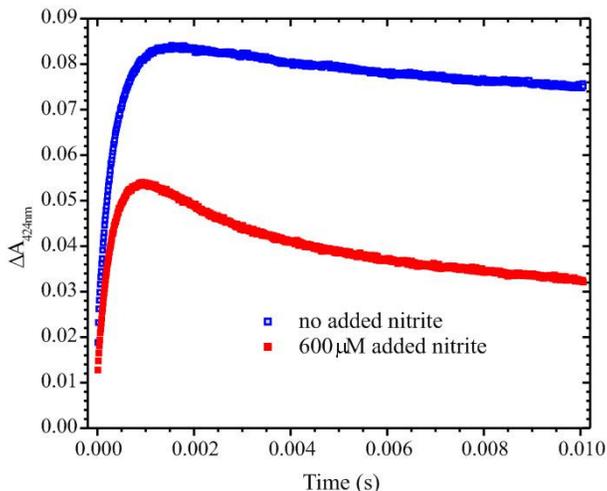
Figure 4.5. Time-trace of the reduced-heme peak. Photo-reduction of wild-type ccNiR using Ru(bpy)$^{2+}$/EDTA/MV occurs within 1 ms in the absence of substrate (blue). The decrease in amplitude beyond 1 ms can be attributed to trace oxygen. When the reaction is performed in the presence of substrate (red), significant changes have occurred in the dead-time of the instrument as well as on the longer millisecond time-scale.

Using the Scheme 4.2 methodology one could show that ccNiR must be reduced by two or more hemes per monomer in order to transfer electrons to nitrite; the one-electron reduced species did not reduce nitrite. It was also possible to obtain a qualitative picture of nitrite reduction rate dependence on nitrite concentration; however, quantitative analysis of data obtained using the Scheme 4.2 methodology proved complicated for two reasons. First, when using this methodology the enzyme is reduced by MV$^+$ in a second-order process that takes from several hundred microseconds to several hundred milliseconds, and generally overlaps the subsequentelectron transfer from the heme pool to NO$_2^-$ that is of interest. Second, the Scheme 4.2 process

invariably generates distributions of ccNiR molecules at various stages of reduction. These considerations, coupled to our concern that the Scheme 4.2 methodology would not translate well to time resolved crystallography (see Section 4.1), led us to abandon the strategy in favor of using the ccNiR-RBP construct, as is described in the next section.

4.3.3. Photo-reduction of ccNiR-RBP. The general strategy for photo-initiating heme reduction in the ccNiR-RBP construct is outlined in Scheme 4.3. Here the photo-excited RBP chromophore transfers an electron directly to the enzyme instead of indirectly through a mediator as in Section 4.3.2. The oxidized RBP is once again a powerful oxidant, and this strong oxidant is covalently linked to the now-reduced enzyme, so that the back-reaction is kinetically faster than it is when the ruthenium chromophore is free in solution. To effectively compete with the back-reaction an external sacrificial electron donor capable of reducing the ruthenium chromophore very rapidly is needed. Initial success was achieved using a large concentration of potassium ferrocyanide to reduce the RBP tag to its original resting state (Scheme 4.3). Figure 4.6 shows the spectral changes observed at 424nm after irradiating a solution initially containing 2.3 μM ccNiR-RBP and 150 mM ferrocyanide with a laser pulse. In Figure 4.6 the first two reactions from Scheme 4.3 take place within the dead-time of the instrument, so at t=0 ΔA_{424} has deflected in the positive direction from zero due to heme reduction. Over the next 4 ms though ΔA_{424} returns exponentially to the baseline, because the ferricyanide generated when quenching the ruthenium chromophore is itself a relatively strong oxidant, and re-oxidizes the protein with a half-life of ~700 μs.

$$Ru^{II}{}_{T309C}\text{-ccNiR} \xrightleftharpoons{h\nu} Ru^{III}{}_{T309C}\text{-ccNiR}^{-}$$

$$Ru^{III}{}_{T309C}\text{-ccNiR}^{-} + Fe(CN)_6{}^{4-} \longrightarrow Ru^{II}{}_{T309C}\text{-ccNiR}^{-} + Fe(CN)_6{}^{3-}$$

$$Ru^{II}{}_{T309C}\text{-ccNiR}^{-} + Fe(CN)_6{}^{3-} \longrightarrow Ru^{II}{}_{T309C}\text{-ccNiR} + Fe(CN)_6{}^{4-}$$
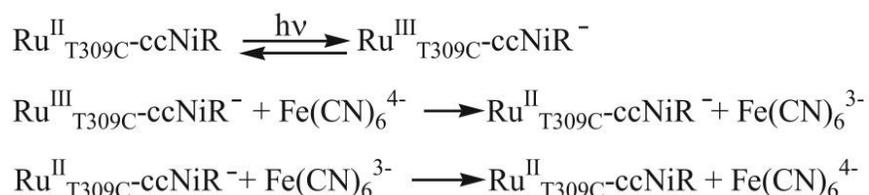
Scheme 4.3. Photo-reduction of ccNiR-RBP. An electron can be transferred from the ruthenium tag to ccNiR using an intense laser pulse with a wavelength of 455 nm. This generates oxidized ruthenium tag which in the absence of an electron donor would re-oxidize the enzyme. However, in the presence of ferrocyanide, the ruthenium tag can be quickly reduced back to its initial state. This process generates ferricyanide which on longer time-scales can re-oxidize ccNiR.

The preliminary experiment shown in Figure 4.6 demonstrated that the attached RBP chromophore is capable of rapidly and efficiently reducing the ccNiR heme pool. Based on the maximum amplitude of the trace in Figure 4.6 one can estimate that about 1.2 µM of heme was initially reduced by photo-initiated electron transfer, which represents a respectable ~50% of the maximal 2.28 µM attainable. Beyond the initial proof of concept experiments however, ferrocyanide will not be a suitable quencher of the Ru(III) state because of the subsequent back-reaction of reduced ccNiR with ferricyanide. For our purposes it will ultimately be necessary for the reduced protein to survive at least a few hundred milliseconds, ideally requiring an irreversible sacrificial donor such as EDTA (see Scheme 4.2). EDTA was tried as a quencher for ccNiR-RBP even before ferrocyanide, but it does not react with the Ru(III) photoproduct rapidly enough to compete with intramolecular electron transfer from the heme pool back to the

Ru(III) center. In very recent work in our laboratory, Natalia Stein has demonstrated that

diethyldithiocarbamate will irreversibly reduce the Ru(III) center of ccNiR-RBP, thus

opening the door for exploiting the methodology to its full extent.
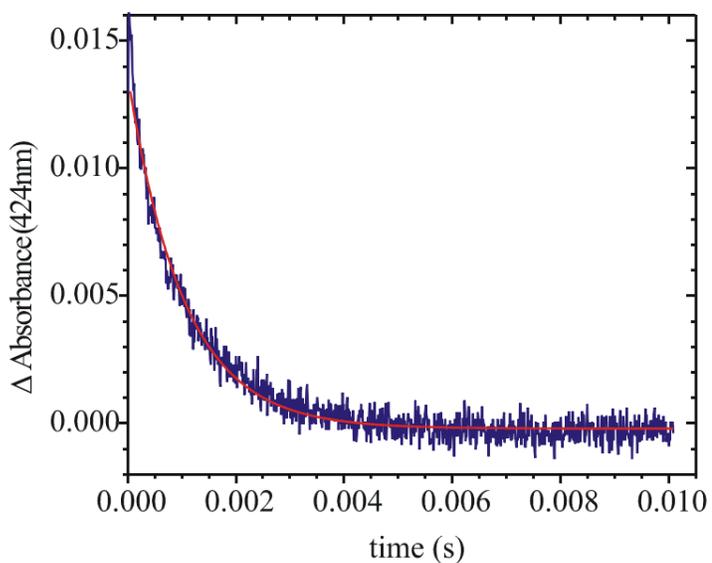
Figure 4.6. Time-trace of the reduced-heme peak of ccNiR-RBP. In the dead-time of

the instrument, an electron is transferred from the ruthenium tag to ccNiR, generating

reduced heme, and ferrocyanide reacts with the oxidized ruthenium tag to return it to its

initial state. Beyond this point, the ferricyanide generated in the previous reaction goes

on to react with the reduced ccNiR and re-oxidizes the enzyme with a half-life of ~700

μs.

4.4. Summary

For the study of the kinetic mechanism of ccNiR using time-resolved crystallography, a photo-initiation method is needed. Since the reactions that we are most interested in studying are reductive reactions, a photo-reduction process was used. Using $Ru(bpy)_3^{2+}$ in conjunction with a secondary electron donor proved to work well in solution, but this most likely would not work well in a crystal. For the photo-reduction of ccNiR in a crystal, we adapted a method of covalently attaching the ruthenium chromophore to the protein via an iodoacetimide linker on the chromophore, which covalently attached to a surface cysteine residue that was induced via a point mutation in ccNiR. This approach proved to be successful in photo-reducing the labeled ccNiR, but for only a short time, with a half-life for the reduction of the protein being ~700 μs. In order for this process to be useful for a time-resolved crystallography experiment, an alternative secondary electron donor, such as diethyldithiocarbamate, must be used that will allow for ccNiR to remain reduced over longer timescales.

4.5. References

1.   Pelliccioli, A. P., and Wirz, J. (2002) Photoremovable protecting groups: reaction mechanisms and applications, *Photochemical & Photobiological Sciences1*, 441-458.

2.   Shi, L., Chen, B., Wang, Z., Elias, D. A., Mayer, M. U., Gorby, Y. A., Ni, S., Lower, B. H., Kennedy, D. W., Wunschel, D. S., Mottaz, H. M., Marshall, M. J., Hill, E. A., Beliaev, A. S., Zachara, J. M., Fredrickson, J. K., and Squier, T. C.

(2006) Isolation of a high-affinity functional protein complex between OmcA and MtrC: two outer membrane decaheme c-type cytochromes of Shewanella oneidensis MR-1., *J. Bacteriol.188*, 4705–4714.

3. Wilker, J. J., Dmochowski, I. J., Dawson, J. H., Winkler, J. R., and Gray, H. B. (1999) Substrates for Rapid Delivery of Electrons and Holes to Buried Active Sites in Proteins, *Angewandte Chemie International Edition38*, 89-92.

4. Eroy-Reveles, A., Leung, Y., Beavers, C. M., Olmstead, M. M., and Mascharak, P. K. (2008) Near-Infrared Light Activated Release of Nitric Oxide from Designed Photoactive Manganese Nitrosyls: Strategy, Design, and Potential as NO Donors, *J. Am. Chem. Soc.130*, 4447-4458.

5. Stoddard, B. L., Cohen, B. E., Brubaker, M., Mesecar, A. D., and Koshland Jr., D. E. (1998) Millisecond Laue structures of an enzyme−product complex using photocaged substrate analogs, *Nature Structural and Molecular Biology5*, 891-897.

6. Schotte, F., Cho, H. S., Kaila, V. R. I., Kamikubo, H., Dashdorj, N., Henry, E. R., Graber, T. J., Henning, R., Wulff, M., Hummer, G., Kataoka, M., and Anfinrud, P. A. (2012) Watching a signaling protein function in real time via 100-ps time-resolved Laue crystallography, *PNAS109*, 19256-19261.

7. Tsuduki, T., Tomita, A., Koshihara, S., Adachi, S., and Yamato, T. (2012) Ligand migration in myoglobin: A combined study of computer simulation and x-ray crystallography, *Journal of Chemical Physics 136*, 165101-165110.

8.   Prasad, D. R., and Hoffman, M. Z. (1986) Photodynamics of the tris(2,2'-bipyrazine)ruthenium(2+)/methylviologen/EDTA system in aqueous solution, *Journal of the American Chemical Society108*, 2568-2573.

9.   Hoffman, M. Z. (1988) Cage escape yields from the quenching of excited tris(bipyridyl)ruthenium(2+) by methylviologen in aqueous solution, *Journal of Physical Chemistry92*, 3458-3464.

10.   Kostera, J., McGarry, J. M., and Pacheco, A. A. (2010) Enzymatic Interconversion of Ammonia and Nitrite: the Right Tool for the Job, *Biochemistry49*, 8546-8553.

11.   Terpetschnig, E., Dattelbaum, J. D., Szmacinski, H., and Lakowicz, J. R. (1997) Synthesis and Spectral Characterization of a Thiol-Reactive Long-Lifetime Ru(II) Complex, *Analytical Biochemistry251*, 241-245.

12.   Castellano, F. N., Dattelbaum, J. D., and Lakowicz, J. R. (1998) Long-Lifetime Ru(II) Complexes as Labeling Reagents for Sulfhydryl Groups, *Analytical Biochemistry255*, 165-170.

13.   Cabail, M. Z., Lace, P. J., Uselding, J., and Pacheco, A. A. (2002) Kinetic studies of the photoinitiated NO-releasing reactions of N,N '-bis-(carboxymethyl)-N,N '-dinitroso-1,4-phenylenediamine, *J. Photoch. Photobio. A.152*, 109-121.

14.   Cabail, M. Z., Moua, V., Bae, E., Meyer, A., and Pacheco, A. A. (2007) Quantifying the photoinduced release of nitric oxide from N,N'-bis(carboxymethyl)-N,N'-dinitroso-1,4-phenylenediamine. Effect of reducing agents on the mechanism of the photoinduced reactions, *J. Phys. Chem. A111*, 1207-1213.

15.   Betts, M. J., and Russell, R. B. (2003) Amino Acid Properties and Consequences

of Substitutions, In *Bioinformatics for Geneticists* (Barnes, M. R., and Gray, I. C.,

Eds.), pp 289-316, John Wiley & Sons, Ltd.

Chapter 5

Spectropotentiometry of ccNiR

5.1. Introduction

Given that ccNiR has multiple redox-active hemes, and that it catalyzes multi-electron reduction reactions, the extent of protein reduction is a critical parameter that must be tracked in any mechanistic study. This applies both to steady-state studies and to single turnover experiments such as time-resolved crystallography. Fortunately, heme-containing proteins, such as ccNiR and HAO, undergo changes in their UV/vis spectra upon reduction. If one can establish the correlation between a given spectral change and the extent of protein reduction, the information can subsequently be used to interpret time-resolved experiments. One technique that lends itself well to this task is spectropotentiometry, which is a combination of potentiometric titration and UV/Vis spectroscopy (*1, 2*). By using a spectral cell fitted with electrodes that are connected to a potentiometer, a series of UV/Vis spectra can be obtained at various applied potentials. In the case of ccNiR, there are five hemes that act as independent chromophores yet have similar overlapping UV/Vis spectra. Therefore, determining the extent of reduction is not a straightforward task. Nevertheless, by using sophisticated techniques such as singular value decomposition (SVD), unique spectral changes due to the various reduction events can be deconvoluted from each other. One can subsequently use this information to determine the extent of reduction in an experiment in which it would be impossible to monitor the solution potential directly, such as in time resolved experiments. This chapter describes a spectropotentiometric analysis of ccNiR at pH 7. While the standard

spectra are collected when the protein is in solution, the spectrum of a protein crystal could also be readily determined using a micro-spectrophotometer aligned to the portion of the crystal that is being photo-reduced. The data from the micro-spectrophotometer could then be compared to the solution standard spectra in order to calculate the extent to which the protein was reduced. Thus, the results presented in this chapter will be useful for interpreting future time-resolved experiments, both in solution and in the solid state.

5.2. Materials and Methods

UV/Vis spectropotentiometry experiments were performed using a BASi Epsilon EC potentiostat to set the potential, and a CARY Bio 50 UV/Vis spectrophotometer to obtain the spectra at each applied potential. The complete apparatus was housed in an anaerobic glove box. Controlled potentiometric electrolysis of the solution was performed in an optically transparent thin-layer electrode (OTTLE) cell, which was a modification of a previously reported design (*1, 2*), and is described in detail elsewhere (*3*). A solution of ccNiR and mediators (Table 5.1) was prepared in a buffer containing 50 mM HEPES, 200 mM NaCl, pH 7.0. All mediators were used at concentrations of 25 μM, except hexaammineruthenium(III) chloride, which had a concentration of 100 μM. UV/Vis spectra in the range from 250 to 800 nm were collected at 10-mV intervals between +50 and -600 mV (vs. SHE). An Ag/AgCl electrode (BASi, model RE-5B) was used as a reference. Cyclic voltammograms of MV were collected before and after collecting the data sets, and the calculated midpoint potentials were used to account for any drift in the reference electrode (the midpoint potential of MV was taken to be -0.449

V vs. SHE (*4*)). Data sets were also collected with identical mediator solutions in the absence of ccNiR, and these were subtracted from the corresponding ccNiR data sets to account for any spectral changes from the mediators during the titration. The corrected data sets were analyzed using the commercially available software packages Origin version 6.0 (Microcal Software) and Mathcad 13 (Mathsoft Engineering and Education).

Mediator	ε° (V vs. SHE)
Hexaammineruthenium(III) chloride	−0.020
Indigo carmine	−0.125
Anthraquinone 1,5-disulfonic acid	−0.175
Anthraquinone 2-sulfonic acid	−0.255
Safranine O	−0.289
6,7-DPD[a]	−0.390
Methyl viologen	−0.449

SHE standard hydrogen electrode

[a] 6,7-DPD:
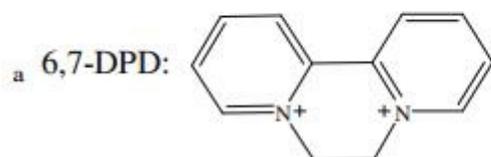
Table 5.1. Mediators used for spectropotentiometry.

5.3. Results

For spectropotentiometric analysis, the spectrum collected in the absence of an applied potential (that of the fully oxidized protein) was first subtracted from the spectra collected under applied potentials in order to generate difference spectra. The absorbance difference data collected between 379 and 454 nm, for all potentials between +34 and -516 mV versus the SHE, were then subjected to a global analysis described in detail in Appendix 3. Briefly, the data were first subjected to singular value decomposition (SVD) (5, 6), which revealed five components above the noise level. The SVD-processed data were next analyzed using a model in which each SVD component is assumed to correlate with the addition of one electron to each ccNiR protomer (Scheme 5.1, Eqs. 5.1a -5.1c and 5.2):

$$C_n = \frac{C_T \prod_1^n E_n}{\text{denom}},$$ (5.1a)

where

$$\text{denom} = 1 + E_1\{1 + E_2[1 + E_3[1 + E_4(1 + E_5)]]\},$$ (5.1b)

$$E_n = \exp\left[\frac{nF}{RT}(\varepsilon_n^0 - \varepsilon_{\text{app}})\right].$$ (5.1c)

$$\Delta\boldsymbol{\epsilon} = \Delta\mathbf{A} \cdot [\mathbf{C}_{\text{red}}(\mathbf{C}_{\text{red}}^{\mathbf{T}} \mathbf{C}_{\text{red}})^{-1}] \cdot \frac{1}{l}.$$ (5.2)

Equations 5.1a, 5.1b, and 5.1c are derived from the Nernst equation in exponential form, and correlate C_n with the applied potential (see Appendix 3). In these equations ε_n^0 is the midpoint potential associated with one-electron reduction of the $(n-1)^{th}$ reduced species, ε_{app} is the applied potential, and C_T is the total ccNiR concentration in solution. Equation 5.2 is a matrix version of Beer's law such that $\mathbf{C}_{\text{red}}$ is a matrix of concentrations in which each column corresponds to a unique reduced species and each row corresponds to a

specific applied potential, $\boldsymbol{\Delta\varepsilon}$ is an extinction coefficient difference matrix in which each column corresponds to a unique reduced species and each row corresponds to a wavelength, $\boldsymbol{\Delta A}$ is the SVD-processed absorbance difference matrix in which each column contains a spectrum at a fixed applied potential and each row shows how the absorbance varies with potential at a fixed wavelength, and l is a scalar representing the path length of the OTTLE cell. The data were fitted to Eqs. 5.1a – 5.1c, and 5.2 using a program created with Mathcad 13. This program first allows the user to manually enter trial values of the five midpoint potentials. For a given set of midpoint potential values, the program then uses Eqs. 5.1a – 5.1c to calculate the concentration of each reduced species at a given applied potential, and stores the concentrations in $\mathbf{C_{red}}$ (Eq. 5.2). Next, the program calculates the extinction coefficient spectra $\Delta\varepsilon$ using Eq. 5.2 (*7*). Finally, the program uses l and the $\boldsymbol{\Delta\varepsilon}$ and $\mathbf{C_{red}}$ matrices to generate an absorbance matrix $\boldsymbol{\Delta A_{calc}}$, and the sum of squares for $\boldsymbol{\Delta A}$-$\boldsymbol{\Delta A_{calc}}$ is computed. By varying the trial values of the five ccNiR midpoint potentials, one can minimize this sum of squares.

$$Ox + e^- \longrightarrow C_1$$
$$C_1 + e^- \longrightarrow C_2$$
$$C_2 + e^- \longrightarrow C_3$$
$$C_3 + e^- \longrightarrow C_4$$
$$C_4 + e^- \longrightarrow C_5$$
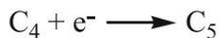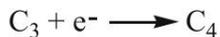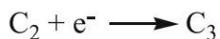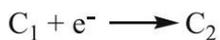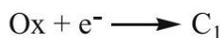
Scheme 5.1. Reduction of fully oxidized ccNiR (Ox). C_1–C_5 refer to the one-electron-reduced to five-electron-reduced species, respectively.

Figure 5.1 shows the results of the global analysis. Figure 5.1a compares the experimental and calculated spectra at selected applied potentials, and Figure 5.1b shows

the fitted ΔA versus ε_{app} slice at 426 nm. Figure 5.2a provides the calculated extinction coefficient difference spectra $\Delta\varepsilon_n$ (the columns of matrix $\mathbf{\Delta\varepsilon}$) for each of the reduced ccNiR species, and Figure 5.2b provides the absolute extinction coefficient spectra for the species, obtained by adding the extinction coefficient spectrum of the fully oxidized ccNiR to each of the extinction coefficient difference spectra. Finally, Figure 5.2c shows the calculated concentrations of the reduced species C_n as a function of the applied potential. Table 5.2 lists the five calculated midpoint potentials, comparing them with those obtained by direct voltammetric methods, and with those previously reported for *E. coli* ccNiR (*8-10*). The uncertainties quoted for each of the $\varepsilon°_n$ values represent the changes that could be made to each trial $\varepsilon°_n$ without increasing the sum of squares by 0.001 units or more (approximately 6% of the sum of squares value).

The procedure described above was also used to investigate the spectral region from 500 to 650 nm, where the characteristic α and β bands are observed for reduced low-spin hemes. The complete analysis is provided in Appendix 3.
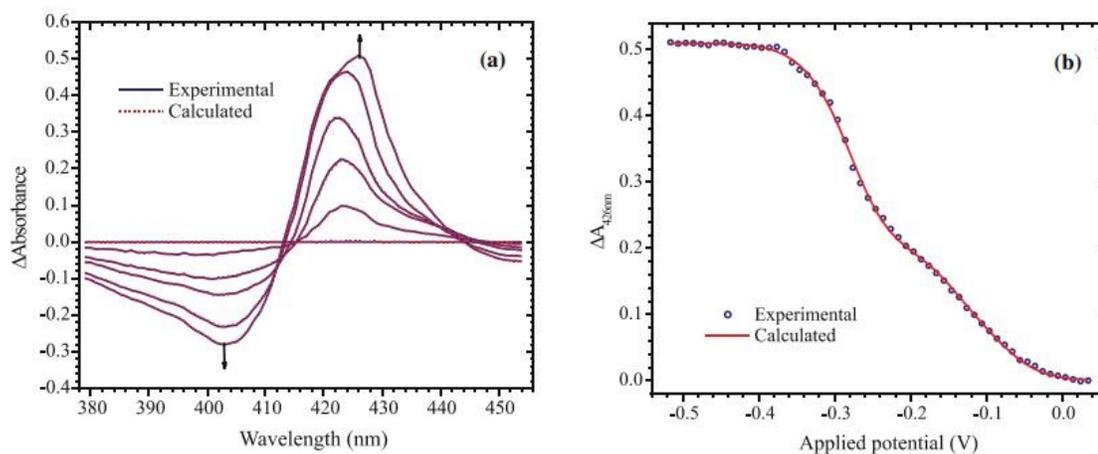
Figure 5.1. **A:** Spectra obtained at applied potentials of 0.034,-0.106, -0.196,-0.256,-0.316, and -0.506 V versus the standard hydrogen electrode (SHE). Solid blue lines show the experimentally obtained data, whereas the dashed red lines show the fit obtained using the matrix represented by Eq. 5.2. **B:** The least-squares best fit of the data by Eq. 5.2 at 426 nm.
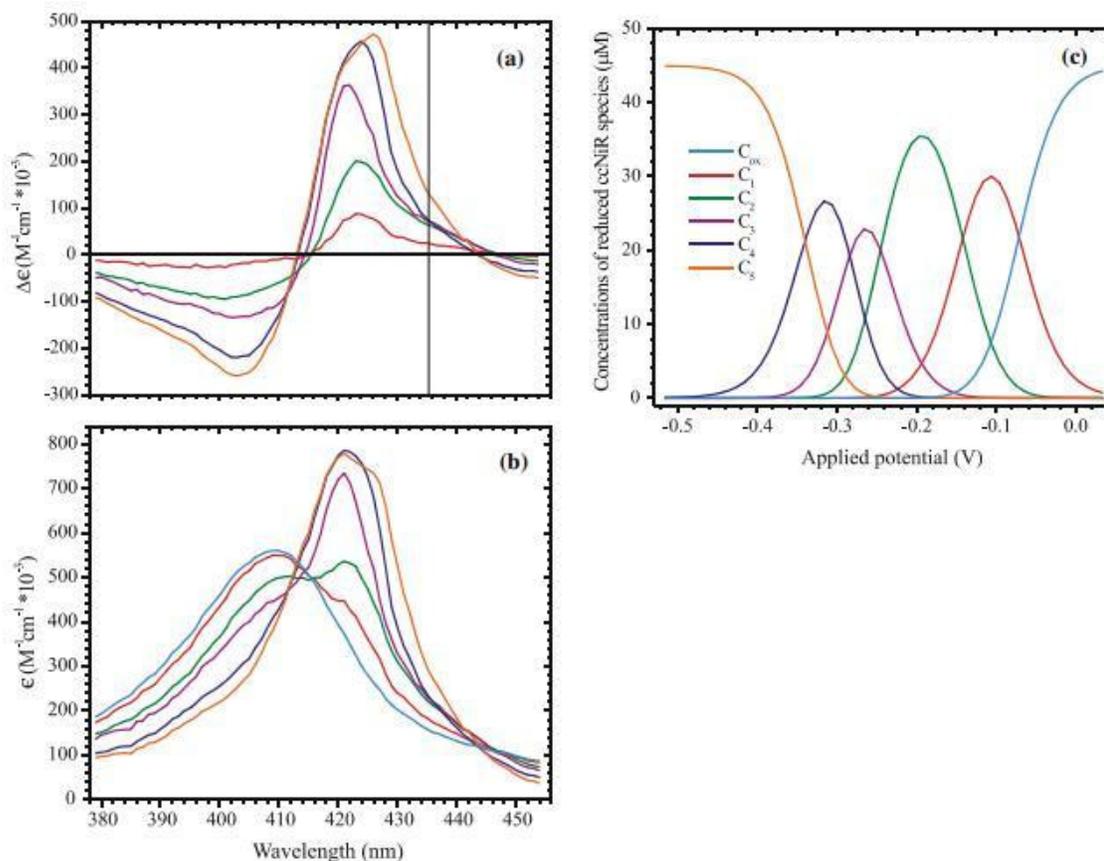
Figure 5.2. **A:** Extinction coefficient difference spectra corresponding to each of the reduced ccNiR species C_1–C_5 (Scheme 5.1), as calculated by fitting the experimental spectropotentiometric titration data using Eq. 5.2. The vertical line shows the point at which a high-spin ferroheme should have an absorbance maximum. **B:** Similar to **A**, but here the calculated absolute extinction coefficient spectra of C_1–C_5 and with the spectrum of C_{ox}, are shown. **C:** Concentrations of the various ccNiR species present in solution at a given applied potential (vs. SHE), obtained by fitting the data to Eq. 5.2.

5.4. Discussion

As shown in Figure 5.1, the spectropotentiometric data set is quite reasonably modeled by Scheme 5.1, which assumes five uncoupled reduction events. Attempts to fit the data set with models that incorporated coupled reductions invariably produced poorer fits. Table 5.2 summarizes the midpoint potentials of *S. oneidensis* ccNiR obtained by spectropotentiometry and film voltammetry, and compares these values with ones previously reported for ccNiR from *E. coli* (*8-10*). For the *S. oneidensis* protein, the midpoint potentials obtained by film voltammetry are consistently more positive than those obtained by spectropotentiometry, by anywhere from 30 to 80 mV. Attempts to fit the spectropotentiometric data set using the midpoint potentials obtained by film voltammetry yielded very poor fits. The voltammetric data were collected at pH 6, whereas the potentiometric data were obtained at pH 7, and this may partially explain the observed differences. However, we note that the various sets of midpoint potentials obtained for *E. coli* show similar inter-set variability (Table 5.2), even though all of those experiments were done at pH 7. Indeed, there is more variation between the midpoint potential values obtained from the three *E. coli* ccNiR data sets, or between the values obtained from the two *S. oneidensis* ccNiR data sets, than there is when comparing the *S. oneidensis* midpoint potentials obtained by film voltammetry with those obtained by magnetic circular dichroism spectropotentiometry for *E. coli* ccNiR (Table 5.2). We therefore conclude that the ccNiRs from *S. oneidensis* and *E. coli* probably have very similar heme midpoint potentials at both pH 6 and pH 7, and that the observed differences are primarily due to experimental biases introduced by the various measuring

methods. Given the complexity of the systems being investigated, these differences are comparatively minor.

S. oneidensis ccNiR		E. coli ccNiR		
Spectropotentiometry	Film voltammetry	MCD spectropotentiometry[a]	Film voltammetry[b]	EPR spectropotentiometry[c]
-0.062 ± 0.007	-0.036	-0.020 ± 0.015 (ls)	$+0.022 \pm 0.015$	-0.037 (ls)
-0.140 ± 0.005	-0.105	-0.108 ± 0.009 (active site)	-0.056 ± 0.015	-0.107 (active site)
-0.25 ± 0.01	-0.166	-0.153 ± 0.011 (ls)	-0.117 ± 0.015	-0.107 (ls)
-0.283 ± 0.007	-0.230	-0.206 ± 0.019 (ls)	-0.189 ± 0.015	-0.323 (ls)
-0.342 ± 0.004	-0.295	-0.292 ± 0.034 (ls)	-0.275 ± 0.015	-0.323 (ls)

Table 5.2. Midpoint potentials of ccNiR hemes (in volts vs. SHE) obtained in this work for the *S. oneidensis* protein and in previous investigations of ccNiR from *E. coli*. Film voltammetry experiments on the *S. oneidensis* ccNiR can be found in (*8*). *a* – Average of two experiments from (*10*), *b* – From (*10*), *c* – From (*9*). MCD – magnetic circular dichroism, ls – low spin.

We have found one surprising difference between the UV/vis spectral characteristics of *S. oneidensis* ccNiR and those reported for *E. coli* ccNiR. In the *E. coli* enzyme, reduction of the active-site heme was reported to produce a distinct signal at 435.5 nm (*10*), consistent with its EPR identification as a high-spin species (*9*). We see no such distinct signal in the *S. oneidensis* ccNiR UV/vis spectrum as the protein is reduced; the five reduced species all have calculated extinction coefficient spectra with maxima below 430 nm, where low-spin ferrous hemes are expected to absorb (Figure 5.2). The maximum of the final reduced species, C_5, does shift to significantly longer wavelength, but remains below 430 nm. Moreover, by analogy with *E. coli* ccNiR,

whose reduction potentials have been assigned to specific hemes primarily on the basis of EPR spectropotentiometry (*9*), we would expect that active-site heme 1 is the second heme reduced ($\varepsilon°_2 = -0.140$ V). The extinction coefficient difference spectrum of the second reduced species, C_2, has a maximum at 423 nm (Figure 5.2a). However, we do note what could be an important pattern at 435 nm in the calculated extinction coefficient difference spectra (vertical line in Figure 5.2a). Reduction of fully oxidized ccNiR to C_1 results in a small increase in $\Delta\varepsilon_{435}$, which is followed by a significantly larger increase as C_1 is reduced to C_2. Further reduction of C_2 first to C_3 and then to C_4 results in virtually no change in $\Delta\varepsilon_{435}$, after which there is another sizeable increase as C_4 is reduced to C_5. This final increase in $\Delta\varepsilon_{435}$ can be explained by the shift in λ_{max} as C_4 is reduced to C_5; however, the increase associated with the reduction of C_1 to C_2 arises from the fact that the C_2 extinction coefficient difference spectrum is broader than the other spectra, with an unusually long tail stretching to longer wavelengths.

All of our observations are more easily explained if we do not associate each ccNiR reduction step with reduction of a single individual heme. Instead we propose that, for example, in two-electron-reduced ccNiR (species C_2) the two electrons are delocalized among several of the hemes, and that the same may be true for the other stages of reduction. This would explain why the UV/Vis spectral changes associated with reduction of C_1 to C_2 appear to exhibit features characteristic of both low-spin and high-spin ferrohemes. This interpretation is also consistent with the EPR results reported by Bamford et al. (*9*). For example, these researchers showed that a signal at $g = 10.8$ observable in parallel mode decreased rapidly to about 20% of its initial intensity at applied potentials of approximately -0.05 to -0.2 V, but then decreased at a much slower

rate thereafter. This signal was assigned to the high-spin ferric active site weakly

exchange coupled to low-spin ferric heme 3. Our interpretation assigns the rapid

decrease in the $g = 10.8$ signal to production of the two-electron-reduced ccNiR (C_2), but

allows a fraction of the C_2 population to retain original ferric heme 1. In this fraction,

another heme would be reduced instead. The appearance of such a distribution of

reduced hemes within a multiheme complex has been predicted in a theoretical

investigation of HAO redox equilibria (*11*), and is likely to be a common phenomenon in

proteins with multiple redox-active sites.

It should also be noted that recent electrochemical studies have indicated that all

reductive events in the catalytic reduction of nitrite to ammonia by ccNiR are most likely

sequential one-electron reductive processes, as opposed to cooperative two-electron

reductive events, such as in the final step of catalysis where hydroxylamine is reduced by

two electrons to form ammonia (*12*). These recent results are by no means conclusive,

but the observations clearly lend themselves towards an avenue of further research.

5.5. Summary

For experiments involving redox-active proteins, such as ccNiR, the ability to

determine the extent of protein reduction in these experiments is crucial. In order to

accomplish this, spectropotentiometry was used to determine the relative extinction

coefficient spectra for each of the five one-electron reduced species that are possible in

ccNiR. The fitting of spectral data collected during a time-resolved experiment, whether

performed in solution or in a crystal, to the previously determined extinction coefficient

spectra for the different reduced ccNiR species, allows for the determination of the extent of reduction. Interestingly, our analysis of the spectropotentiometry data showed that electrons in a partially reduced ccNiR molecule are delocalized over multiple hemes, as opposed to being centered on a particular heme. This result illustrates that our global analysis approach to analyzing the spectropotentiometric data allows for an understanding of the ccNiR system that would not have been possible with a less comprehensive approach.

5.6. References

1.   Heineman, W. R., Norris, B. J., and Goelz, J. F. (1975) Measurement of enzyme $E^{0'}$ values by optically transparent thin layer electrochemical cells, *Anal. Chem. 47*, 79-84.

2.   Pilkington, M. B. G., Coles, B. A., and Compton, R. G. (1989) Construction of an optically transparent thin layer electrode cell for use with oxygen-sensitive species in aqueous and non-aqueous solvents, *Anal. Chem. 61*, 1787-1789.

3.   Bodemer, G. J. (2008) An investigation of OmcA from *Shewanella oneidensis MR1:* redox and structural characterization, In *Ph. D dissertation*, University of Wisconsin-Milwaukee, Milwaukee, WI.

4.   Watanabe, T., and Honda, K. (1982) Measurement of the extinction coefficient of the methyl viologen cation radical and the efficiency of its formation by semiconductor photocatalysis, *J. Phys. Chem. 86*, 2617-2619.

5.   Press, W. H., Teukolsky, S. A., Vetterling, W. T., and Flannery, B. P. (2007) Numerical Recipes the art of scientific computing, 3rd ed., pp 65-75, Cambridge University Press, New York, NY.

6.   Henry, E. R., and Hofrichter, J. (1992) Singular Value Decomposition: Application to Analysis of Experimental Data, In *Meth. Enzymol.* (Brand, L., and Johnson, M. L., Eds.), pp 129-192, Academic Press, San Diego.

7.   Press, W. H., Teukolsky, S. A., Vetterling, W. T., and Flannery, B. P. (2007) Numerical Recipes the art of scientific computing, 3rd ed., pp 773-839, Cambridge University Press, New York, NY.

8.   Youngblut, M., Judd, E. T., Srajer, V., Sayyed, B., Goelzer, T., Elliott, S. J., Schmidt, M., and Pacheco, A. A. (2012) Laue crystal structure of *Shewanella oneidensis* cytochrome *c* nitrite reductase from a high-yield expression system, *J. Biol. Inorg. Chem. 17*, 647-662.

9.   Bamford, V. A., Angove, H. C., Seward, H. E., Thomson, A. J., Cole, J. A., Butt, J. N., Hemmings, A. M., and Richardson, D. J. (2002) Structure and spectroscopy of the periplasmic cytochrome c nitrite reductase from Escherichia coli, *Biochemistry 41*, 2921-2931.

10.   Marritt, S. J., Kemp, G. L., Xiaoe, L., Durrant, J. R., Cheesman, M. R., and Butt, J. N. (2008) Spectroelectrochemical characterization of a pentaheme cytochrome in solution and as electrocatalytically active films on nanocrystalline metal-oxide electrodes, *J. Am. Chem. Soc. 130*, 8588-8589.

11. Kurnikov, I. V., Ratner, M. A., and Pacheco, A. A. (2005) Redox equilibria in hydroxylamine oxidoreductase. Electrostatic control of electron redistribution in multielectron oxidative processes, *Biochemistry 44*, 1856-1863.

12. Judd, E. T., Youngblut, M., Pacheco, A. A., and Elliott, S. J. (2012) Direct Electrochemistry of Shewanella oneidensis Cytochrome c Nitrite Reductase: Evidence of Interactions across the Dimeric Interface, *Biochemistry 51*, 10175-10185.

Chapter 6

Running *S. oneidensis* ccNiR in Reverse

6.1. Introduction

As shown in Figure 1.1 of Chapter 1, microorganisms can extract energy by interconverting nitrite and ammonia in either direction. Under aerobic conditions energy is extracted by ammonia-oxidizing bacteria (AOB) from the oxidation of ammonia by oxygen, whereas under anaerobic conditions the energy is obtained by nitrite ammonifiers from the reduction of nitrite by organic electron donors (*1, 2*). Given that the thermodynamics of ammonia-nitrite interconversion can be readily shifted to favor one direction while remaining within biologically accessible boundaries, the Pacheco research group is very interested in understanding how, and maybe even if, the enzymes that interconvert ammonia and nitrite are optimized to operate preferentially in one direction or the other. During ammonification the primary enzyme used is ccNiR, whereas the AOB use ammonia mono-oxygenase and hydroxylamine oxidoreductase (HAO) in conjunction to oxidize ammonia to nitrite. CcNiR and HAO are structurally similar, which makes the question of whether they have been evolutionarily optimized to catalyze similar reactions in opposite directions all the more intriguing. Previously, our group described how HAO can be run in reverse by applying a sufficiently negative electrochemical potential to the reaction mixture (*3, 4*). This chapter evaluates ccNiR's ability to run in reverse in the presence of high hydroxylamine concentrations.

6.2. Materials and Methods

    6.2.1. Stopped-Flow. Stopped-flow experiments were run on a SF-61 DX2 Double Mixing Stopped-Flow System (Hi-Tech Scientific) that was made anaerobic by scrubbing with glucose oxidase (MP Biomedicals) and glucose (Fisher Scientific) at concentrations of 2 U/mL and 1 mM, respectively. Enzyme samples were made anaerobic by alternately gently pumping on vacuum and purging with argon repeatedly. All other solutions were made anaerobic by purging with argon. All data were collected at 20°C.

    In order to prevent drastic pH changes when mixing ccNiR with high concentrations of hydroxylamine hydrochloride (Acros) during stopped-flow experiments, a double-mixing strategy was employed. Solutions of hydroxylamine hydrochloride were first rapidly mixed with HEPES sodium salt (Fisher Scientific) at a ratio of hydroxylamine:HEPES of 1:1.18, and aged for one second in order to obtain a final pH of 7.0. This buffered hydroxylamine solution was then rapidly mixed with a 2 μM ccNiR solution in 20 mM HEPES, 1 mM EDTA, pH 7.0. Spectral data were collected using a photo-diode array detector (Hi-Tech Scientific) on both short (1.5 second) and long (30 second) timescales, after which the datasets were combined and analyzed using programs written within the commercially available software packages Mathcad 13.0 (PTC Software) and Origin 6.0 (Microcal Software). The analysis strategies used in our laboratory have been previously described (*3-7*); details specific to this work are provided in the Results Section 6.3.

6.2.2. Rapid freeze-quench EPR. Rapid freeze-quench samples were made using a syringe-ram controller Model 715 (Update Instrument, Inc), and quenched in -95°C isopentane. Reaction mixtures consisted of a final concentration of 200 mM hydroxylamine, 236 mM HEPES sodium salt, and 50 µM ccNiR, pH 7.0. EPR spectra were recorded at the Medical College of Wisconsin with 100 kHz magnetic field modulation on a EleXsys E600 spectrometer (Bruker), equipped with an Oxford Instruments ITC503 temperature controller and ESR900 helium flow cryostat (Oxford Instruments). Perpendicular mode EPR spectra were recorded at 9.39 GHz using an ER 4122SHQ resonator, and at 9.63 GHz using an ER 4116DM resonator in TE102 mode. All parallel mode data were recorded at 9.39 GHz with the ER 4116DM operating in TE012 mode. Precise frequencies were recorded for each spectrum by a built-in microwave counter. Background signals were recorded on a frozen water sample and subtracted in Xepr (Bruker Biospin) with small field corrections for slight frequency differences. Spectra were collected at a temperature of 10 K and a microwave power of 5 kW. Other recording parameters were chosen such that the resolution was limited by the 10 G sinusoidal field modulation amplitude. It was noted that a copper contaminant was present in several samples, so a mixture of hydroxylamine and HEPES sodium salt, as prepared previously, was rapidly mixed with 1 mM $CuSO_4$ in 20 mM HEPES, pH 7.0, using the same freeze-quench technique as previously described. This sample generated an EPR spectrum that was suitable for subtracting the copper contaminant from the previously generated data. Finally, intensities were normalized to the signal at 2290 G.

6.2.3. Nitrite/Nitric Oxide/Ammonia Assays. Two well documented nitrite detection assays were used: the Griess assay (*8*), and the DAN assay (*9*). Samples were

prepared in an anaerobic glovebox with 200 mM hydroxylamine solution and varying

amounts of ccNiR. After 15 minutes, the ccNiR was removed using 10K MWCO

centrifugal concentrators (Millipore). In order to prevent hydroxylamine from interfering

with the assay, a 10% excess of sodium pyruvate was added to each reaction mixture,

after which the assay was performed. Data were collected using a Varioskan Flash

microtiter plate reader (Thermo Scientific).

Nitric oxide was assayed as described previously (5), by carrying out the same

reaction as described above in the presence of 5 µM catalase (Sigma). Catalase binds

nitric oxide tightly, leading to a characteristic change in the UV/Vis spectrum that is

readily quantified.

Ammonia was quantified using a well-documented enzymatic assay (5), that had

to be modified to first eliminate the interfering high ionic strength solution that

accompanied the high hydroxylamine concentrations. A reaction was performed as was

done in the nitrite detection assays. Once the enzyme was removed and the solution was

treated with pyruvate, the solution was run through a device used to selectively dialyze

the ammonia out of the high ionic strength solution into a low ionic strength solution that

was subsequently assayed for ammonia concentration. A complete description of the

device can be found in Appendix 4.

6.3. Results

    6.3.1. Stopped-Flow. Figure 6.1 shows selected spectral changes observed after mixing 0.80 µM ccNiR with 160 mM hydroxylamine using the double-mixing stopped-flow method described in Section 6.2.1. The changes are broadly characteristic of low-spin *c*-heme reduction, exhibiting a maximum positive absorbance deflection at ~422 nm, and a maximum negative amplitude at ~402 nm (*10, 11*). Nevertheless there are subtle shifts in the difference spectra over time (Figure 6.1a), and a look at the time domain (Figure 6.1b) reveals that spectral changes occur on three distinct timescales: a fast phase that is complete within ~100 ms, followed by slower phases evolving over ~1s and 30s, respectively. Singular value decomposition (SVD) analysis revealed four spectral components, so the SVD-processed spectra were fitted using a model that incorporated three exponentials and an initial (t_0) invariant spectrum. The least-squares calculated spectra at selected times after mixing are overlaid on the experimental traces in Figure 6.1a (red and yellow traces), while Figure 6.1b shows a fitted sample ΔA vs time trace at 422 nm. Figure 6.2a shows the extinction coefficient difference spectra calculated for each of the components in the Figure 6.1 fit, while Figure 6.2b shows how the concentration of each species is predicted to evolve over time.
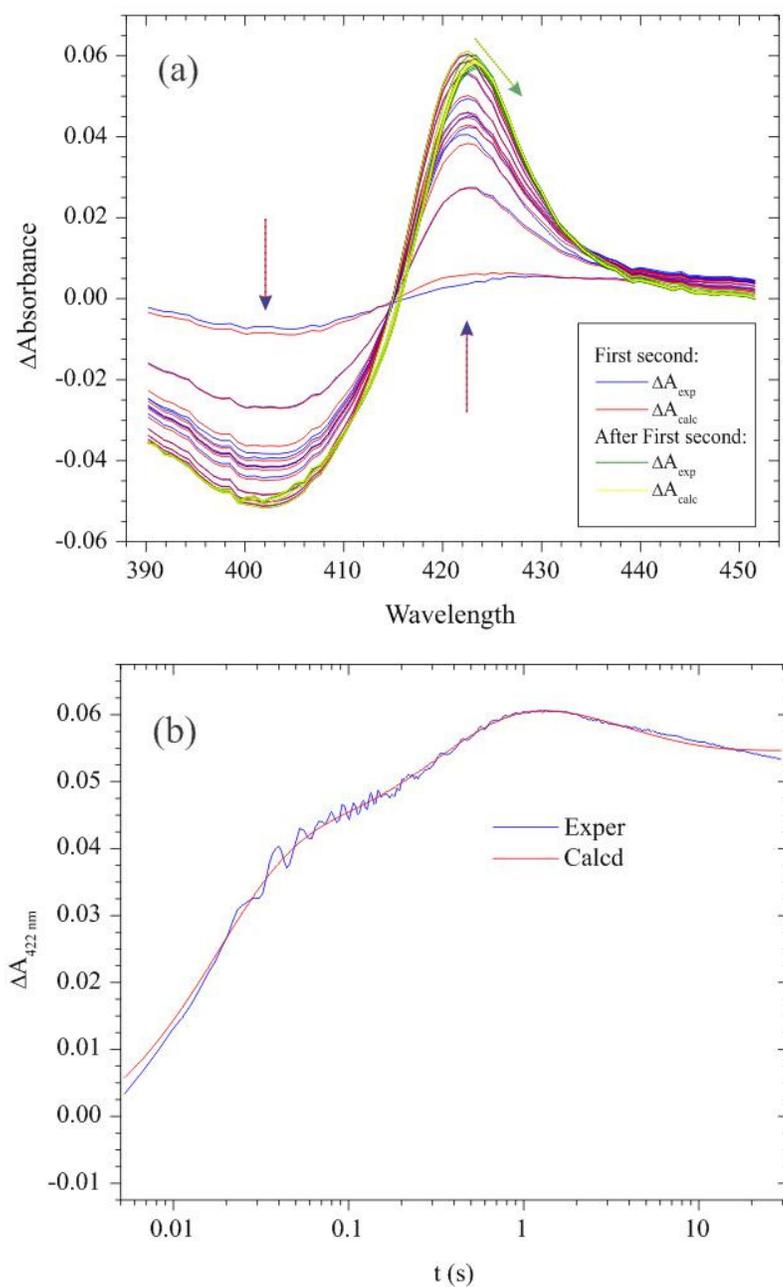
Figure 6.1. A: Results of the reaction of 160 mM hydroxylamine with 0.80 μM ccNiR$_{ox}$ showing both experimental data and calculated fits of the data. A decrease in signal at ~402 nm and an increase in signal at ~422 nm indicates heme reduction. **B:** Time-trace of the data at 422 nm and its associated fit.
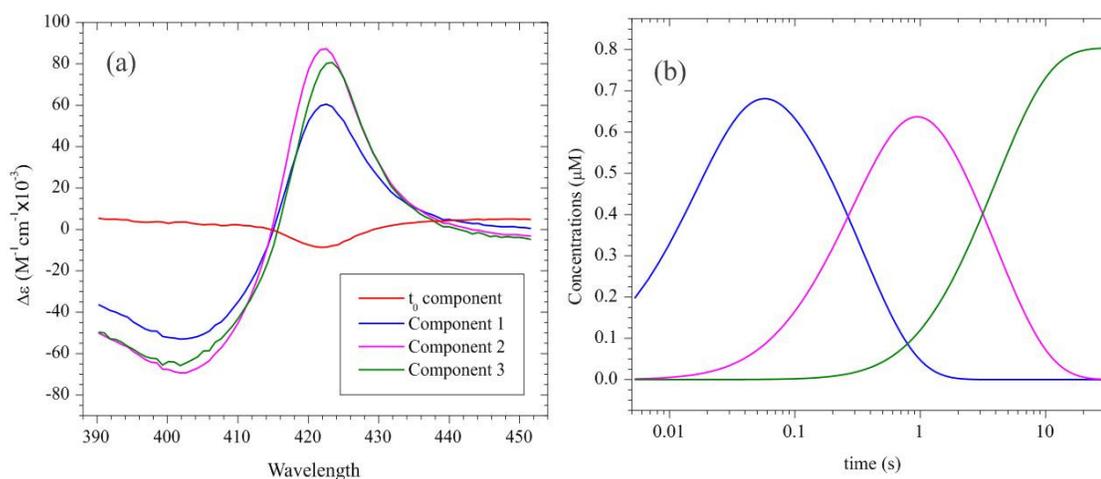
Figure 6.2. **A:** Plot of the extinction coefficient difference spectra of the spectral

component at t_0 and the three subsequent species that were sequentially generated in the

reaction of ccNiR$_{ox}$ and hydroxylamine. The λ_{max} of the reduced heme peak at 424 nm

increases in amplitude from the first intermediate to the second, and then slightly

decreases in amplitude from the second intermediate to the final species as well as a

slight red-shift. **B:** Simulation of the reaction of 1 μM ccNiR$_{ox}$ and 200 mM

hydroxylamine using the rate constants for the formation of the three subsequent species

as determined via UV/vis stopped-flow. The first intermediate species had a maximum

accumulation at ~100 ms, the second at ~1 s, and the final species had a maximum

accumulation at ~10 s. The simulation assumed that all reactions were irreversible.

When the experiment shown in Figures 6.1 and 6.2 was repeated using varying

concentrations of NH$_2$OH, the apparent rate constant for formation of the first component

was found to vary hyperbolically with [NH$_2$OH] (Figure 6.3a). The other two

components were essentially independent of [NH$_2$OH] (Figures 6.3b, c). These

observations were interpreted in terms of the chemical model shown in Scheme 6.1. In this model the fully oxidized ccNiR and added hydroxylamine first come to a rapid pre-equilibrium governed by equilibrium constant K_1. This pre-equilibrium is established within the dead time of the stopped-flow instrumentation, and gives rise to the t_0 extinction coefficient difference spectrum (Figure 6.2a). The ccNiR-(NH_2OH) adduct then undergoes three sequential changes governed by rate constants $k_2 - k_4$, respectively.
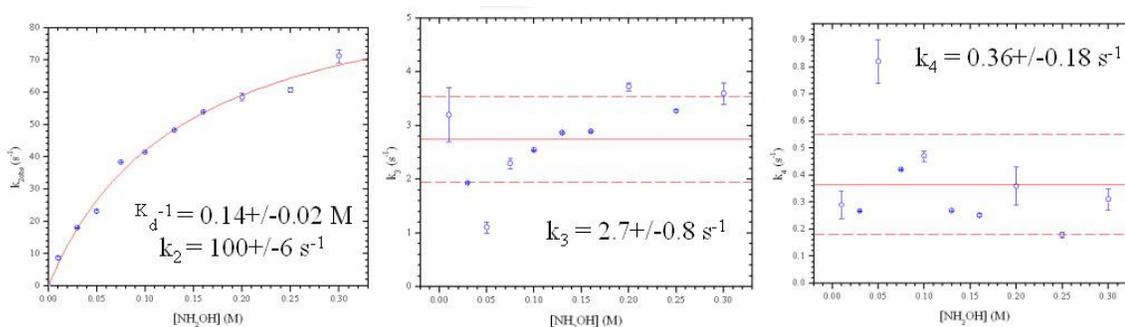
Figure 6.3. Kinetic rate constants as determined via UV/vis stopped flow experiments in the reaction of ccNiR$_{ox}$ and hydroxylamine. Three distinct kinetic events were observed. The first kinetic event was dependent of hydroxylamine concentration and the two subsequent events were independent of hydroxylamine concentration.
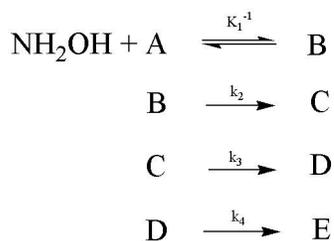
Scheme 6.1. Minimal model for the reaction of hydroxylamine with ccNiR$_{ox,}$ used to analyze the data.

The true rate constant k_2 for the first exponential event, together with the equilibrium constant K_1, were obtained by fitting the Figure 6.3a data to a rectangular hyperbola (Equation 6.1). From this, k_2 was determined to be 100 ± 6 s^{-1}, and K_1 140 ± 20 mM. The values of k_3 and k_4 were determined to be 2.7 ± 0.8 s^{-1} and 0.36 ± 0.18 s^{-1}, respectively, by averaging the values shown in Figures 6.3b and 6.3c.

$$k_{2obs} = \frac{k_2[NH_2OH]}{K_1^{-1} + [NH_2OH]} \tag{6.1}$$

6.3.2. Rapid freeze-quench EPR. The top trace in Figure 6.4 is the perpendicular mode EPR spectrum obtained for the resting *S. oneidensis* ccNiR$_{ox}$. It shows two of the three signals (g_y and g_z) at $g = 2.30$ and 1.52, respectively, that can be attributed to low-spin hemes with imidazoles that are parallel to each other on opposite sides of the heme plane (*12, 13*). The ccNiR crystal structure (Chapter 3) shows that hemes 2 and 3 have imidazoles parallel to each other, so one or both of these hemes could give rise to these signals. There are also signals at $g = 3.44$ that suggest the presence of a high-spin Fe(III) heme with $S = 5/2$ weakly anti-ferromagnetically coupled to a low-spin Fe(III) heme with $S = \frac{1}{2}$ (*13*). Parallel mode spectra were also collected for ccNiR$_{ox}$; these are shown in Appendix 4. The only high-spin heme in ccNiR is the Heme 1 active site, so we attribute these signals to coupling between the active site and the adjacent heme 3 (see Figure 3.1, Chapter 3). This then leads us to assign the g_y and g_z signals solely to heme 2, in agreement with the earlier work of Bamford et al. with the *E. coli* ccNiR (*13*).
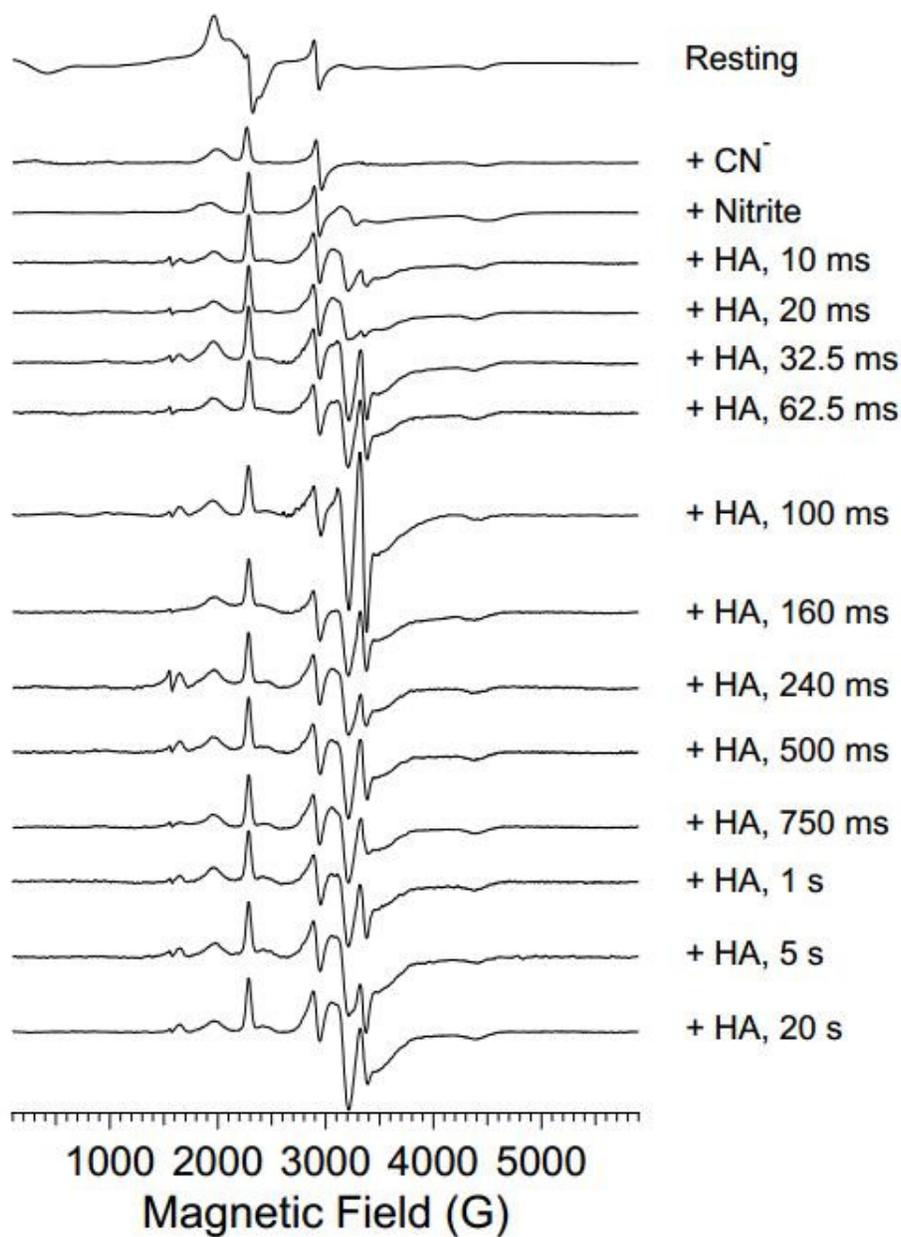
Figure 6.4. Results of standard X-band EPR and rapid freeze-quench X-band EPR. All data were collected in perpendicular mode, with the rapid freeze-quench spectra collected at a frequency of 9.63 GHz and all other data collected at 9.39 GHz. Background hydroxylamine and copper signals were subtracted, and signals were normalized to the peak at 2290 G.

Addition of a strong-field ligand such as nitrite or cyanide leads to significant changes in the EPR spectrum (second and third traces in Figure 6.4). The signals attributable to the anti-ferromagnetically coupled high-spin heme are now absent, and all three signals (g_x, g_y, and g_z) for low-spin hemes with $S = \frac{1}{2}$, and imidazoles parallel to the heme plane, are clearly visible. In addition, a "Highly Anisotropic Low-Spin" (HALS) signal is also now visible at $g = 3.47$. This type of signal has been attributed to low-spin hemes with imidazoles perpendicular to each other on opposite sides of the heme plane (*12, 13*). The imidazoles for hemes 4 and 5 in ccNiR have this orientation (Figure 3.1, Chapter 3), so we assign this signal to these hemes.

The 4th to 15th EPR spectra in Figure 6.4 were obtained in rapid freeze-quench experiments in which 50 μM ccNiR were mixed with 200 mM NH_2OH, as described in Section 6.2. The spectrum for the first time point at 10 ms is quite similar to that of ccNiR$_{ox}$ in the presence of the strong-field ligands nitrite or cyanide: the high-spin heme signal is no longer detectable, and both the HALS signal for parallel imidazoles and the g_x, g_y, and g_z signals for perpendicular imidazoles are clearly visible. This is consistent with the establishment of a rapid pre-equilibrium in which hydroxylamine binds ccNiR$_{ox}$, as shown in the first step of Scheme 6.1. Presumably, coordination of hydroxylamine to the heme center is accompanied by a high-spin to low-spin transition at the active site.

After the first 10 ms there are surprisingly few changes in the EPR spectrum of the NH_2OH –ccNiR reaction mixture, with the important exception of a signal at $g = 2.002$ that rises to maximum intensity within 100 ms, and then drops to a background intensity of ~20% (Figure 6.4 and 6.5). This signal is clearly attributable to a free radical species. For the reaction conditions given, 100 ms corresponds to the time at which the

first stopped-flow kinetic intermediate (see previous Section) is expected to reach a maximum concentration. We therefore assign this first kinetic process to a one-electron transfer from the hydroxylamine moiety to the ccNiR heme pool, which generates a $NH_2O\cdot$ radical seen by EPR, and the reduced heme signal seen by UV/Vis. The model is outline in Scheme 6.2, which is a refined version of Scheme 6.1 that takes into account not only the EPR and stopped-flow results, but also the results presented in the next section.
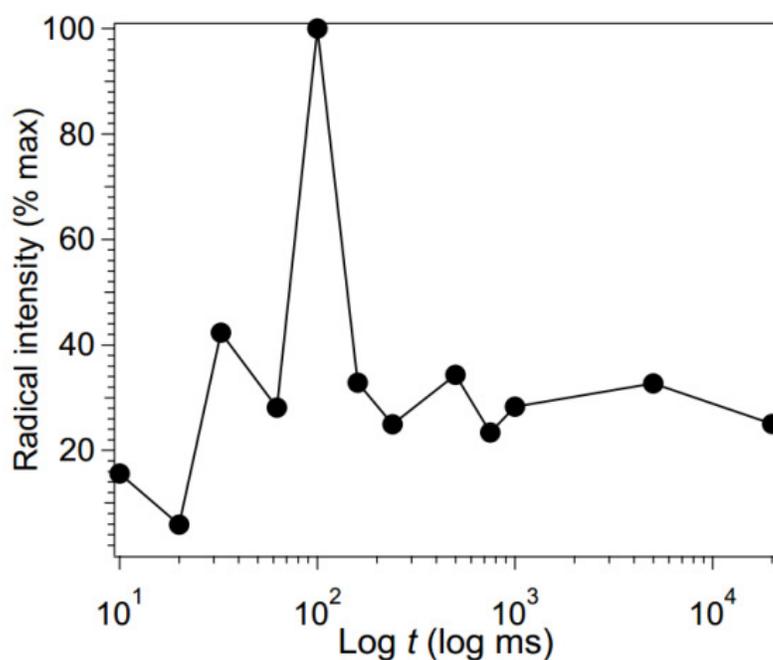
Figure 6.5. Graph of the relative intensity of the signal at $g = 2.002$ in the rapid freeze-quench EPR experiments. The maximum intensity was at the 100 ms time-point, and thereafter the signal remained constant at ~30% of the maximum relative intensity.

$$ccNiR_{ox} + NH_2OH \xrightleftharpoons{K_d^{-1}} [ccNiR_{ox}\text{-}NH_2OH] \quad (1)$$
$$\underset{A}{} \qquad\qquad\qquad\qquad \underset{B}{}$$

$$[ccNiR_{ox}\text{-}NH_2OH] \xrightleftharpoons{k_2} [ccNiR_{red1}\text{-}NH_2O\bullet] + H^+ \quad (2)$$
$$\underset{B}{} \qquad\qquad\qquad\qquad \underset{C}{}$$

$$[ccNiR_{red1}\text{-}NH_2O\bullet] \xrightleftharpoons{k_3} [ccNiR_{red2}\text{-}HNO] + H^+ \quad (3)?$$
$$\underset{C}{} \qquad\qquad\qquad\qquad \underset{D}{}$$

$$[ccNiR_{red2}\text{-}HNO] + NH_2OH + H_2O \xrightleftharpoons{k_4} [ccNiR_{red4}\text{-}NH_2OH] + NO_2^- + 3H^+ \quad (4)?$$
$$\underset{D}{} \qquad\qquad\qquad\qquad\qquad\qquad \underset{E}{}$$

$$ccNiR_{ox} + 2NH_2OH + H_2O \xrightleftharpoons{K_{eq}} [ccNiR_{red4}\text{-}NH_2OH] + NO_2^- + 5H^+ \quad (Net)$$
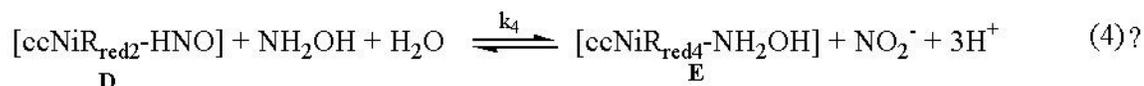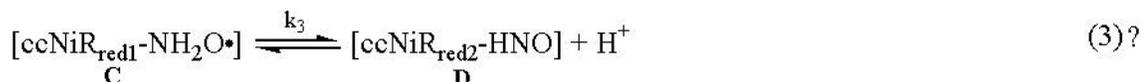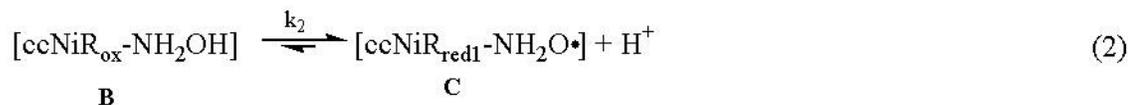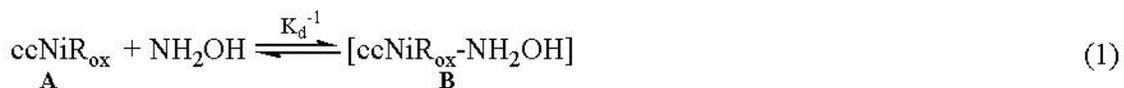
Scheme 6.2. Proposed scheme for the reaction of $ccNiR_{ox}$ and hydroxylamine. Equation 1 shows $ccNiR_{ox}$ and hydroxylamine establishing a rapid pre-equilibrium where hydroxylamine is bound to the active site and no electron transfer has taken place. Equation 2 shows the deprotonation of bound hydroxylamine, the 1 e^- reduction of ccNiR, and the formation of a free-radical on the bound substrate. The back reaction in Equation 2 is depicted as being relatively small compared to the forward reaction due to the concentration of Species C being independent of hydroxylamine concentration. Equation 3 is somewhat ambiguous, yet there has to be an event where ccNiR becomes further reduced by 1 e^-. Finally, Equation 4 shows a 2 e^- reduction of ccNiR, nitrite being produced, and hydroxylamine again binding to the active site due to the initial pre-equilibrium shown in Equation 1.

6.3.3. Assays for free reactive nitrogen species. Solutions containing 200 mM

NH$_2$OH and amounts of ccNiR varying from 1 - 90 µM were allowed to react

anaerobically for ~15 min, filtered to remove the enzyme, and then analyzed for the

presence of NO, NO$_2^-$ and NH$_4^+$, as described in Section 6.2. Of the three nitrogenous

species only NO$_2^-$ was detected. The observed dependence of [NO$_2^-$] on total [ccNiR]

(Figure 6.6) is consistent with establishment of the net equilibrium shown at the bottom

of Scheme 6.2. The Figure 6.6 data were fitted to Equation 6.2 (black trace in Figure

6.6), which yielded a value of K$_{eq}$ = 0.4 µM.
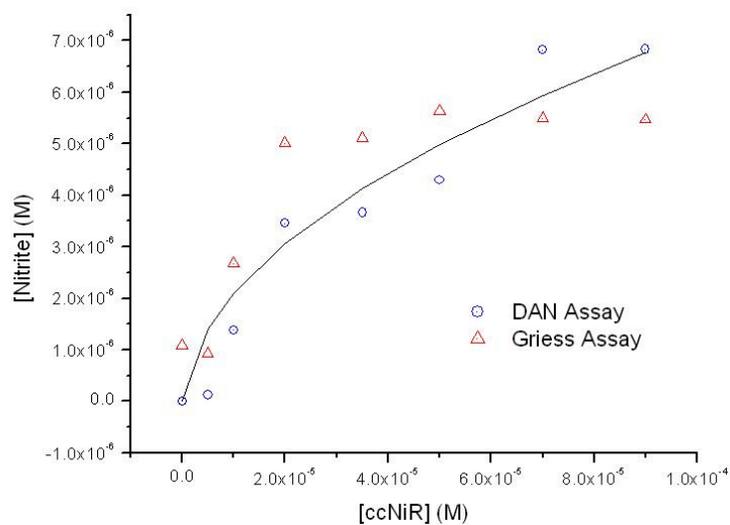
Figure 6.6. Results of the nitrite detection assays. Both the colorimetric Griess assay

and the fluorometric DAN assay were used (*8, 9*). Reactions were run in the presence of

200 mM hydroxylamine, which was then rendered inert via mixing with sodium pyruvate

once the reaction was complete.

$$[NO_2^-]_{free} = -0.5K_{eq} + 0.5\sqrt{K_{eq}^2 + 4K_{eq}[ccNiR]_t}$$

$$(6.2)$$

6.4. Discussion

In the first step of the oxidation of hydroxylamine by $ccNiR_{ox}$ both the stopped-flow and EPR data show that an event has occurred within the dead-time of the experiments. This suggests that a rapid pre-equilibrium is being established between the enzyme and substrate (Equation 1 in Schemes 6.1 and 6.2). In the first time-point of the rapid freeze-quench EPR experiments no signal attributable to high-spin heme is detected, suggesting that hydroxylamine has bound to ccNiR and induced a high-spin to low-spin transition (Figure 6.4, trace 4). At this same point in the reaction, the stopped-flow data show that minimal reduction of ccNiR has occurred. Therefore, at the very beginning of the reaction, hydroxylamine has bound to the active site of ccNiR and induced a transition from high-spin heme to low-spin, but no electron transfer has yet occurred.

The second step in the reaction is characterized by the one-electron reduction of ccNiR, forming $ccNiR_{red1}$, and a free-radical (Equation 2 in Scheme 6.2). In the stopped-flow experiments, the $ccNiR_{red1}$ signal reaches a maximum at ~96 ms. This correlates quite well with the rapid freeze-quench EPR 100 ms time-point, where the maximum intensity of the free radical signal at $g = 2.002$ is observed (Figures 6.4, 6.5). This leads to the conclusion that a free radical is forming on the bound substrate simultaneously with the one-electron reduction of ccNiR. Given the known chemistry of hydroxylamine, the unpaired electron is most likely on the oxygen atom of the substrate molecule (*14*), although experiments with ^{15}N-labeled hydroxylamine would have to be carried out in order to explicitly confirm this.

At this point in the catalytic process, the EPR data show that the intensity of the free-radical diminishes, but does not disappear completely, and no other changes in the EPR spectra are readily detectable. However, there are significant changes in the stopped-flow data. At first the amplitudes at 402 nm and 422 nm continue to increase for approximately one second, suggesting further reduction of the ccNiR heme pool (Figures 6.1, 6.2). The associated component is referred to as ccNiR$_{red2}$ in Scheme 6.2. Over the final 30 seconds of the reaction the intensity of the 422 nm signal decreases slightly and shifts to the red. Scheme 6.2 suggests that nitrite release occurs during this final event, though this suggestion is highly speculative for now.

Overall Scheme 6.2 provides one possible mechanistic interpretation of the stopped-flow, EPR and mass balance experiments performed to date. For now the evidence for the first two steps of the scheme, as well as for the overall net equilibrium, is fairly strong. Steps 3 and 4 are more speculative, and further experiments will be needed to put the theory on a stronger footing. A particular weakness of the current analysis is that it completely neglects the dimeric nature of ccNiR, and instead treats the subunits as uncoupled monomers. This is a very crude approximation, which may be hiding some interesting details of the system, and its validity will need to be further assessed in future.

Our data so far provide one other important insight. As shown in Scheme 6.3, the disproportionation of hydroxylamine at pH 7 is a highly favorable process, with ε° = +0.62 V. Furthermore, at first glance ccNiR would seem to be an ideal catalyst for hydroxylamine disproportionation, as shown schematically in Figure 6.7. One sees from this figure that if there is hydroxylamine oxidation occurring at the active site of one protomer, the electrons produced in this reaction could be transferred to the active site of

the other protomer, where hydroxylamine could be then reduced to ammonia. Given the high driving force for the disproportionation reaction, one might have expected to see large quantities of nitrite and ammonia generated under the reaction conditions of Figure 6.6, in which 200 mM of hydroxylamine and no disproportionation products were present at the outset. And yet, the results of Section 6.3.3 clearly show that though hydroxylamine can reduce ccNiR stoichiometrically and release sub-stoichiometric amounts of nitrite in the process, it does not disproportionate in the presence of the enzyme. If it did, large quantities of both nitrite and ammonia should have been detected.

$$2NH_2OH + 6H^+ + 4e^- \longrightarrow 2NH_4^+ + H_2O \qquad \varepsilon^o_1 = 0.89V$$

$$NH_2OH + H_2O \longrightarrow NO_2^- + 5H^+ + 4e^- \qquad -\varepsilon^o_2 = -0.27V$$

$$\overline{3NH_2OH + H^+ \longrightarrow 2NH_4^+ + NO_2^- + H_2O \qquad \varepsilon^o_{disp} = 0.62V}$$
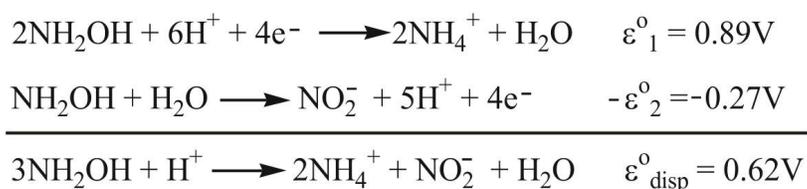
Scheme 6.3. Scheme showing the reduction of hydroxylamine to ammonia and the oxidation of hydroxylamine to nitrite, along with the associated thermodynamic potentials. If disproportionation were to occur, then these equations would combine to form the bottom reaction, which is quite thermodynamically favorable.
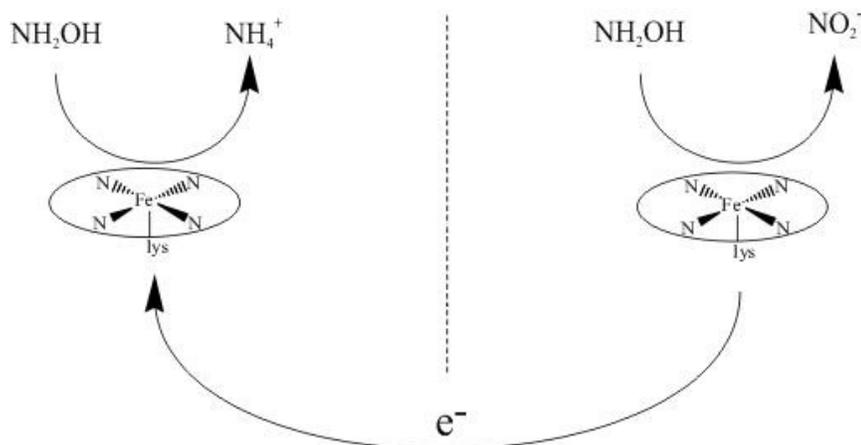
Figure 6.7. Depiction of a scenario where hydroxylamine is being oxidized to nitrite at the active site of one monomer of ccNiR, and the electrons produced in this reaction are then transferred across the dimer interface to the active site of the other monomer, where hydroxylamine is reduced to ammonia.

CcNiR *can* stoichiometrically oxidize NH_2OH to NO_2^- on the timescale of seconds, even though the equilibrium for the reaction lies far to the left ($K_{eq} = 0.4\ \mu M$ from analysis of the Figure 6.6 data). The ccNiR hemes provide a natural path for transferring electrons between NH_2OH moieties bound to active sites on separate subunits (Chapter 3, Figure 3.3), so it seems unlikely that electron flow provides the barrier to disproportionation. This leaves the thermodynamically very favorable reduction of NH_2OH to NH_4^+ as the most likely *kinetic* barrier to disproportionation.

We suggest that NH_2OH reduction to NH_4^+ at a heme center may take place via a process akin to Scheme 6.4, in which loss of water results in formation of the species notionally represented by the resonance structures "B". Such a species would be stable

only when the ccNiR hemes collectively provide sufficient electron density to make B effectively an amide bound to Fe (right resonance form). According to this scenario, NH_2OH disproportionation does not occur because the oxidative half reaction doesn't poise the hemes at sufficiently low potentials to stabilize intermediate B. At present the Scheme 6.4 mechanism is purely speculative; however, the methods described in this dissertation provide several approaches to testing and refining this mechanism. For example, in future experiments Ru-labeled ccNiR could be exposed to high hydroxylamine concentrations, and then photo-reduced using the methodology described in Chapter 4. In this way it should be possible to determine very precisely the extent of heme reduction needed in order to effect reduction of the bound hydroxylamine. It should also be possible to determine whether the reduction of bound hydroxylamine is a concerted two-electron process, as suggested in Scheme 6.4, or whether it can take place via one-electron steps.
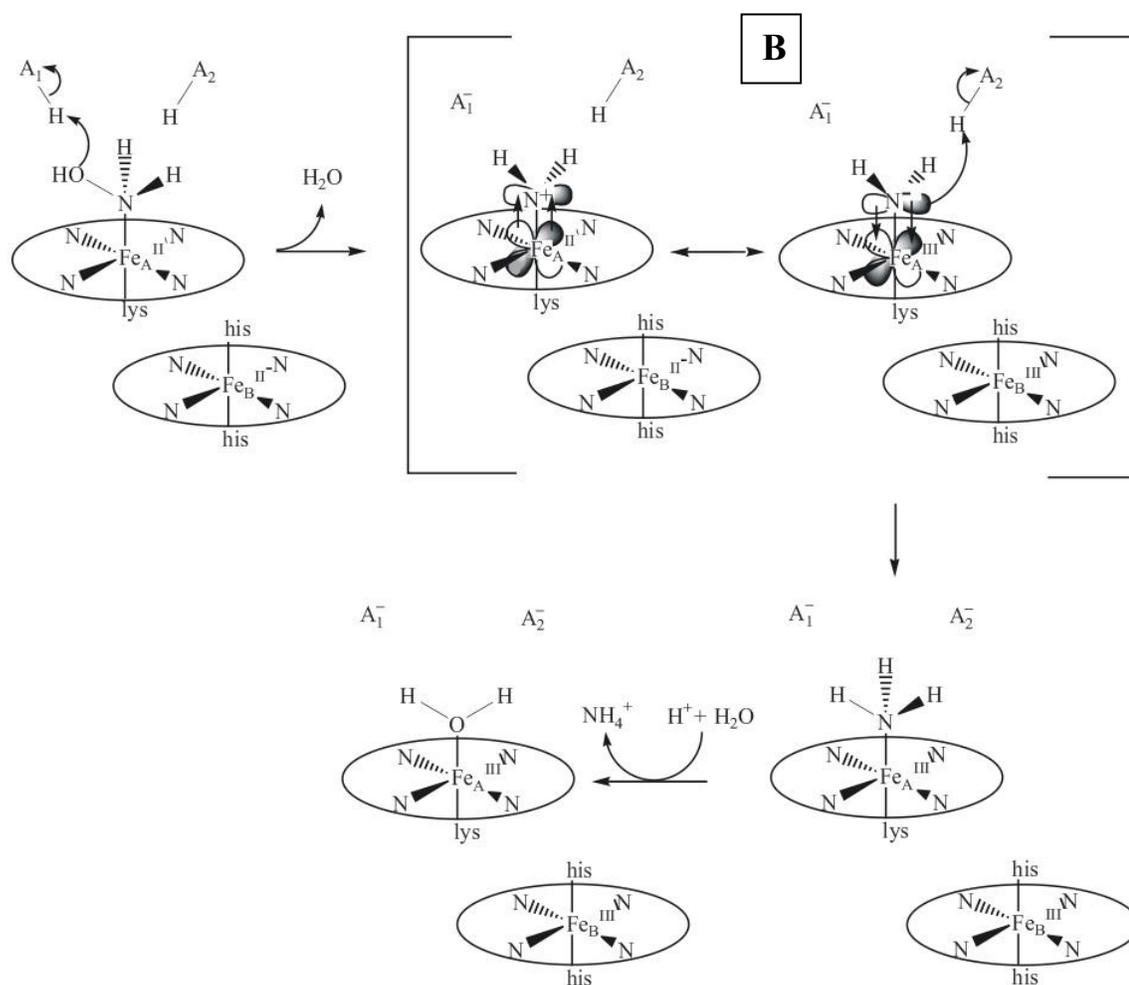
Scheme 6.4. Depiction of a possible manner in which hydroxylamine is reduced to ammonia by ccNiR.

6.5. References

1.   Ehrlich, H. L. (2002) *Geomicrobiology*, 4th ed., Marcel Dekker, Inc, New York, NY.

2.   Fenchel, T., King, G. M., and Blackburn, T. H. (1998) *Bacterial Biogeochemistry*, 2nd ed., Academic Press, London.

3.   Kostera, J., Youngblut, M. D., Slosarczyk, J. M., and Pacheco, A. A. (2008) Kinetic and product distribution analysis of NO reductase activity in *Nitrosomonas europaea* hydroxylamine oxidoreductase, *J. Biol. Inorg. Chem. 13*, 1073-1083.

4.   Kostera, J., McGarry, J. M., and Pacheco, A. A. (2010) Enzymatic Interconversion of Ammonia and Nitrite: the Right Tool for the Job, *Biochemistry 49*, 8546-8553.

5.   Purwar, N., McGarry, J. M., Kostera, J., Pacheco, A. A., and Schmidt, M. (2011) Interaction of nitric oxide with catalase: structural and kinetic analysis, *Biochemistry 50*, 4491-4503.

6.   Cabail, M. Z., Moua, V., Bae, E., Meyer, A., and Pacheco, A. A. (2007) Quantifying the photoinduced release of nitric oxide from N,N'-bis(carboxymethyl)-N,N'-dinitroso-1,4-phenylenediamine. Effect of reducing agents on the mechanism of the photoinduced reactions, *J. Phys. Chem. A 111*, 1207-1213.

7.   Youngblut, M., Judd, E. T., Srajer, V., Sayyed, B., Goelzer, T., Elliott, S. J., Schmidt, M., and Pacheco, A. A. (2012) Laue crystal structure of *Shewanella*

oneidensis cytochrome *c* nitrite reductase from a high-yield expression system, *J. Biol. Inorg. Chem. 17*, 647-662.

8. Griess, P. (1879) Ueber einige azoverbindungen, *Chemische Berichte 12*, 426-428.

9. Nussler, A. K., Glanemann, M., Schirmeier, A., Liu, L., and Nussler, N. C. (2006) Fluorometric measurement of nitrite/nitrate by 2,3-diaminonaphthalene, *Nat. Protocols 1*, 2223-2226.

10. Gouterman, M. (1978) Optical Spectra and Electronic Structure of Porphyrins and Related Rings, In *The Porphyrins V3* (Dolphin, D., Ed.), pp 1-166, Academic Press, Inc.

11. Adar, F. (1978) Electronic Absorption Spectra of Hemes and Hemoproteins, In *The Porphyrins V3* (Dolphin, D., Ed.), pp 167-210, Academic Press, Inc.

12. Walker, F. A. (1999) Magnetic spectroscopic (EPR, ESEEM, Mossbauer, MCD and NMR) studies of low-spin ferriheme centers nad their corresponding heme proteins, *Coord. Chem. Rev. 186*, 471-534.

13. Bamford, V. A., Angove, H. C., Seward, H. E., Thomson, A. J., Cole, J. A., Butt, J. N., Hemmings, A. M., and Richardson, D. J. (2002) Structure and spectroscopy of the periplasmic cytochrome c nitrite reductase from Escherichia coli, *Biochemistry 41*, 2921-2931.

14. Wieghardt, K. (1984) In *Advances in Inorganic and Bioinorganic Mechanism, Vol 3* (Sykes, A. G., Ed.), p 213, Academic Press, London.

Chapter 7

Conclusion

7.1. Concluding remarks

As shown in this dissertation, several benchmarks have now been reached on the way to developing a methodology for the use of time resolved crystallography to study ccNiR, which is a major long-term goal for the Pacheco group. First, an overexpression system for ccNiR in *S. oneidensis* was developed. It was determined that this overexpression system yielded ~30× more protein in the crude cell lysate than the wild-type organism. Additionally, an optimized purification scheme was developed which yielded highly pure protein, with a yield of ~40% compared to the crude cell lysate. An added advantage of having an overexpression system is that it allows for the generation of mutants. This advantage was exploited in the preparation of surface-modified ccNiR to which a photoactive Ru complex could be attached (see Chapter 4 and below). More recently co-workers in the Pacheco group have also generated active site mutants of ccNiR, which will allow for the further study of the catalytic mechanism of this protein.

Once a large amount of protein was made available via the aforementioned overexpression system, crystals of ccNiR of sufficient quality for crystallographic analysis were eventually obtained. These crystals did not yield usable crystallographic data using traditional cryo-X-ray diffraction methods, yet high-quality data *were* obtained using the Laue technique at room temperature. From these data the crystal structure of *S. oneidensis* ccNiR was determined to a resolution of 2.59 Å. To our knowledge, this is the first time that the crystal structure of a protein was solved using Laue X-ray

crystallography prior to being solved using traditional methods. This result was fortuitous as it showed not only that the structure of *S. oneidensis* ccNiR could be solved for protein obtained using our expression system, but also that the crystals were of sufficient quality for use with the Laue X-ray crystallography technique. This was not a foregone conclusion, as the Laue method usually requires substantially better quality crystals than the conventional method; in particular, this method is highly sensitive to mosaicity (*1*). Given that time resolved crystallography requires the use of the Laue technique, its use for solving the ccNiR structure was a significant milestone to reach.

The next benchmark that was reached on the path to a method for studying ccNiR via time-resolved crystallography was the development of a viable photo-initiation system. A photo-reduction method was sought in order to study the physiologically relevant ccNiR-catalyzed reductions of nitrite and other reactive nitrogen species. Initially, $Ru(bipy)_3^{2+}$ was employed as the photoactive species. This compound, in the presence of methyl viologen and EDTA, was found to readily reduce ccNiR in solution on the timescale of hundreds of microseconds to several milliseconds. This method is not readily adaptable to use in the solid state though; furthermore, in many instances the initial ccNiR reduction steps are slow enough to overlap subsequent electron transfers from the heme pool to bound nitrogenous species, which complicates data analysis. A better method was subsequently devised, in which a compound related to $Ru(bipy)_3^{2+}$ but containing an iodoacetimide moiety (Figure 4.2, Chapter 4), could be covalently linked to the surface cysteine of a ccNiR mutant. The Ru-labeled ccNiR was characterized using UV/visible and fluorescence spectroscopies, as well as MALDI-TOF mass spectrometry, and it was shown that photo-reduction of the labeled ccNiR in solution could be effected

using a 455 nm laser pulse. Importantly, reduction of the heme pool took place in less than 1 μs, which completely isolates the reductive process from subsequent electron transfer from the heme pool to bound reactive nitrogen species. For the preliminary studies presented herein ferrocyanide was used as a secondary electron donor (Scheme 4.3, Chapter 4), but more recent work by colleagues from the Pacheco group has shown that diethyldithiocarbamate is more suitable, as it renders the reduction process irreversible. Further studies are now under way to identify crystallization conditions for the Ru-labeled ccNiR, which are expected to be different from those used to crystalize the wild-type enzyme.

One final benchmark that was reached in this investigation was the use of spectroelectrochemistry to determine the relative extinction coefficient spectra for the reduced ccNiR species. Analysis of these data revealed that ccNiR is reduced via five distinct one-electron transfer events, each of which gives rise to its own UV/Vis spectroscopic signature. Additionally, analysis showed that individual hemes cannot be assigned to each reduced species. Rather, as each electron is put into the ccNiR system, it is delocalized over multiple hemes. The relative extinction coefficient spectra for each of the five reduced ccNiR species that were obtained in this study will ultimately be needed for interpreting time-resolved UV/Vis experiments with ccNiR, such as those outlined in Chapter 4. In turn, the time-resolved UV/Vis experiments will be essential for planning the time-resolved crystallography experiments.

In addition to the results described in Chapters 2-5, which were directly aimed at laying the groundwork for applying time-resolved crystallography to the study of ccNiR, the discovery that ccNiR can oxidize hydroxylamine with nitrite as the sole nitrogenous

product (Chapter 6) also provided important mechanistic insights about ccNiR's reaction mechanism. UV/visible stopped-flow and rapid freeze-quench EPR data, along with product analysis, showed that the equilibrium between hydroxylamine and nitrite is fairly rapidly established in the presence of large initial concentrations of hydroxylamine, even though said equilibrium lies far to the left. By contrast reduction of hydroxylamine to ammonia did not occur, even though disproportionation of hydroxylamine to yield both nitrite and ammonia would be strongly favored thermodynamically under the reaction conditions. This suggests that there is a kinetic barrier that prevents the ccNiR-catalyzed reduction of hydroxylamine to ammonia. While hydroxylamine oxidation by ccNiR is unlikely to have any physiological relevance, the study does lead to hypotheses about how the enzyme operates physiologically, as shown for example in Scheme 6.4 (Chapter 6). These hypotheses are already being tested, and are also being used to guide the design of experiments by the Pacheco group's next generation of graduate students.

7.2. References

1.   Schmidt, M. (2008) Structure Based Enzyme Kinetics by Time-Resolved X-ray crystallography, In *Ultrashort Laser Pulses in Medicine and Biology* (Zinth, W., Braun, M., and Gilch, P., Eds.), Springer Verlag.

Appendix 1

Supplementary Material to Chapter 2

A1.1. Comparison between the wild-type ccNiR gene and the optimized gene used for over-expression.

Figure A1.1. Gene sequence for wild-type and optimized ccNiR gene.

Appendix 2

Supplementary Material to Chapter 3

A2.1. Molecular packing in orthorhombic and monoclinic crystal forms
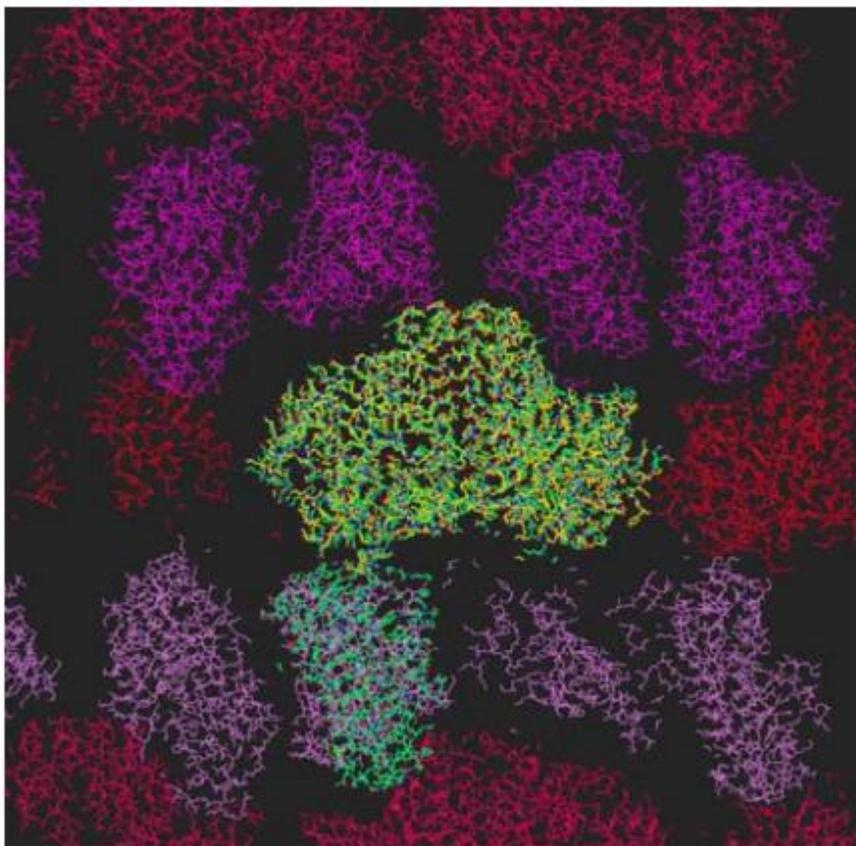
Figure A2.1. The content of the asymmetric unit in the orthorhombic crystals is shown in yellow, and dimers related by crystallographic symmetry are shown in red and purple tones. One of the two dimers (green) in the asymmetric unit of the monoclinic crystals is superimposed by least squares fitting on the yellow dimer. The non-crystallographically related second dimer is also shown in green. One can easily identify the rotation that breaks the symmetry. If the green dimer were to remain at the same position as the purple dimer, crystals would remain orthorhombic.

Appendix 3

Supplementary Material to Chapter 5

A3.1. Spectropotentiometric analysis of ccNiR

A3.1.1. Derivation of Equation 5.1. Using the terminology presented in Scheme 5.1, we can write the Nernst equations that relate two given ccNiR species C_n and C_{n-1}, as shown in Eqs. A3.1 – A3.5.

$$\varepsilon_{app} = \varepsilon_1^o - \frac{RT}{nF} \ln \frac{C_1}{Ox} \tag{A3.1}$$

$$\varepsilon_{app} = \varepsilon_2^o - \frac{RT}{nF} \ln \frac{C_2}{C_1} \tag{A3.2}$$

$$\varepsilon_{app} = \varepsilon_3^o - \frac{RT}{nF} \ln \frac{C_3}{C_2} \tag{A3.3}$$

$$\varepsilon_{app} = \varepsilon_4^o - \frac{RT}{nF} \ln \frac{C_4}{C_3} \tag{A3.4}$$

$$\varepsilon_{app} = \varepsilon_5^o - \frac{RT}{nF} \ln \frac{C_5}{C_4} \tag{A3.5}$$

In exponential form these equations can be re-written in the forms shown in Eqs. A3.6 and A3.7:

$$C_1 = Ox \times E_1 \tag{A3.6}$$

$$C_n = C_{n-1} \times E_n \tag{A3.7}$$

where E_n is defined by Eq. 5.1c from Chapter 5:

$$E_n = \exp\left[\frac{nF}{RT}(\varepsilon_n^o - \varepsilon_{app})\right] \tag{5.1c}$$

Now the total concentration of ccNiR, C_T, will be the given by the sum of the various species present at any given applied potential (Eq. A3.8). All of the species except Ox can be eliminated from Eq. A3.8 by substituting each C_n value with the expressions A3.6, A3.7. The result is shown in

$$C_T = Ox + \sum_{n=1}^{5} C_n \tag{A3.8}$$

$$C_T = Ox\left\{1 + E_1\left[1 + E_2\left[1 + E_3\left(1 + E_4(1 + E_5)\right)\right]\right]\right\} \tag{A3.9}$$

Eq. A3.9. Solving for Ox gives Eq. A3.10, where the large term in the denominator has been abbreviated as "denom" (Eq. 5.1b from Chapter 5). Finally, by performing successive substitutions into Eqs. A3.6 and A3.7, all of the C_n species can be rewritten in terms of C_T, as shown in Eq. 5.1a of Chapter 5.

$$Ox = \frac{C_T}{denom} \tag{A3.10}$$

$$denom = 1 + E_1\left\{1 + E_2\left[1 + E_3\left(1 + E_4(1 + E_5)\right)\right]\right\} \tag{5.1b}$$

$$C_n = \frac{C_T \times \prod\limits_1^n E_n}{denom} \tag{5.1a}$$

A3.1.2. Beer's law for difference spectra. We begin by eliminating Ox from the Beer's law expression (Eq. A3.11) by first solving for Ox in Eq. A3.8 (which yields Eq. A3.12), and then

$$A_\lambda = \left(\epsilon_{ox\lambda}Ox + \sum_{n=1}^{5}\epsilon_{n\lambda}C_n\right) \times l \tag{A3.11}$$

substituting Ox using the Eq. A3.12 expression to give Eq. A3.13. In these equations A_λ is the absorbance at a given wavelength λ, $\epsilon_{ox\lambda}$ and $\epsilon_{n\lambda}$ are the extinction coefficients of the oxidized

$$Ox = C_T - \sum_{n=1}^{5}C_n \tag{A3.12}$$

$$A_\lambda = \left\{\epsilon_{ox\lambda}\left[C_T - \left(\sum_{n=1}^{5}C_n\right)\right] + \sum_{n=1}^{5}\epsilon_{n\lambda}C_T\right\} \times l \tag{A3.13}$$

and nth reduced species at that wavelength, and l is the cell pathlength. In the absence of applied potential, all of the ccNiR is in the oxidized form, and Eq. A3.13 simplifies to Eq. A3.14, where $A_{0\lambda}$ is the absorbance of fully oxidized ccNiR at λ. If we use Eq. A3.14 to substitute for $\epsilon_{ox\lambda}C_T$ in Eq. A3.13 we get, after rearrangement, Eq. A3.15. Straightforward rearrangement of the summations then yields the desired Eq. A3.16, in which $\Delta A_\lambda = A\lambda - A_{0\lambda}$ and $\Delta\epsilon\lambda = \epsilon_{n\lambda} - \epsilon_{ox\lambda}$. Equation 5.2 is a matrix

$$A_{0\lambda} = \epsilon_{ox\lambda}C_T l \tag{A3.14}$$

$$A_\lambda = \left(A_{0\lambda} - \epsilon_{ox\lambda}\sum_{n=1}^{5}C_n + \sum_{n=1}^{5}\epsilon_{n\lambda}C_T \right) \times l \tag{A3.15}$$

$$\Delta A_\lambda = l \times \sum_{n=1}^{n}\Delta\epsilon_{n\lambda}C_n \tag{A3.16}$$

form of Eq. A3.16, rearranged to give the extinction coefficient spectra as a function of the concentrations, absorbances and cell pathlength. Because the concentration matrix is not square and thus has no inverse, in Eq. 5.2 one must construct the pseudoinverse, as explained in Gates et al (*1*).

  A3.1.3. Complete description of the global analysis procedure. Initially, the absorbance difference data collected between 379 nm and 454 nm, for all potentials between +34 mV and -516 mV vs SHE, were subjected to singular value decomposition (SVD) analysis. This analysis revealed five components with U and V autocorrelation values greater than 0.8, and singular values above the noise background, as shown in

Section A3.4. All subsequent U and V components had autocorrelation values well below 0.8, which corresponds roughly to s/n = 1 (*2*).

Selected ΔA_λ vs. ε_{app} traces of the SVD-processed data were next fitted to Eqs. 5.1 and A3.16 using the Levenberg-Marquardt routine supplied by Origin 6.0 (*1*). At some wavelengths it was possible to fit the ΔA_λ vs. ε_{app} slices with less than 5 potentials, because some of the $\Delta\epsilon_{n\lambda}$ were small at those wavelengths. For example, 420 nm and 430 nm data could be fitted with 4 and 3 potentials, respectively. Taken together, these initial analyses of individual ΔA_λ vs. ε_{app} slices provided rough guesses of the ε°_n values.

In the final step the entire SVD-processed data set was fit using Eqs. 5.1 and the matrix Eq. 5.2, using a program created with Mathcad 13. Briefly, this global analysis program first allows the user to manually enter trial values of the five midpoint potentials. For a given set of midpoint potential values the program then uses Eq. 5.1 to calculate the concentration of each reduced species at a given applied potential, and stores the concentrations in $\mathbf{C_{red}}$. $\mathbf{C_{red}}$, $\mathbf{\Delta A}$, and l are then used to calculate the matrix of extinction coefficient spectra $\mathbf{\Delta\epsilon}$ using Eq. 5.2. Finally, the program uses l and the $\mathbf{\Delta\epsilon}$ and $\mathbf{C_{red}}$ matrices to generate an absorbance matrix $\mathbf{\Delta A_{calc}}$, and the sum of squares for $\mathbf{\Delta A}$ $- \mathbf{\Delta A_{calc}}$ is computed. By varying the trial values of the five ccNiR midpoint potentials, this sum of squares can be minimized. The midpoint potentials obtained by fitting the single wavelength ΔA_λ vs. ε_{app} slices to Eqs. 5.1 and A3.16 were used as initial trial values in the global fit. These trial values proved to be excellent initial guesses, and only minor modifications to the ε^o_n values were needed in the subsequent sum of squares minimization procedure.

A3.1.4. Results of singular value decomposition analysis of the Soret region

data.
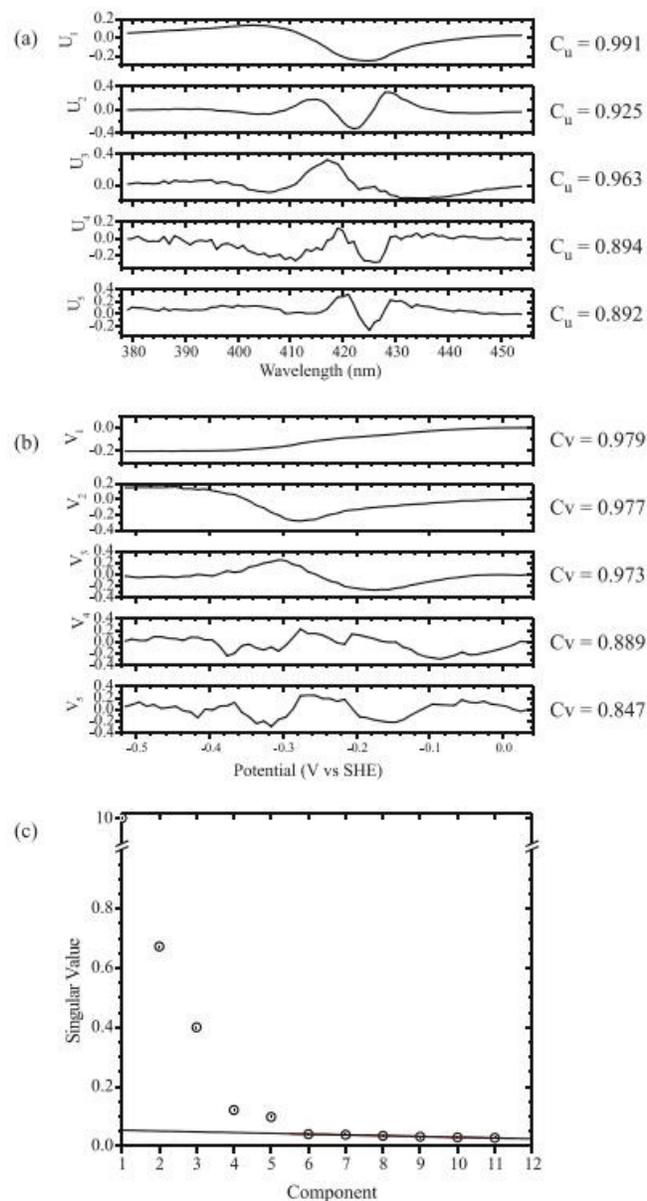
Figure A3.1. A: The 5 U components corresponding to singular values above the noise level, and their associated autocorrelation values C_U. **B:** The 5 V components corresponding to singular values above the noise level, and their associated autocorrelation values CV. **C:** Singular values of the first 11 components.

A3.1.5. Results of singular value decomposition analysis of the α,β region data.

The spectral region from 500 nm – 650 nm, where characteristic bands are observed for

reduced low-spin hemes (the α, β bands), was investigated in a manner analogous to that

described above and in the main paper for the Soret region. The absorbance difference

data collected between 500 nm and 650 nm, for all potentials between +34 mV and -516

mV vs SHE, were first subjected to SVD analysis. For this region, where the signals are

less intense than in the Soret region, inspection of the U and V autocorrelation values and

singular values unambiguously showed only four spectral components above the noise

background (Figs. A3.2a and A3.2b).
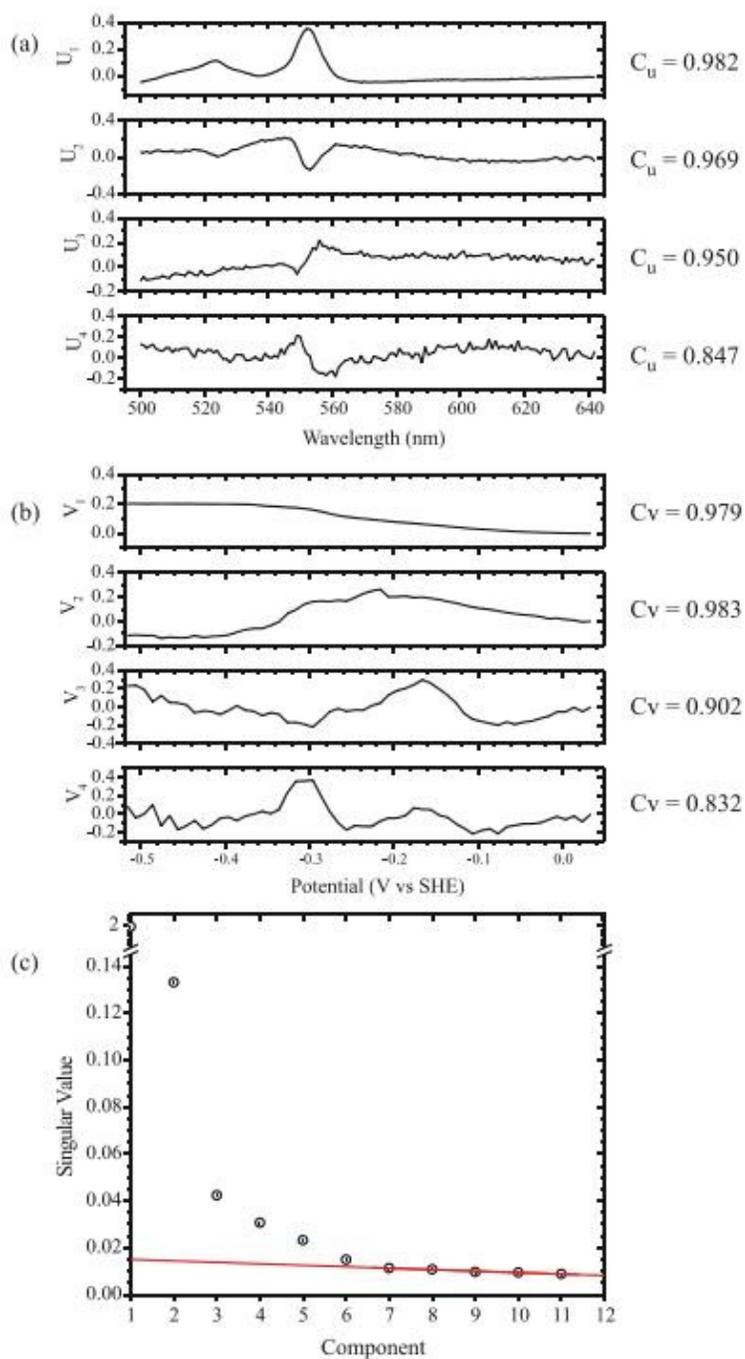
Figure A3.2. Analysis of the α,β region. **A:** The 5 U components corresponding to

singular values above the noise level, and their associated autocorrelation values C_U. **B:**

The 5 V components corresponding to singular values above the noise level, and their

associated autocorrelation values CV. **C:** Singular values of the first 11 components.

Initially, the new SVD-processed data set was fit directly to a 4-component version of the matrix Eq. 5.2, using a 4-component version of the Mathcad global analysis program described above and in Chapter 5, and using the optimized midpoint potential values obtained by fitting the 379 nm – 454 nm data as guiding initial guesses. The optimized midpoint potential values thus obtained are listed in Table A3.1; the values obtained from the Soret region are also given for comparison. Notice that ε^o_1, ε^o_2, and ε^o_4 correlate very well with the Soret values ε^o_1, ε^o, and ε^o_5, whereas the ε^o_3 value sits between the Soret ε^o_3 and ε^o_4 values. We interpret this to mean that the spectral changes seen in the α, β region are tracking the same electrochemical processes as those seen in the Soret region, but that the extinction coefficient difference spectra of the various reduced species are too similar to each other to give rise to 5 distinct components in the SVD. To explore this hypothesis we fitted the α, β region data using 5 potentials, but assuming that the extinction coefficient difference spectra $\Delta\epsilon_3$ and $\Delta\epsilon_4$ are identical. The results are listed in Table A3.1, representative fits are provided in Figure A3.3, and the calculated extinction coefficient difference spectra are given in Figure A3.4. In support of the model, the fits are slightly better than those obtained for the 4-potential 4-$\Delta\epsilon$ model, and excellent across the spectral region.

Soret region analysis	500nm - 650 nm region analysis		
5 spectra, 5 potentials	4 spectra, 4 potentials[1]	4 spectra, 5 potentials	4 spectra, 4 potentials[2]
-0.063±0.008	-0.048	-0.045	-0.063
-0.148±0.006	-0.140	-0.139	□
-0.232±0.013	-0.269	-0.271	-0.232
-0.282±0.002		-0.301	-0.282
-0.338±0.002	-0.338	-0.336	-0.338
Sum of squares:	1.78E-03	1.73E-03	7.72E-03

[1.] No restrictions on midpoint potential values

[2.] Second reduction event is assumed to produce no absorbance change

Table A3.1. Midpoint potentials of ccNiR hemes (in V vs. SHE) obtained by spectropotentiometry. Comparison between values obtained by fitting the Soret region and those obtained by fitting the 500 - 650 nm region.
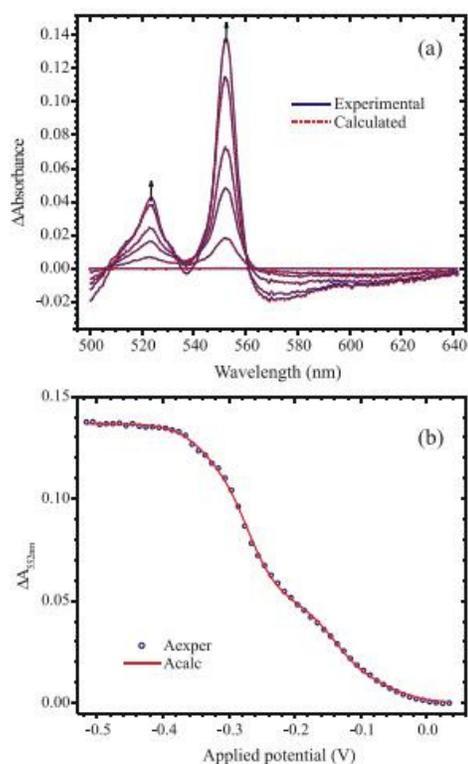
Figure A3.3. Best least-squares fit of the α,β spectral region data to a model with 5 midpoint potentials but only 4 extinction coefficient difference spectra, where C_3 and C_4 are assumed to have identical spectra.
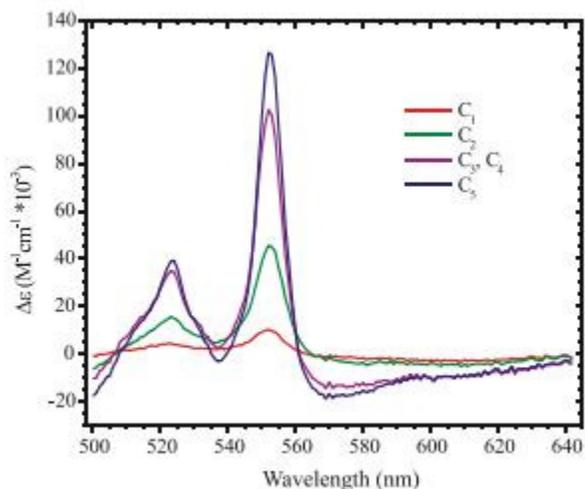
Figure A3.4. Extinction coefficient difference spectra calculated for the α,β spectral region using the model with 5 midpoint potentials and 4 extinction coefficients.

An alternative explanation for there being only 4 SVD components in the α, β region is that reduction of the high-spin active site (heme 1) does not result in significant spectral changes in this region. Certainly the sharp features seen at 552 nm and 524 nm are characteristic of (isolated) low-spin ferrous hemes and not high-spin ones (*3*). We tried fitting the 500 nm – 650 nm data to 4 potentials using the Soret ε^o_1 and $\varepsilon^o_3 - \varepsilon^o_5$ values as initial guesses, and assuming that the second reduction event did not produce a significant spectral change in this region (this assumes that the second reduction event corresponds to reduction of the high-spin active site heme, as concluded in studies of the *E. coli* protein). However, the fits thus obtained were substantially worse than those obtained with 4 potentials when the ε^o_3 is allowed to sit between the Soret ε^o_3 and ε^o_4 values, and the other midpoint potentials correlate 1:1 with the corresponding Soret values (Table A3.1). We conclude that every reduction event in *S. oneidensis* ccNiR

results in α,β region spectral changes of the type normally associated with reduction of low-spin ferri-hemes to the low-spin ferro form.

A.3.2. References

1.   Gates, A. J., Kemp, G. L., To, C. Y., Mann, J., Marritt, S. J., Mayes, A. G., Richardson, D. J., and Butt, J. N. (2011) The relationship between redox enzyme activity and electrochemical potential - cellular and mechanistic implications from protein film electrochemistry, *Phys. Chem. Chem. Phys. 13*, 7720-7731.

2.   Henry, E. R., and Hofrichter, J. (1992) Singular Value Decomposition: Application to Analysis of Experimental Data, In *Meth. Enzymol.* (Brand, L., and Johnson, M. L., Eds.), pp 129-192, Academic Press, San Diego.

3.   Kiefersauer, R., Than, M. E., Dobbek, H., Gremer, L., Melero, M., Strobl, S., Dias, J. M., Soulimane, T., and Huber, R. (2000) A novel free-mounting system for protein crystals: transformation and improvement of diffraction power by accurately controlled humidity changes, *J. Appl. Cryst. 33*, 1223-1230.

Appendix 4

Supplementary Material to Chapter 6

A4.1. Parallel mode EPR spectrum for ccNiR$_{ox}$
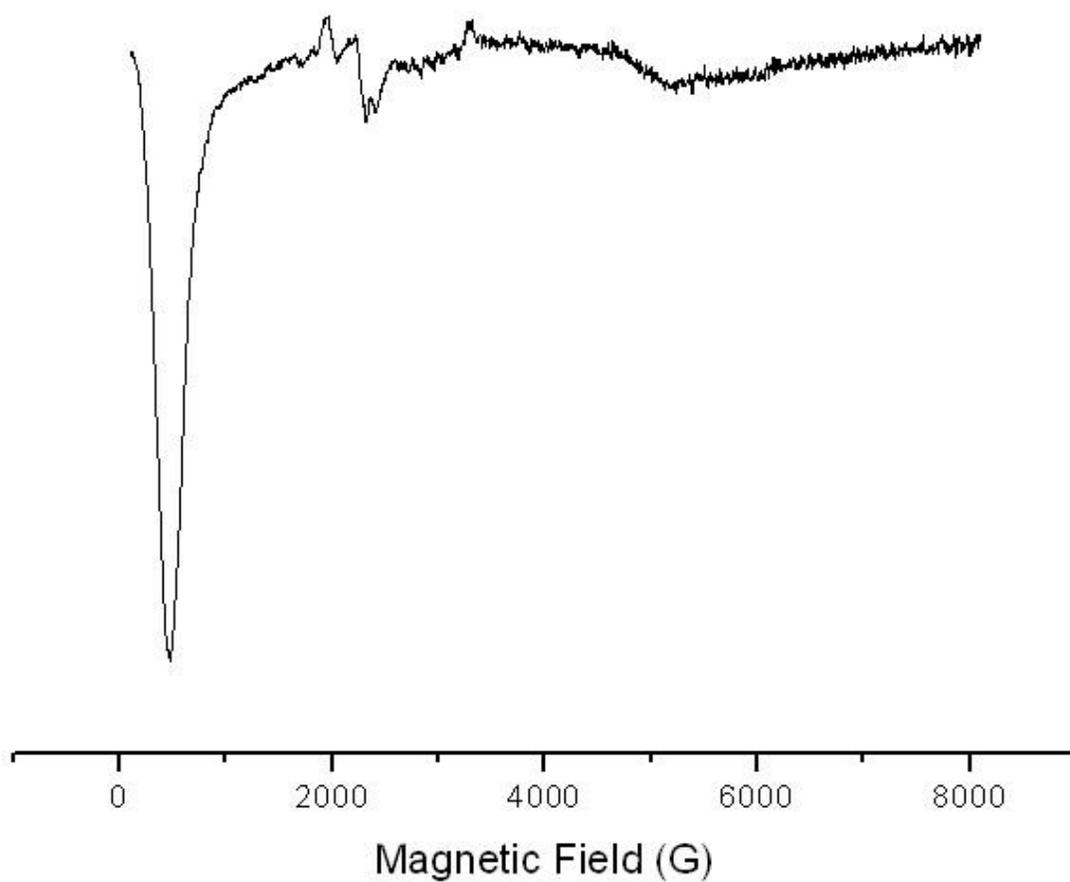
Figure A4.1. Parallel mode EPR spectrum for ccNiR$_{ox}$. The large spectral feature at $g \sim$ 7 is indicative of the presence of heme in a high-spin state.

A4.2. Selective dialysis of ammonia

   A.4.2.1. Selectively dialyzing ammonia from a high ionic strength solution. A
device for the selective dialysis of ammonia from an aqueous solution was obtained from
Dr. Joseph Aldstadt. The device consists of two plastic blocks with matching channels
etched into each piece so that when the two blocks are assembled together, a cylindrical
channel is formed (Figure A4.2). A piece of Teflon tape was placed between the blocks
to act as a membrane. Initially, the solution containing ammonia was titrated to pH 11
and then run through one side of the block in a closed loop using a peristaltic pump at a
rate of 1 mL/min. A 20 mM HEPES solution at pH 7 was left stationary on the other side
of the membrane. After 5 min, the pump was stopped, and the pH 7 solution was
withdrawn from the device and assayed for ammonia.
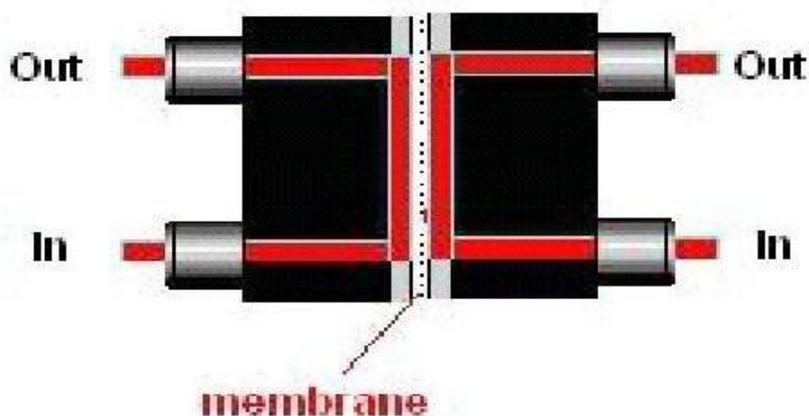
Figure A4.2. Depiction of the device for the selective dialysis of ammonia from an
aqueous solution. The left side of the device is the solution containing the ammonia at
pH 11, the membrane is Teflon tape, and the right side is the pH 7 buffer solution where
the ammonia accumulates after dialysis.

A.4.2.2. Results and discussion. Initially a standard curve was created using ammonium chloride in CAPS buffer as the source of ammonia (Figure A4.3). CAPS has a pK_a of 10.5, and is thus suitable for buffering at pH 11, which is necessary for converting all ammonium into deprotonated ammonia. Once the ammonia diffuses across the Teflon membrane, it becomes protonated in the pH 7 HEPES buffer, thus trapping the ammonia. Figure A4.3 shows that the modified assay has a linear response to ammonia. Furthermore, the assay can detect less than 10 μM ammonia, which is an improvement over the standard ammonia assay (*1*). This improvement is due to the concentrating effect that accompanies dialysis.

The reaction of hydroxylamine and $ccNiR_{ox}$ was run as described in Chapter 6, after which excess hydroxylamine was removed by reacting with pyruvate. When the treated reaction mixture was assayed for ammonia as described above, no ammonia was detected beyond the levels of a negative control in which the reaction was run in the absence of $ccNiR_{ox}$.

$$Y = (194.10163) X + 0.01096$$
$$R^2 = 0.91135$$
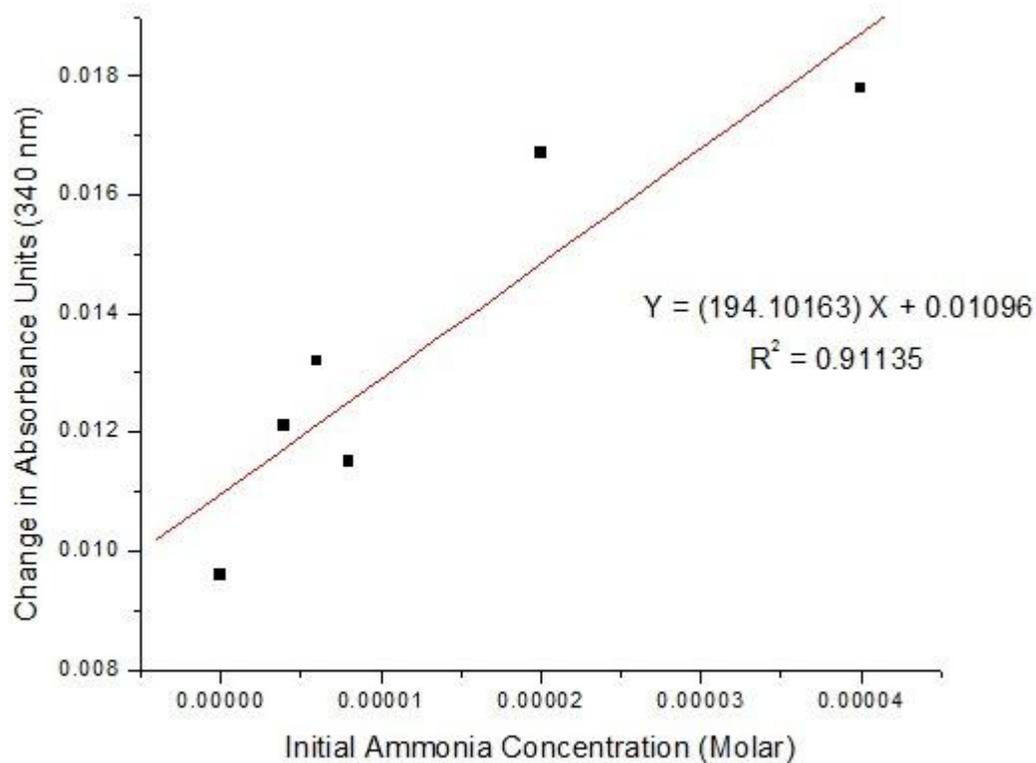
Figure A4.3. Standard curve for the ammonia assay using the ammonia dialysis device.

A4.3. References

1.   Neeley, W. E., and Phillipson, J. (1988) Automated Enzymatic Method for

        Determining Ammonia in Plasma, with 14-day Reagent Stability, *Clinical*

        Chemistry 34, 1868-1869.

Appendix 5

Protocol for the Preparation of Electrocompetent *S. oneidensis* TSP-C Cells

(Note: TSP-C strain has natural rifampicin resistance)

1) Inoculate 10 mL LB broth supplemented with 30 µg/mL rifampicin with either a single colony or 10 µL of frozen cell stock. Incubate overnight at 30°C @ 175 RPM.

2) Use all of the culture made in Step 1 to inoculate 1 L LB broth supplemented with 30 µg/mL rifampicin. Incubate at 30°C @ 175 RPM until $OD_{600} = 0.4$. (Note: it usually takes 90-120 min to reach the proper OD_{600}.)

3) Place flask in an ice water bath for 30 min. (***Note: from this point on, it is EXTREMELY IMPORTANT to keep all solutions and plasticware ice-cold to avoid heating the sample.***)

4) Centrifuge sample in ice-cold centrifuge tubes at $6000 \times g$ for 5 min. Remove supernatant with a sterile siphon attached to a vacuum flask.

5) Re-suspend cell pellet in ~100 mL ice-cold 10% glycerol in pure H_2O.

6) Repeat Steps 4 and 5 two more times.

7) After the third washing with ~100 mL ice-cold 10% glycerol solution, centrifuge the sample one last time at $6000 \times g$ for 5 min. Remove supernatant with a sterile siphon attached to a vacuum flask.

8) Resuspend sample in ~25 mL ice-cold 10% glycerol and transfer the sample to a conical centrifuge tube. Centrifuge at $4500 \times g$ for 10 min. Remove supernatant

with a sterile siphon attached to a vacuum flask, leaving behind a minimal amount of liquid. Resuspend pellet in remaining liquid.

9) Measure the OD_{600} of a 100× dilution of the resulting solution. The OD_{600} of the diluted solution must be between 0.8-1.0. If the OD_{600} of the diluted solution is greater than 1.0, dilute the sample with 10% ice-cold glycerol until the OD_{600} of the diluted sample is between 0.8-1.0. If the OD_{600} of the diluted sample is less than 0.8, try centrifuging the sample at 4500 x g and siphon off the supernatant in order to concentrate the cells to the proper OD_{600}.

10) Make 50 µL aliquots of cells in ice-cold cryotubes. Store samples at -80°C until needed.

Appendix 6

Protocol for the Electroporation of *S. oneidensis* TSP-C Cells

(Note: TSP-C strain has natural rifampicin resistance)

1) Thaw previously prepared electrocompetent *S. oneidensis* TSP-C cells on ice for 20 min. (***Note: it is EXTREMELY IMPORTANT that all solutions and plasticware are ice-cold until the cells are electroporated.***)

2) Add 2 µL of concentrated plasmid DNA to thawed cells. (Note: for best results, use a sample with plasmid DNA concentration of >500 ng/µL.) Flick tube 4-6 times to mix. Transfer sample to an ice-cold, sterile electroporation cuvette with a 2 mm gap. Incubate cell/DNA solution on ice for 15 min.

3) Moving quickly, wipe off moisture from the outside of the electroporation cuvette, place cuvette in electroporation device, and electroporate cells using a 2.5 kV pulse. (Note: using a voltage higher than 2.5 kV was detrimental and appeared to kill the cells.)

4) Immediately after electroporation, add 950 µL of room temperature SOC medium and mix the sample thoroughly. Transfer the sample to a 2 mL centrifuge tube.

5) Incubate the samples at 30°C, while shaking at 200 RPM, for 1 hour.

6) Plate varying amounts of sample onto LB agar plates supplemented with 20 mM $MgSO_4$, 30 µg/mL rifampicin, and the appropriate concentration of antibiotic that corresponds to the resistance gene on the plasmid used. (Note: it appears that *S. oneidensis* cannot have ampicillin resistance conferred onto it; however,

kanamycin resistance was conferred, and a concentration of 50 µg/mL of

kanamycin in cultures worked well.)

7) Incubate plates overnight at 30°C. Colonies of successful transformants should

appear in 16-32 hours.

Matthew D. Youngblut

Curriculum Vitae

Professional Preparation

University of Wisconsin-Milwaukee   B.Sc. Chemistry   2007
University of Wisconsin-Milwaukee   Ph.D. Chemistry   2013

Publications

Judd, E.; Youngblut, M.; Pacheco, A.; Elliot, S. "Direct Electrochemistry of *Shewanella oneidensis* Cytochrome c Nitrite Reductase: Evidence for Interactions Across the Dimeric Interface" *Biochemistry*, **2012**, *51*, 10175-10185.

Youngblut, M.; Judd, E. T.; Srajer, V.; Sayyed, B.; Goelzer, T.; Elliott, S. J.; Schmidt, M.; Pacheco, A. A. "Laue Structure of *Shewanella oneidensis* Cytochrome *c* Nitrite Reductase from a High-yield Expression System" *J. Biol. Inorg. Chem.*, **2012**, *17*, 647-662 (DOI: 10.1007/s00775-012-0885-0).

Kostera, J.; Youngblut, M. D.; Slosarczyk, J. M.; Pacheco, A. A. "Kinetic and Product Distribution Analysis of NO· Reductase Activity in *N. europaea* Hydroxylamine Oxidoreductase" *J. Biol. Inorg. Chem.* **2008**, 1073-1083.

Selected Presentations

<u>Matthew D. Youngblut</u>, John Conrad, Graham Moran, Brian Bennett, A. Andrew Pacheco "Running a nitrite reductase in reverse: a spectroscopic study" Bioinorganic Chemistry Gordon Research Conference and Seminar, Jan. 20th-27th 2013, Ventura, CA.

<u>Matthew D. Youngblut</u>, John Conrad, Graham Moran, Brian Bennett, A. Andrew Pacheco "Running a nitrite reductase in reverse: a spectroscopic study" 32nd Midwest Enzyme Chemistry Conference, Oct. 13th 2012, University of Illinois at Chicago, Chicago, IL.

<u>Matthew D. Youngblut</u>, John Conrad, Graham Moran, Brian Bennett, A. Andrew Pacheco "Running a nitrite reductase in reverse: a spectroscopic study" Principles of EPR Training Workshop, Aug. 13th-15th 2012, Medical College of Wisconsin, Wauwatosa, WI.

<u>Matthew D. Youngblut</u>, Evan T. Judd, Vukica Srajer, Bilal Sayyed, Tyler Goelzer, Sean J. Elliott, Marius Schmidt, A. Andrew Pacheco "Laue Crystal Structure of *Shewanella oneidensis* Cytochrome c Nitrite Reductase from a High-yield Expression System" Bioinorganic Chemistry Gordon Research Seminar, Jan. 26th-29th 2012, Ventura, CA.

Matthew D. Youngblut, Joseph Eschweiler, Marius Schmidt, A. Andrew Pacheco "Structural and kinetic investigations of cytochrome *c* nitrite reductase from *Shewanella oneidensis*" 15th International Conference on Biological Inorganic Chemistry, Aug. 7th - 12th 2011, University of British Columbia, Vancouver, B. C. Canada.

Jennifer M. McGarry, Matthew D. Youngblut, A. Andrew Pacheco "Kinetic investigation of cytochrome c_{554} nitrosylation" 15th International Conference on Biological Inorganic Chemistry, Aug. 7th - 12th 2011, University of British Columbia, Vancouver, B. C. Canada.

Matthew D. Youngblut, Marius Schmidt, A. Andrew Pacheco "Using Laue x-ray diffraction to solve a crystal structure" Bioinorganic Chemistry Gordon Research Seminar, Feb. 3rd-6th 2011, Ventura, CA.

Matthew D. Youngblut, A. Andrew Pacheco "Laser photo-initiated nitrosylation of *N. europaea* cytochrome c_{554}: A study of the protein's role in reducing NO·" 233rd ACS National Meeting, Mar. 25th-29th 2007, Chicago, IL.

Presented posters on current research at the University of Wisconsin-Milwaukee Department of Chemistry and Biochemistry on Awards Day, annually, 2007-2013.

Technical Skills

Biochemistry/molecular biology

Protein purification. Proficient in all current protein purification techniques, using both FPLC and LPLC; extensive experience in developing purification protocols for challenging proteins.

Protein over-expression systems. Successfully designed over-expression systems in atypical bacteria for obtaining proteins that do not express well using traditional techniques.

Bacterial growth. Experienced at growing bacteria in both small and large scale cultures (up to 100 L batches).

Bacterial cloning. Proficient in all current techniques used for cloning genes in Gram-negative bacteria.

Anaerobic techniques. Highly proficient at handling proteins and other materials anaerobically using gloveboxes and inert gas Schlenk line systems.

Data analysis and instrumentation

UV/visible spectroscopy-based techniques. Highly proficient in a wide variety of UV/visible spectroscopic techniques, including assay development, time-resolved experiments using either **stopped-flow** or **nanosecond laser-pulsed** initiation, and **UV/Vis spectroelectrochemistry** (see below).

Time-resolved nanosecond laser-initiated spectroscopy. Significant experience in using nanosecond pulsed lasers for photo-initiating reactions within protein solutions, which could then be followed on microsecond and longer timescales using UV/Vis spectroscopy. Experience included developing the photo-active systems, aligning the laser optics and analyzing the collected data.

Stopped-flow UV/visible spectroscopy. Significant experience with single- and double-mixing stopped-flow initiation of experiments.

Protein electrochemistry. Performed potentiometric titrations of proteins with multiple redox-active sites using ultra-thin cuvettes equipped with optically transparent electrodes, which allowed the system to be monitored using UV/Vis spectroscopy at each applied potential.

Rapid freeze-quench protein EPR. Some experience using the rapid freeze-quench technique to prepare samples for EPR spectroscopy. In this technique a reaction is initiated by rapid mixing of two or more solutions, after which the

mixture is quickly frozen to kinetically trap proteins in meta-stable intermediate states, which are then investigated using EPR. Samples can be frozen in as little as 10 ms after mixing.

Data analysis using PTC Mathcad and Microcal Origin. Developed custom scripts and methodologies for the global analysis of large and complex datasets resolved in multiple domains (e.g.: absorbance vs. time and wavelength in UV/Vis time resolved spectroscopy, or absorbance vs. time and applied potential in UV/Vis spectroelectrochemistry).

Protein crystallography. Significant experience with growing protein crystals and using protein crystallization screens; some experience with collecting and interpreting diffraction data.

HPLC. Some experience using analytical HPLC for monitoring enzymatic reactions; includes method development.

Awards

George Sosnovsky Award for Excellence in Graduate Research – 2012

Durward-Layde Memorial Scholarship – 2007

Travisan-Fueger Graduate Fellowship – 2007

Analytical Chemistry Award in the UWM Chemistry Department – 2007

Service, Education and Outreach

Direct supervisor for 1-3 undergraduate researchers each semester between Spring 2007 and Fall 2012.

Founding member of the UWM Chemistry department's Graduate Student Council. Duties included working directly with the faculty on planning departmental events, handling graduate students' concerns, and editing departmental documents.

Active participant in the American Chemical Society's Project Seed program, which sponsors talented high school students from economically disadvantaged backgrounds to spend summers working in a research laboratory.

Active participant in the NSF's Research Experience for Teachers program, which provides a professional development opportunity to K-12 science teachers by placing them in a research laboratory during the summer.

Chair of the "New Approaches" session at the 32nd Midwest Enzyme Chemistry Conference, Oct. 13th 2012, University of Illinois at Chicago, Chicago, IL.